

## Spin-orbit coupling and geometric phases at oxide interfaces

Groenendijk, Dirk

**DOI**

[10.4233/uuid:265e1be8-6edc-4ee2-8b9c-8d01a6022448](https://doi.org/10.4233/uuid:265e1be8-6edc-4ee2-8b9c-8d01a6022448)

**Publication date**

2019

**Document Version**

Final published version

**Citation (APA)**

Groenendijk, D. (2019). *Spin-orbit coupling and geometric phases at oxide interfaces*. [Dissertation (TU Delft), Delft University of Technology]. <https://doi.org/10.4233/uuid:265e1be8-6edc-4ee2-8b9c-8d01a6022448>

**Important note**

To cite this publication, please use the final published version (if applicable). Please check the document version above.

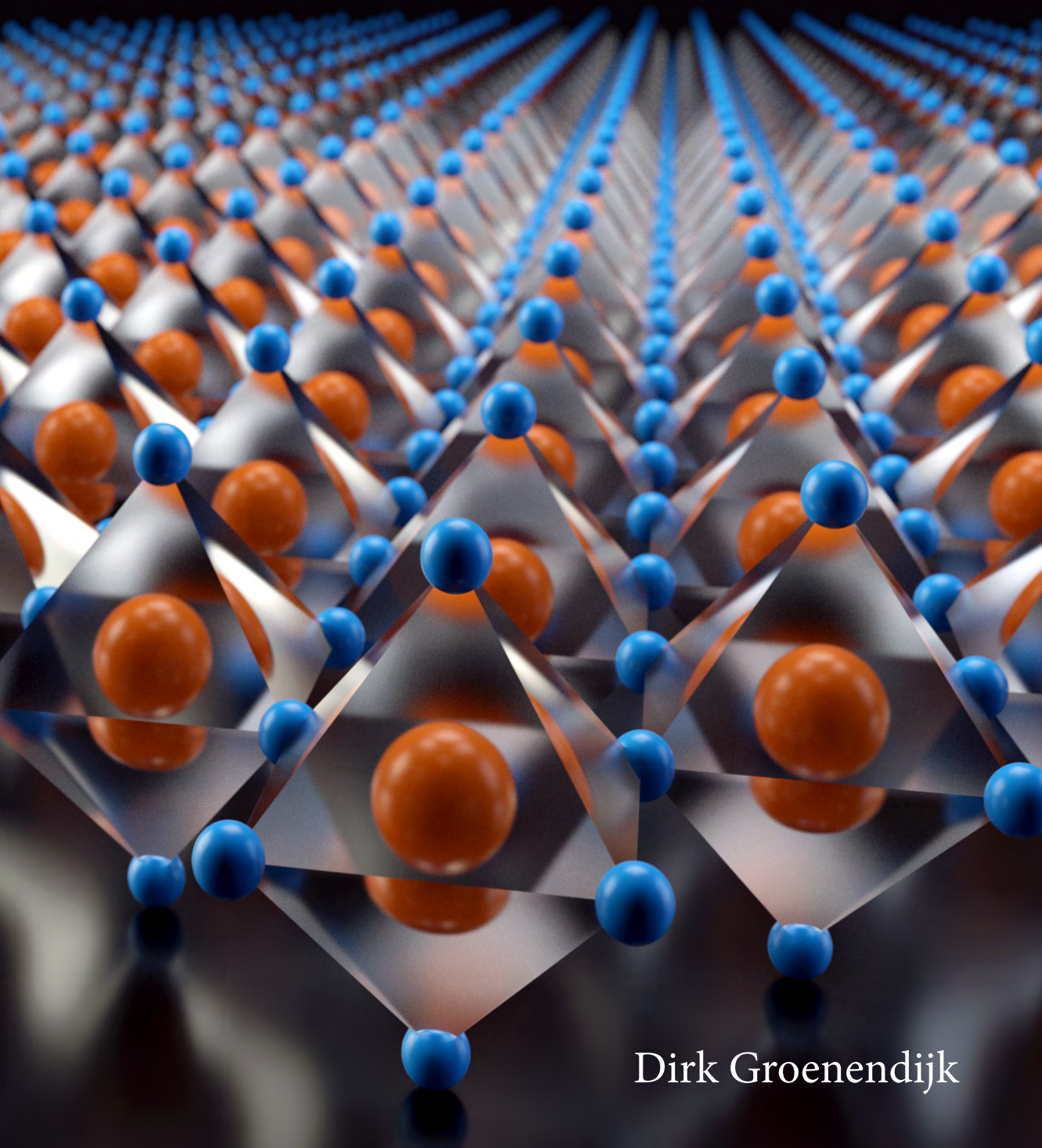
**Copyright**

Other than for strictly personal use, it is not permitted to download, forward or distribute the text or part of it, without the consent of the author(s) and/or copyright holder(s), unless the work is under an open content license such as Creative Commons.

**Takedown policy**

Please contact us and provide details if you believe this document breaches copyrights. We will remove access to the work immediately and investigate your claim.

# Spin-orbit coupling and geometric phases at oxide interfaces



Dirk Groenendijk



# **SPIN–ORBIT COUPLING AND GEOMETRIC PHASES AT OXIDE INTERFACES**

## **Dissertation**

for the purpose of obtaining the degree of doctor  
at Delft University of Technology  
by the authority of the Rector Magnificus Prof. Dr. Ir. T. H. J. van der Hagen,  
Chair of the Board for Doctorates,  
to be defended publicly on Monday 28 January 2019 at 10:00 o'clock

by

**Dirk Jan GROENENDIJK**

Master of Science in Applied Physics,  
Delft University of Technology, Delft, The Netherlands,  
born in Nieuwegein, The Netherlands.

This dissertation has been approved by

Promotor: Dr. A. D. Caviglia

Promotor: Prof. Dr. Ir. H. S. J. van der Zant

**Composition of the doctoral committee:**

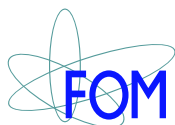
Rector Magnificus,  
Dr. A. D. Caviglia,  
Prof. Dr. Ir. H. S. J. van der Zant,

Chairperson  
Technische Universiteit Delft  
Technische Universiteit Delft

*Independent members:*

Prof. Dr. J. Santamaria,  
Prof. Dr. T. Banerjee,  
Prof. Dr. Ir. G. Koster,  
Prof. Dr. P. G. Steeneken,  
Dr. M. Cuoco,  
Prof. Dr. Y. Blanter,

Universidad Complutense de Madrid  
Rijksuniversiteit Groningen  
Universiteit Twente  
Technische Universiteit Delft  
Università degli Studi di Salerno  
Technische Universiteit Delft (*reserve*)



*Keywords:* Complex oxide heterostructures & interfaces, strontium iridates & ruthenates, spin-orbit coupling, electronic correlations, low-temperature electronic transport, Berry phase, freestanding oxides

*Printed by:* Gildeprint, Enschede

*Front & Back:* Render of a single perovskite layer of  $\text{BO}_6$  octahedra.

Copyright © 2019 by D. J. Groenendijk

Casimir PhD series 2018-16

ISBN 978-90-8593-381-6

An electronic version of this dissertation is available at  
<http://repository.tudelft.nl/>.

# CONTENTS

<b>Abbreviations</b>	<b>ix</b>
<b>Summary</b>	<b>xi</b>
<b>Samenvatting</b>	<b>xiii</b>
<b>1 Introduction</b>	<b>1</b>
1.1 Energy scales in transition metal oxides . . . . .	3
1.1.1 Electronic correlations . . . . .	3
1.1.2 Spin-orbit coupling . . . . .	4
1.2 Thin films and heterostructures. . . . .	5
1.2.1 Pulsed laser deposition . . . . .	5
1.2.2 Strontium iridates . . . . .	7
1.2.3 Strontium ruthenates . . . . .	8
1.3 Outline of this thesis . . . . .	10
<b>2 Epitaxial growth and stability of SIO/STO heterostructures</b>	<b>11</b>
2.1 Structural and electronic characterization . . . . .	12
2.2 Laser-induced target surface modification . . . . .	15
2.3 Film degradation in ambient conditions . . . . .	16
2.4 Conclusions. . . . .	17
2.5 Methods . . . . .	17
2.6 Supplementary information . . . . .	18
2.6.1 Additional X-ray diffraction measurements . . . . .	18
2.6.2 Modeling of resistivity-temperature data . . . . .	19
2.6.3 Growth rate and target surface morphology . . . . .	19
2.6.4 Preservation of the film properties by STO encapsulation . . . . .	21
<b>3 Balanced electron-hole transport in SIO/STO heterostructures</b>	<b>23</b>
3.1 Back-gate modulation of magnetotransport . . . . .	24
3.2 Temperature-dependent thermoelectric response . . . . .	26
3.3 Modeling of electronic transport parameters . . . . .	29
3.4 Conclusions. . . . .	30
3.5 Methods . . . . .	31
3.6 Supplementary information . . . . .	31
3.6.1 Influence of oxygen vacancies on the resistance . . . . .	31
3.6.2 Sampling algorithm . . . . .	32
3.6.3 Magnetoresistance analysis . . . . .	33

<b>4</b>	<b>Spin-orbit semimetal SIO in the two-dimensional limit</b>	<b>35</b>
4.1	Critical thickness of the MI transition . . . . .	37
4.2	Magnetoconductance near the transition point. . . . .	38
4.3	Scanning tunneling spectroscopy . . . . .	40
4.4	First-principles calculations . . . . .	41
4.5	Conclusions. . . . .	41
4.6	Methods . . . . .	42
4.7	Supplementary information . . . . .	43
4.7.1	Film growth and Hall bar fabrication. . . . .	43
4.7.2	Influence of the STO cap layer . . . . .	44
4.7.3	Transport in the localized regime . . . . .	44
4.7.4	Modeling of magnetotransport data . . . . .	45
<b>5</b>	<b>Anisotropic magnetoresistance in two-dimensional SIO</b>	<b>49</b>
5.1	Low-temperature magnetotransport . . . . .	50
5.2	Angular dependence of magnetoresistance . . . . .	51
5.3	Anisotropic magnetoresistance in different planes . . . . .	52
5.4	Field-induced magnetic transition . . . . .	53
5.5	Conclusions. . . . .	54
5.6	Methods . . . . .	55
5.7	Supplementary information . . . . .	55
5.7.1	Growth of SIO/STO heterostructures. . . . .	55
5.7.2	Magnetoresistance of 5 and 30 u.c. films . . . . .	55
<b>6</b>	<b>Berry phase engineering in STO/SRO/SIO heterostructures</b>	<b>59</b>
6.1	Anomalous Hall effect of ultrathin SRO . . . . .	60
6.2	Presence of two anomalous Hall channels . . . . .	64
6.3	Control of the relative spin polarizations . . . . .	66
6.4	Conclusions. . . . .	68
6.5	Methods . . . . .	68
6.6	Supplementary information . . . . .	69
6.6.1	Structural and magnetic characterization . . . . .	69
6.6.2	Additional magnetotransport characterization. . . . .	70
6.6.3	Anomalous Hall effect in ultrathin SRO bilayers . . . . .	76
6.6.4	(111)-oriented STO/SRO/SIO heterostructures . . . . .	79
<b>7</b>	<b>Ultrathin complex oxide nanomechanical resonators</b>	<b>83</b>
7.1	Preparation of freestanding films . . . . .	84
7.2	Mechanical characterization of oxide resonators . . . . .	85
7.3	Temperature-dependent mechanical properties . . . . .	87
7.4	Conclusions. . . . .	91
7.5	Methods . . . . .	91
7.6	Supplementary information . . . . .	92
7.6.1	Growth & characterization of freestanding films . . . . .	92
7.6.2	SHG study of freestanding STO . . . . .	93

---

<b>8 Conclusions and perspectives</b>	<b>95</b>
8.1 Spin and charge accumulation at oxide interfaces . . . . .	96
8.2 Berry phase engineering in freestanding oxides . . . . .	97
8.3 Functional oxide resonators and supercapacitors . . . . .	98
<b>References</b>	<b>99</b>
<b>Curriculum Vitæ</b>	<b>111</b>
<b>List of Publications</b>	<b>113</b>
<b>Acknowledgements</b>	<b>115</b>



# LIST OF ABBREVIATIONS

2D	two-dimensional
a.u.	arbitrary units
ABF	annular bright-field
ADF	annular dark-field
AFM	atomic force microscopy
AHE	anomalous Hall effect
AMR	anisotropic magnetoresistance
ARPES	angle-resolved photoemission spectroscopy
c.p.s.	counts per second
CMOS	complementary metal oxide semiconductor
DFT	density functional theory
DOS	density of states
EELS	electron energy loss spectroscopy
EDX	energy-dispersive X-ray spectroscopy
GGA	generalized gradient approximation
HAADF-STEM	high-angle annular dark-field scanning transmission electron microscopy
LAO	$\text{LaAlO}_3$
LSDA	local spin density approximation
LSMO	$\text{La}_{1-x}\text{Sr}_x\text{MnO}_3$
MBE	molecular beam epitaxy
MEMS	microelectromechanical systems
MIT	metal-insulator transition
MR	magnetoresistance
NEMS	nanoelectromechanical systems
PPMS	physical property measurement system

---

PDMS	polydimethylsiloxane
PLD	pulsed laser deposition
r.l.u.	reciprocal lattice units
QCP	quantum critical point
RHEED	reflection high-energy electron diffraction
RRR	residual resistivity ratio
SAO	$\text{Sr}_3\text{Al}_2\text{O}_6$
SHG	second harmonic generation
SIO	$\text{SrIrO}_3$
SOC	spin-orbit coupling
SRO	$\text{SrRuO}_3$
STEM	scanning transmission electron microscope
STM	scanning tunneling microscopy
STO	$\text{SrTiO}_3$
STS	scanning tunneling spectroscopy
SQUID	superconducting quantum interference device
TEM	transmission electron microscopy
THE	topological Hall effect
TMO	transition metal oxide
u.c.	unit cell
VNA	vector network analyser
VRH	variable range hopping
XAS	X-ray absorption spectroscopy
XRD	X-ray diffraction
XRR	X-ray reflectivity

# SUMMARY

In this work, we investigate electronic and magnetic phenomena in thin films and heterostructures of transition metal oxides with strong spin–orbit coupling. Ultrathin films are prepared by pulsed laser deposition, a technique which enables layer-by-layer growth of complex materials on atomically flat crystal surfaces. The properties of these heterostructures, which include materials such as strontium iridate ( $\text{SrIrO}_3$ ) and strontium ruthenate ( $\text{SrRuO}_3$ ), are probed by applying electric and magnetic fields. By varying parameters such as temperature, magnetic field strength and layer thickness, we obtain information about spin and charge transport in these atomically engineered crystals.

[Chapter 1](#) provides an introduction to the field of transition metal oxides, followed by a brief overview of the materials studied in this dissertation.

[Chapters 2 to 5](#) are dedicated to  $\text{SrIrO}_3$ , a material that displays unexpected physical properties owing to the strong spin–orbit coupling of Ir. [Chapter 2](#) starts with the growth and thermodynamic stability of  $\text{SrIrO}_3$ , which is essential to obtain high-quality films and study their properties in the ultrathin limit. We develop a method to grow stoichiometric films by measuring their transport characteristics as a function of the target condition. We discover that the properties of  $\text{SrIrO}_3$  are sensitive to degradation in air and develop an encapsulation procedure to protect the film surface.

$\text{SrIrO}_3$  displays an exotic semimetallic state due to the interplay between electronic correlations, spin–orbit coupling, and octahedral rotations. In [Chapter 3](#), we combine thermoelectric and magnetotransport measurements to quantitatively determine the transport coefficients of the different conduction channels. Despite their different dispersion relationships, electrons and holes are found to have strikingly similar transport coefficients.

[Chapters 4 and 5](#) focus on the electronic and magnetic properties of  $\text{SrIrO}_3$  in the two-dimensional limit. In [Chapter 4](#), we discover a metal–insulator transition occurring at a critical thickness of 4 unit cells and an enhancement of spin fluctuations near the transition point. We investigate the magnetic state in [Chapter 5](#), showing that a four-fold symmetric magnetoresistance component appears above a critical magnetic field.

In [Chapter 6](#), we interface ultrathin  $\text{SrIrO}_3$  with  $\text{SrRuO}_3$ , an itinerant ferromagnet with an unconventional anomalous Hall conductivity. We discover that the presence of two dissimilar interfaces results in the emergence of two spin-polarized conduction channels.

Having explored the influence of epitaxial interfaces, in [Chapter 7](#) we develop a method to detach thin films from their growth substrate using an epitaxial buffer layer. Using this approach, we prepare nanomechanical resonators of freestanding  $\text{SrTiO}_3$  and  $\text{SrRuO}_3$  films. By measuring the temperature dependence of their mechanical response, we observe signatures of structural phase transitions in the  $\text{SrTiO}_3$ , which affect the strain and mechanical dissipation of the resonators.

**Chapter 8** summarizes the findings of the previous chapters and provide perspectives for future work. We discuss ongoing experiments regarding Berry phase engineering and the manipulation of freestanding films.

# SAMENVATTING

In dit werk onderzoeken we elektronische en magnetische fenomenen in dunne films en heterostructuren van transitietmetaaloxiden met sterke spin–baan koppeling. Dunne films worden bereid door middel van gepulseerde laserdepositie, een techniek waarmee complexe materialen laagje voor laagje op atomair vlakke kristaloppervlakken gegroeid kunnen worden. De eigenschappen van deze heterostructuren, waartoe strontium iridium oxide ( $\text{SrIrO}_3$ ) en strontium ruthenium oxide ( $\text{SrRuO}_3$ ) behoren, worden bestudeerd met behulp van elektrische en magnetische velden. Door parameters zoals temperatuur, magnetische veldsterkte en laagdikte te variëren, verkrijgen we informatie over spin- en ladingstransport in deze atomair ontworpen kristallen.

**Hoofdstuk 1** geeft een inleiding tot het veld van transitietmetaaloxiden, gevolgd door een beknopt overzicht van de materialen die in dit proefschrift bestudeerd worden.

**Hoofdstukken 2 tot 5** zijn toegewijd aan  $\text{SrIrO}_3$ , een materiaal dat onverwachte fysische eigenschappen vertoont dankzij de sterke spin–baan koppeling van Ir. **Hoofdstuk 2** begint met de groei en thermodynamische stabiliteit van  $\text{SrIrO}_3$ , wat essentieel is om films van hoge kwaliteit te verkrijgen en hun eigenschappen te bestuderen in de tweedimensionale limiet. We ontwikkelen een methode om stoichiometrische films te groeien door hun transporteigenschappen te meten als functie van de target-toestand. We ontdekken dat de eigenschappen van  $\text{SrIrO}_3$  gevoelig zijn voor degradatie en ontwikkelen een procedure om het oppervlak te beschermen.

$\text{SrIrO}_3$  vertoont een exotische semimetallische toestand door de wisselwerking tussen elektronische correlaties, spin–baan koppeling en octaëdrische rotaties. In **Hoofdstuk 3** combineren we thermoelektrische en magnetische transportmetingen om de transportcoëfficiënten van de verschillende geleidingskanalen te bepalen. Ondanks hun verschillende dispersierelaties vinden we dat elektronen en gaten vergelijkbare transportcoëfficiënten hebben.

**Hoofdstukken 4 en 5** zijn gericht op de elektronische en magnetische eigenschappen van  $\text{SrIrO}_3$  in de tweedimensionale limiet. In **Hoofdstuk 4** ontdekken we dat een transitie van een metaalachtige naar een isolerende toestand plaatsvindt bij een kritische dikte van 4 lagen en dat spin fluctuaties versterkt zijn nabij het transitiepunt. We onderzoeken de magnetische toestand in **Hoofdstuk 5** en tonen aan dat een viervoudig symmetrische magnetowerstand component verschijnt boven een kritisch magnetisch veld.

In **Hoofdstuk 6** creëren we grensvlakken tussen  $\text{SrIrO}_3$  en  $\text{SrRuO}_3$ , een ferromagneet met een onconventioneel “anomalous Hall effect”. We ontdekken dat de aanwezigheid van twee verschillende grensvlakken leidt tot de manifestatie van twee spingepolariseerde geleidingskanalen.

Na de invloed van epitaxiale grensvlakken te hebben bestudeerd, ontwikkelen we in **Hoofdstuk 7** een methode om dunne films te scheiden van het substraat door gebruik te maken van een bufferlaag. Met deze methode maken we nanomechanische resonatoren

van vrijstaande  $\text{SrTiO}_3$  en  $\text{SrRuO}_3$  films. Door de temperatuurafhankelijkheid van hun mechanische respons te meten, nemen we kenmerken van structurele faseovergangen in  $\text{SrTiO}_3$  waar, die de spanning en mechanische dissipatie van de resonatoren beïnvloeden.

**Hoofdstuk 8** vat de bevindingen van de voorgaande hoofdstukken samen en verschaft perspectieven voor toekomstig werk. We bespreken nog lopende experimenten met betrekking tot het ontwerpen van geometrische fases en de manipulatie van vrijstaande films.

# 1

## INTRODUCTION

*The electric light did not come from  
the continuous improvement of candles.*

Oren Harari

*In this chapter we introduce the field of transition metal oxides and discuss its relevance to society. We also briefly review the physical concepts that are relevant for the properties of the materials investigated in this thesis.*

WE live in the information age, a period marked by *digitalization* and *computerization*. The information age is also referred to as the *silicon age*, since the digital revolution was made possible by the industrial processing of silicon and the production of transistors of ever-smaller dimensions. The widespread use of smaller, cheaper and more powerful computers has affected nearly every aspect of our everyday life and transformed our economy. In this regard, silicon has proven to be as revolutionary as stone, bronze and iron in their respective ages.

The information age presents many challenges for the coming decades, including the growing need for (i) fast, high-capacity and secure information storage, (ii) a sustainable energy economy and (iii) increased computational power. It is becoming increasingly clear that novel materials, that can generate devices with properties such as ultralow energy consumption and high speed and capacity, are required to address these challenges. This need has vastly expanded the field of materials research, a rapidly growing area that sees a strong interest from both academia and industry.

One of the material classes that are considered particularly promising for next-generation electronic devices is *transition metal oxides* (TMOs). These materials show a range of exceptional physical properties due to the delicate interplay among their spin, charge and orbital degrees of freedom [1, 2]. A significant body of work has been devoted to TMOs containing  $3d$  and  $4d$  elements, which include systems displaying metal-insulator transitions [3], high- $T_c$  superconductivity [4] and Mott insulating states [5, 6]. At the heart of these properties are *strong electronic correlations*, arising due to strong electrostatic repulsion between electrons on neighboring sites.

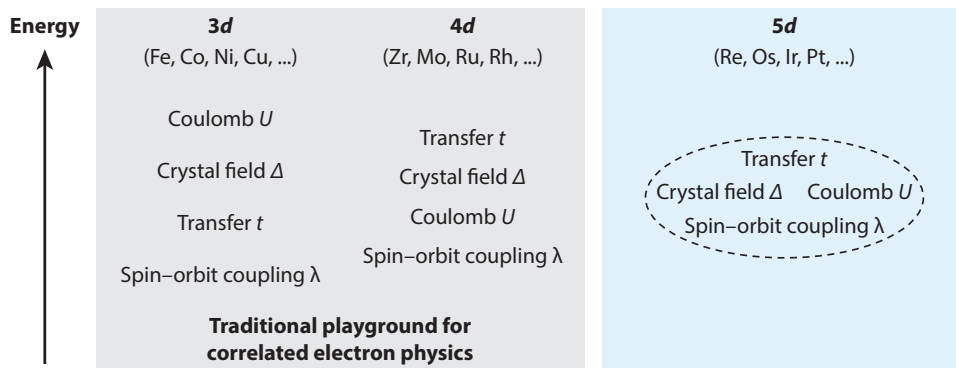


Figure 1.1: **Energy landscape of transition metal oxides.** Schematic illustration of the hierarchy among energy scales in  $3d$ ,  $4d$ , and  $5d$  transition metal oxides.

Much less attention has been directed to  $5d$  TMOs due to the relative scarcity of  $5d$  elements and the difficulty of synthesizing them. Apart from strong correlations, the electrons in these materials have an important property called *spin-orbit coupling* (SOC), a relativistic effect that entangles the spin and orbital degrees of freedom. This property is particularly useful for applications since it can provide a platform for spintronics (devices that operate with spin rather than charge currents) and enable data processing with minimal dissipation [7, 8].

The interplay between electronic correlations and SOC is far from understood and needs to be investigated in the appropriate material systems. Here, we study the structural, electronic and magnetic properties of single-crystal thin films and heterostructures of strontium iridates ( $\text{SrIrO}_3$  and  $\text{Sr}_2\text{IrO}_4$ ) and strontium ruthenate ( $\text{SrRuO}_3$ ). While Ir is not abundant and is unlikely to be widely used in future devices, the study of these materials will advance our fundamental understanding and provide pathways for engineering similar states in systems with more common elements. Our primary focus is on the properties of ultrathin  $\text{SrIrO}_3$  and the formation of epitaxial interfaces with  $\text{SrRuO}_3$ . Finally, we use a novel method to obtain freestanding oxides and fabricate nanomechanical resonators to probe their structural phase transitions.

## 1.1. ENERGY SCALES IN TRANSITION METAL OXIDES

The electronic and magnetic properties of TMOs are governed by the hierarchy between different energy scales (see Fig. 1.1). In this section, we will review the physical principles governing these energy scales and discuss their impact on the electronic and magnetic structure.

### 1.1.1. ELECTRONIC CORRELATIONS

Transition metal oxides typically have incompletely filled  $d$ -orbitals with narrow energy bands. Due to the small overlap between neighbouring orbitals, the behavior of electrons cannot be described in terms of non-interacting entities. This interaction is accounted for in the Hubbard model [9], an extension of the tight-binding model where electrons can hop between nearest-neighbour lattice sites with a kinetic energy  $-t$  (see Fig. 1.2). The Hubbard model introduces an additional energy  $U$  for a pair of electrons occupying the same site due to Coulomb repulsion.

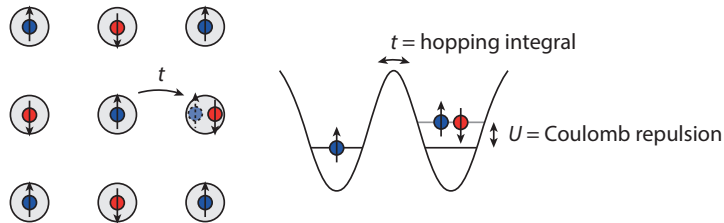


Figure 1.2: **The Hubbard model.** Intersite hopping saves energy  $t$ , while double occupancy costs energy  $U$ . This model gives rise to an insulating state at large  $U/t$ , called a Mott insulator.

The Hubbard Hamiltonian is given by

$$H = -t \sum_{\langle i,j \rangle, \sigma} c_{i\sigma}^\dagger c_{j\sigma} + U \sum_{\mathbf{i}} n_{i\uparrow} n_{i\downarrow}, \quad (1.1)$$

where the first term is the kinetic energy, describing the destruction of a fermion of spin  $\sigma$  on site  $i$  and its creation on the neighboring site  $j$  (or vice versa). The second term is the interaction energy, which adds an energy  $U$  if a site is doubly occupied.

While conventional band theory predicts a metallic state for a half-filled band, the Hubbard model correctly predicts the Mott insulating state. It is instrumental in describing high-temperature superconductivity and the superfluid–Mott insulator transition in cold-atom experiments. Additionally, it spurred the development of dynamical mean-field theory (DMFT), which is now widely used to calculate the electronic structure of strongly correlated materials. We will see in [Section 1.2.2](#) that even a moderate  $U$  can have profound effects on the electronic and magnetic properties of strontium iridates.

### 1.1.2. SPIN–ORBIT COUPLING

Spin–orbit coupling (SOC) is a relativistic effect that entangles the spin and orbital angular momentum of the electron (see [Fig. 1.3](#)). In the rest frame of an electron bound to an atom, the electron experiences a magnetic field  $\mathbf{B}$ . Since  $E \propto \Delta V$  (where  $E$  is the electric field and  $V$  the potential),

$$\mathbf{B} \propto \mathbf{v} \times \mathbf{E} = \frac{\mathbf{r} \times \mathbf{p}}{mr} |\Delta V|, \quad (1.2)$$

where  $\mathbf{v}$  is the velocity of the electron and  $\mathbf{r} \times \mathbf{p}$  is the angular momentum  $\mathbf{L}$  [10]. Multiplying by the magnetic moment of the electron  $\mathbf{m}_s$  yields

$$\mathbf{B} \cdot \mathbf{m}_s \propto \mathbf{L} \cdot \mathbf{S}, \quad (1.3)$$

where  $\mathbf{S}$  is the spin angular momentum vector.

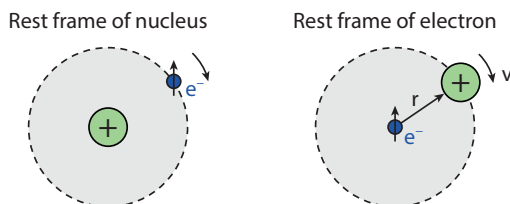


Figure 1.3: **Spin–orbit coupling.** Schematic illustration of the relativistic interaction between the electron's spin and the positively charged nucleus.

The complete expression for the SOC strength (not shown here) contains an energy scale  $\lambda$  which is proportional to  $Z^4$ , where  $Z$  is the atomic number. SOC is therefore small for light elements but becomes significant for heavy elements such as Ru ( $\lambda \sim 0.1$  eV) and Ir ( $\lambda \sim 0.4$  eV) [11, 12]. In atomic systems, SOC breaks the degeneracy between different energy levels and causes splitting of spectral lines. In solids, SOC results in splitting of electronic bands that are otherwise degenerate. When these bands are close to the Fermi level and the splitting is sufficiently large, this can substantially impact the electronic properties. As we will see in [Section 1.2.2](#), splitting due to SOC gives rise to narrow  $J_{\text{eff}} = 1/2$  states in the electronic structure of  $\text{Ir}^{4+}$ , which can be easily gapped by even a moderate value of the Coulomb repulsion  $U$ . In  $\text{SrRuO}_3$  (SRO), SOC causes the easy axis of magnetization to be perpendicular to the film plane and is important in setting the intrinsic contribution to the anomalous Hall conductivity ( $\sigma_{xy}$ ), which will be discussed in [Section 1.2.3](#).

## 1.2. THIN FILMS AND HETEROSTRUCTURES

Thin films of TMOs can be grown by different techniques such as pulsed laser deposition (PLD) and molecular beam epitaxy (MBE). The advantages of PLD are that (i) the transfer of materials is in general stoichiometric, (ii) the deposition can occur in a high oxygen pressure environment, and (iii) the energy of the ablated species can be controlled by the laser fluence [13]. A schematic illustration of a PLD system is shown in Fig. 1.4a.

### 1.2.1. PULSED LASER DEPOSITION

During PLD, a high-power ultraviolet pulsed laser (Coherent COMPexPro 205, KrF 248 nm) is focused on a target of the material that is to be deposited onto a single-crystal substrate. STO is frequently used as a growth substrate due to its insulating properties and the possibility of terminating its surface with  $\text{TiO}_2$ , forming an atomically flat template for thin film growth [14, 15]. The STO substrates used in this thesis were purchased from CrysTec GmbH. The initial part of the laser pulse ablates the target material, while the rest of the pulse ionises the ablated species. This causes the material to be accelerated towards the substrate, forming a so-called plasma plume. A constant flow of  $\text{O}_2$  is maintained in the chamber to oxidise the ablated species and reduce their kinetic energy. For the growth of SIO and SRO, the oxygen partial pressure is typically of the order of 0.1 mbar, while the base pressure of the system is about  $10^{-8}$  mbar. The ablated material is deposited on the substrate, which is heated by an infrared laser (to about  $600^\circ\text{C}$  for SIO and SRO) to promote the surface diffusivity. A typical growth rate for these two compounds is 100 pulses per unit cell. The substrates are mounted with two stainless steel clamps and the temperature is measured using an optical pyrometer. We monitor the growth using reflection high-energy electron diffraction (RHEED), a technique which relies on the diffraction of high-energy electrons from the surface of the growing film. After the growth, the samples are annealed for 1 hour in 300 mbar of  $\text{O}_2$  at  $550^\circ\text{C}$  to refill any oxygen vacancies that might have formed. Finally, the samples are cooled down in the same atmosphere at a rate of  $20^\circ\text{C}/\text{min}$ .

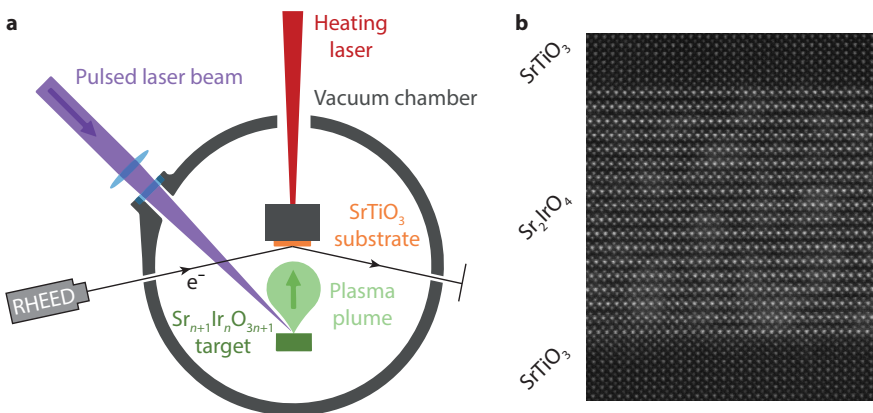


Figure 1.4: **Growth of transition metal oxide heterostructures.** (a) Schematic illustration of pulsed laser deposition. (b) Transmission electron microscopy measurement of an  $\text{STO}/\text{Sr}_2\text{IrO}_4/\text{STO}$  heterostructure.

Our PLD system can contain 5 different targets at any time, making it possible to grow heterostructures of different materials, each with their ideal growth conditions such as temperature, pressure, and laser fluence. An example of a heterostructure composed of STO/Sr<sub>2</sub>IrO<sub>4</sub>/STO is shown in Fig. 1.4b. The STO on the bottom of the image is the substrate, while the top STO is used to impose symmetric boundary conditions and protect the Sr<sub>2</sub>IrO<sub>4</sub> film from degradation in air. Since a large portion of the work covered in this thesis is focused on SIO, we will showcase the growth and characterization of epitaxial Sr<sub>2</sub>IrO<sub>4</sub> in Fig. 1.5.

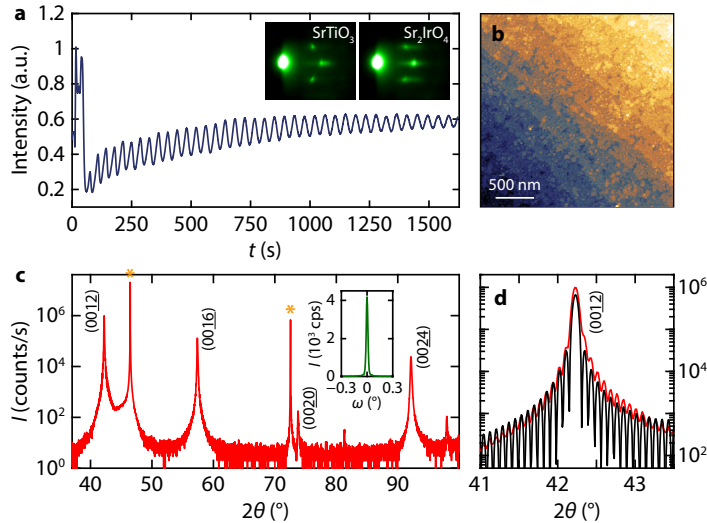


Figure 1.5: **Growth and characterization of epitaxial Sr<sub>2</sub>IrO<sub>4</sub>.** (a) RHEED intensity oscillations of the specular spot during the growth of a 45 u.c. Sr<sub>2</sub>IrO<sub>4</sub> film. Four oscillations correspond to 1 SrO-IrO<sub>2</sub>-SrO block. (b) AFM topographic image of the surface of a 10 u.c. Sr<sub>2</sub>IrO<sub>4</sub> film. (c) XRD measurement of an STO-capped 45 u.c. Sr<sub>2</sub>IrO<sub>4</sub> film. Inset: rocking curve around the Sr<sub>2</sub>IrO<sub>4</sub> (0012) reflection. (d) XRD measurement around the (0012) reflection. The black solid line is a simulation of the diffracted intensity with 45 u.c. and  $c = 25.66 \text{ \AA}$ .

Figure 1.5a shows RHEED intensity oscillations during the growth of Sr<sub>2</sub>IrO<sub>4</sub> on a TiO<sub>2</sub>-terminated STO substrate, where each oscillation corresponds to the growth of one SrO-IrO<sub>2</sub>-SrO block. The inset shows the diffraction pattern before and after the growth. Various techniques are used to investigate the surface and crystalline quality of the films after the growth. In Fig. 1.5b, an atomic force microscopy (AFM) image of the film surface is shown, where the step-and-terrace structure of the STO substrate is still clearly visible and only islands of unit cell height are observed. The crystal structure of the film can be studied using X-ray diffraction (XRD), of which a measurement ( $\theta$ - $2\theta$  scan) is shown in Fig. 1.5c. The intense, narrow peaks correspond to the  $c$ -axis lattice parameter of the STO substrate ( $3.905 \text{ \AA}$ ) and the other peaks arise from the Sr<sub>2</sub>IrO<sub>4</sub> film (bulk lattice parameter  $25.79 \text{ \AA}$ ). The finite size oscillations around the peak can be fitted to extract the film thickness, as shown in Figure 1.5d, and the peak position is determined by the  $c$ -axis lattice parameter. The simulation of the diffracted intensity (made with InteractiveXRDFit [16]) yields a thickness of 45 u.c. and a  $c$ -axis lattice parameter of  $25.66 \text{ \AA}$ . The

thickness is in good agreement with the thickness determined by RHEED. Note that the  $c$ -axis is slightly smaller than that of bulk  $\text{Sr}_2\text{IrO}_4$  (25.79 Å), which results from the tensile strain (−0.7% lattice mismatch) from the STO substrate.

### 1.2.2. STRONTIUM IRIDATES

The electronic structure of  $\text{Sr}_{n+1}\text{Ir}_n\text{O}_{3n+1}$  compounds can be best understood starting from Ir in an octahedral environment [17]. The energy levels of a single  $\text{IrO}_6$  octahedron are shown in Fig. 1.6a. Ir has electronic configuration  $[\text{Xe}] 4f^{14} 5d^7 6s^2$ , which leads to  $5d^5$  due to its oxidation state of 4+. The  $5d$  levels are first split into  $t_{2g}$  and  $e_g$  orbital states by the crystal field energy  $\Delta$ , which increases the energy of orbitals with lobes pointing towards the oxygen ions. The  $t_{2g}$  levels are further split by SOC into effective total angular momentum  $J_{\text{eff}} = 1/2$  and  $J_{\text{eff}} = 3/2$  levels. This effectively reduces the system to a half-filled  $J_{\text{eff}} = 1/2$  single band system [18]. This band is then affected by the correlation energy  $U$ , which is determined by the octahedral connectivity (see Fig. 1.6b) which is different for each member of the RP series [19, 20].

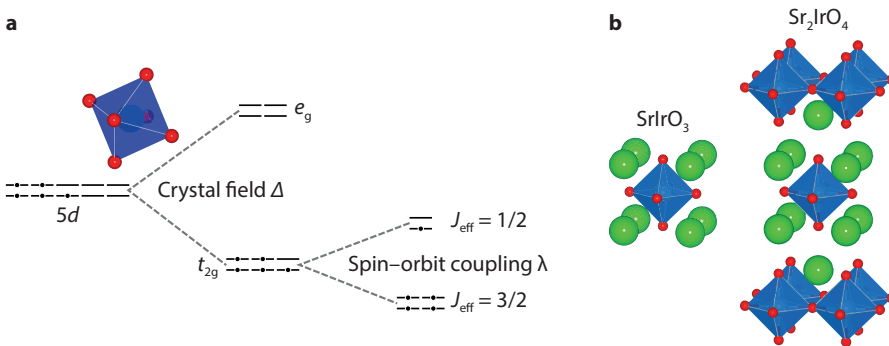


Figure 1.6: **5d level splittings in strontium iridates.** (a) Splitting of 5d energy levels by crystal field and spin-orbit coupling. (b) Crystal structure of SIO and  $\text{Sr}_2\text{IrO}_4$ .

In the 2D member  $\text{Sr}_2\text{IrO}_4$ , even a small  $U$  is sufficient to split the narrow  $J_{\text{eff}} = 1/2$  band into an upper and lower Hubbard band, resulting in a so-called spin-orbit Mott insulating state [18]. The Ir moments are antiferromagnetically coupled, but due to strong SOC, which locks the individual magnetic moments to the octahedral rotations, a weak net ferromagnetic moment appears [21, 22]. In the 3D member SIO,  $U$  is too small to open a gap but significantly reduces the density of states (DOS) at the Fermi level, resulting in a narrow-band semimetallic state [23, 24]. Theoretical calculations have suggested that SIO may be a non-trivial topological semimetal, with a Dirac nodal ring near the  $U$  point [25, 26]. Its study has been hampered by the fact that bulk SIO tends to crystallize into a  $6H$ -hexagonal structure rather than in a perovskite phase [27]. Epitaxial constraint allows for the stabilization of the perovskite phase, however in this case the Dirac cones are gapped due to the breaking of glide symmetry [24, 28].

### 1.2.3. STRONTIUM RUTHENATES

Strontium ruthenates ( $\text{Sr}_{n+1}\text{Ru}_n\text{O}_{3n+1}$ ) have been the subject of intense study for decades:  $\text{Sr}_2\text{RuO}_4$  due to its unconventional superconducting state [29, 30] and SRO due to its unusual metallic ferromagnetic state characterized by electron correlations and large magnetocrystalline anisotropy [11, 31]. SRO displays a rather unconventional anomalous Hall effect (AHE), which changes non-monotonically with temperature and even changes sign (see Fig. 1.8a). Its origin has been heavily contested and inspired many experimental and theoretical works [32–34]. Most works now agree on that the dominant mechanism for the AHE is the Berry phase effect [35], which depends on the Bloch states and their occupation. In general, ferromagnetic systems can display various types of Hall effects, which are shown in Fig. 1.7.

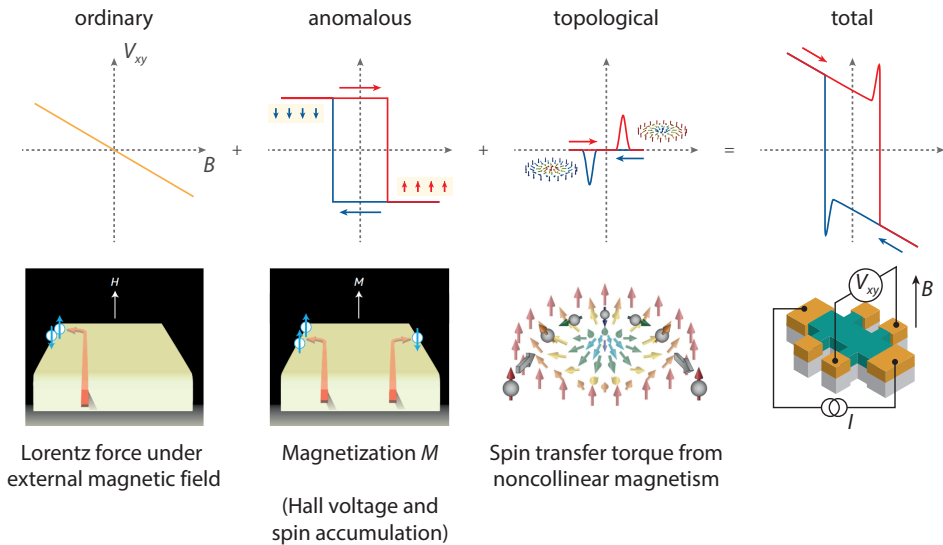


Figure 1.7: **Mechanisms responsible for Hall effects.** In magnetic systems, three mechanisms can contribute to the Hall effect. The magnetic field dependence of the Hall voltage is shown in the top, with the underlying mechanism shown below. The bottom right panel shows the measurement configuration. The three panels on the bottom left are adapted from Refs. [36, 37].

Note that the ordinary Hall effect (leftmost panel) can be nonlinear if multiple electron- and/or hole-like bands are involved in transport. In many materials, the magnitude of the AHE follows the empirical relation  $\rho_{xy} = R_0 H_z + R_s M_z$ , where  $\rho_{xy}$  is the transverse resistivity,  $R_0 H_z$  is the ordinary Hall contribution and  $R_s M_z$  represents the anomalous Hall contribution arising from the spontaneous magnetization [38]. The coefficient  $R_s$  typically depends on the resistivity  $\rho$  as  $R_s = a\rho + b\rho^2$ , where the linear term is due to spin-dependent scattering (skew scattering) [39], and the quadratic term is due to a lateral displacement during scattering (side jump scattering) [40]. These contributions are both *extrinsic* in that they depend on scattering with impurities. In 1954, Karplus and Luttinger showed that there is also an *intrinsic* contribution to the AHE that arises from the so-called “anomalous velocity” [41]. This velocity term appears in the full expression

for  $v(k)$  in addition to the usual band dispersion contribution. It originates from the Berry curvature of occupied eigenstates, which can be understood as an effective magnetic field in momentum space [42]. This effective field modifies the equation of motion of electrons and gives rise to the intrinsic AHE. The general formula for the velocity of electrons in an electric field  $\mathcal{E}$  is

$$v(k) = \frac{1}{\hbar} \frac{\partial E(k)}{\partial k} - \frac{e}{\hbar} \mathcal{E} \times b(k), \quad (1.4)$$

where  $E(k)$  is the dispersion relation and  $b(k)$  is the Berry curvature. The anomalous velocity is always transverse to the electric field, thus giving rise to a Hall voltage. For crystals with simultaneous time-reversal and spatial inversion symmetry the Berry curvature vanishes throughout the Brillouin zone. However, in systems with broken time-reversal or inversion symmetries, their proper description requires the use of the full velocity formula. The intrinsic contribution to  $\sigma_{xy}$  does not depend on  $\rho$  but on the magnetization  $M$ , and its dependence can be calculated from the band structure by using for example the Kubo formula [42]. For SRO, the Berry curvature is negligible in most regions of the momentum space but displays sharp and pronounced peaks at a (near) degeneracy or band crossing, which acts as a magnetic monopole [34]. An example is shown in Fig. 1.8b, where a sharp peak is present at the  $\Gamma$  point where the bands are nearly degenerate.

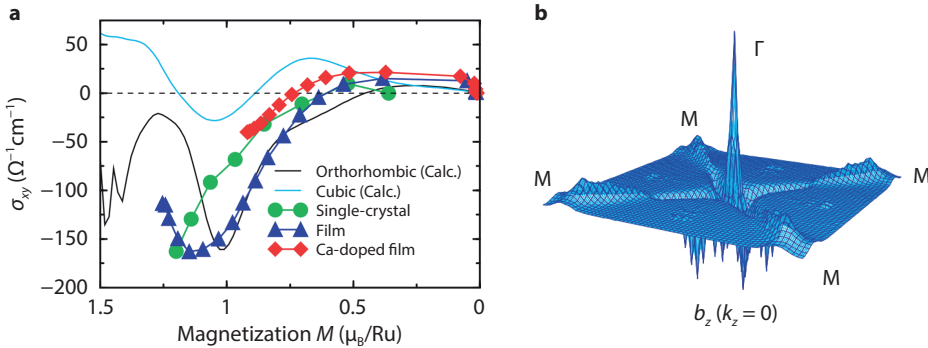


Figure 1.8: **Anomalous Hall effect of SRO.** (a) Anomalous Hall conductivity  $\sigma_{xy}$  of SRO as a function of magnetization  $M$ . Both experimental and theoretical results are shown. (b) Calculated flux distribution in  $k$ -space of the  $t_{2g}$  bands of cubic SRO. The sharp peak arises due to the (near) degeneracy of the bands, which acts as a magnetic monopole. Adapted from Ref. [34].

Recently there has been a renewal of interest in SRO films, this time in ultrathin (few u.c.) form. Several groups have reported on the observation of a topological Hall effect [43–48], which has been attributed to the presence of skyrmions: vortex-like quasi-particles (see Fig. 1.7) that can be viewed as “whirlpools” of magnetic spin [37]. The Hall effect in such systems, most notably STO/SRO/SIO, will be discussed in Chapter 6.

### 1.3. OUTLINE OF THIS THESIS

In this thesis, we study the electronic and magnetic properties of transition metal oxide thin films and heterostructures containing  $4d$  and  $5d$  elements. We focus on low-temperature electronic transport in ultrathin SIO and SRO heterostructures.

In [Chapter 2](#), we develop a procedure to obtain high-quality SIO films by taking into account the laser-induced modification of the target surface and film degradation in ambient conditions. By preparing the target surface prior to the deposition and encapsulating the films with STO, we obtain stable films that can be processed to fabricate devices such as Hall bars, which is crucial for the rest of the work presented in the thesis.

[Chapter 3](#) focuses on the semimetallic state of SIO. The partial occupation of several electron- and hole-like bands results in seemingly conflicting Seebeck and Hall coefficients. We resolve this issue by quantitatively determining the electron and hole carrier densities by combining magnetotransport and thermoelectric measurements in a field-effect geometry.

[Chapter 4](#) explores the thickness-dependent electronic properties of ultrathin SIO films. We uncover a transition from a semimetallic to an insulating state below 4 unit cells, and show that spin fluctuations are enhanced while approaching the transition point.

In [Chapter 5](#), we investigate the magnetic properties of ultrathin SIO at mK temperatures. We find that the magnetoresistance is anisotropic with respect to the magnetic field orientation, and its angular dependence reveals the presence of a fourfold symmetric component above a critical magnetic field. We attribute this transition to a field-induced magnetic state in SIO.

In [Chapter 6](#), we interface ultrathin SIO with the itinerant ferromagnet SRO, forming the tricolor STO/SRO/SIO system. Measurements of the anomalous Hall effect, which probe the Berry curvature of occupied bands, reveal the presence of two spin-polarized conduction channels. We attribute this to electronic and magnetic reconstructions at the SIO/SRO and SRO/STO interfaces, showing the potential of SIO for interface engineering.

[Chapter 7](#) explores a new method to detach thin films from their growth substrate by using an epitaxial buffer layer. Using this approach, we obtain nanomechanical resonators of high-quality freestanding STO and SRO films. By measuring the temperature dependence of their mechanical response, we observe signatures of structural phase transitions in the STO, which affect the strain and mechanical dissipation of the resonators.

[Chapter 8](#) summarizes the findings of the previous chapters and provide perspectives for future work. We discuss ongoing experiments regarding Berry phase engineering and the manipulation of freestanding thin films.

# 2

## EPITAXIAL GROWTH AND STABILITY OF SIO/STO HETEROSTRUCTURES

*Success is the ability to go from one failure to another with no loss of enthusiasm.*

*Obtaining high-quality thin films of 5d transition metal oxides is essential to explore the exotic semimetallic and topological phases predicted to arise from the combination of strong electron correlations and spin-orbit coupling. Here, we show that the transport properties of SIO thin films, grown by pulsed laser deposition, can be optimized by considering the effect of laser-induced modification of the SIO target surface. We further demonstrate that bare SIO thin films are subject to degradation in air and are highly sensitive to lithographic processing. A crystalline STO cap layer deposited in-situ is effective in preserving the film quality, allowing us to measure metallic transport behavior in films with thicknesses down to 4 unit cells. In addition, the STO encapsulation enables the fabrication of devices such as Hall bars without altering the film properties, making it possible to perform precise (magneto)transport measurements on micro- and nanoscale devices.*

---

Parts of this chapter have been published in Applied Physics Letters **109**, 041906 (2016) by D. J. Groenendijk, N. Manca, G. Mattoni, L. Kootstra, S. Gariglio, Y. Huang, E. van Heumen, and A. D. Caviglia [49].

XRD measurements were performed by S. Gariglio.

THE intriguing electronic structure of  $5d$  transition metal oxides arises from the delicate interplay between competing energy scales. Iridium compounds display a particularly large SOC of the order of 0.4 eV, which leads to the formation of novel  $J_{\text{eff}} = 1/2$  and  $J_{\text{eff}} = 3/2$  states [50]. The combination of this strong SOC and slight lattice distortions has recently drawn attention to SIO as a promising candidate to realise topological (semi)metallic phases [26, 51–54]. Perovskite SIO is a member of the  $Pbnm$  space group, featuring two glide planes and a mirror plane which are crucial in determining its band structure [25, 28]. At atmospheric pressure, SIO crystallises in a  $6H$ -hexagonal structure, while its perovskite form can be obtained by applying high pressure and temperature and subsequent quenching [55]. This requires particular care due to the high volatility of iridium oxides and competition with other phases such as  $\text{Sr}_2\text{IrO}_4$  and  $\text{Sr}_3\text{Ir}_2\text{O}_7$  [56]. These extreme conditions can be avoided by resorting to thin film growth, where epitaxial constraint can be used to synthesize perovskite SIO films [23, 24, 28, 57–63]. SIO films are generally grown by PLD, where a relatively high oxygen pressure (0.01–1 mbar) is required to control the Ir oxidation state [63]. In such high pressure conditions, the interaction dynamics between the expanding plume and the background gas are very complex [64]. This can readily result in slight deviations from the ideal film stoichiometry, which can strongly affect the electrical properties through the formation of crystal defects. Electrical transport measurements of SIO films reported in literature show a rather large variability, which brings to question the role of disorder and secondary phase formation on the film properties [59–61, 65, 66].

In this chapter, we identify key issues related to the growth and stability of SIO thin films and study how these affect their electrical properties. First, we show that the morphology and stoichiometry of the SIO target surface is progressively modified by laser ablation, reducing the growth rate and affecting the electrical properties of thin films. We then demonstrate that the transport properties of SIO films are subject to degradation over time in ambient conditions and that the films are highly sensitive to lithographic processing. These complications make it difficult to perform systematic and reproducible transport measurements. A crystalline STO cap layer deposited *in-situ* prevents film degradation and enables us to obtain metallic behavior in films with thicknesses down to 4 unit cells. In addition, the STO encapsulation preserves the film quality during lithographic processing, allowing the fabrication of Hall bars for precise (magneto)transport studies.

## 2.1. STRUCTURAL AND ELECTRONIC CHARACTERIZATION

In Fig. 2.1 we present the structural and electrical characterization of STO-capped SIO thin films deposited in optimum conditions. RHEED intensity oscillations, shown in Fig. 2.1a, are observed for both the 20 u.c. SIO film and the 10 u.c. STO cap layer and can be used to determine the growth rate. Figure 2.1b shows an XRD measurement around the (001) reflection (pseudocubic notation) of an STO-capped 30 u.c. SIO film. The clear finite size oscillations and the small FWHM of the rocking curve ( $0.06^\circ$ , Fig. 2.1b, inset) evidence long-range crystalline order. Additional XRD measurements, such as reciprocal space mapping, show that the film is coherently strained on the substrate (see Fig. 2.4). Measurements over a larger  $2\theta$  range indicate that, in these growth conditions, no secondary phases are formed. The film thickness extracted from the fit (12 nm, solid line)

is in good agreement with the number of unit cells estimated from RHEED and is confirmed by X-ray reflectivity. The resulting  $c$ -axis parameter is  $4.08\text{\AA}$ , which is consistent with the expected value taking into account the compressive strain from the STO substrate (+1.54%) and imposing the conservation of the bulk u.c. volume.

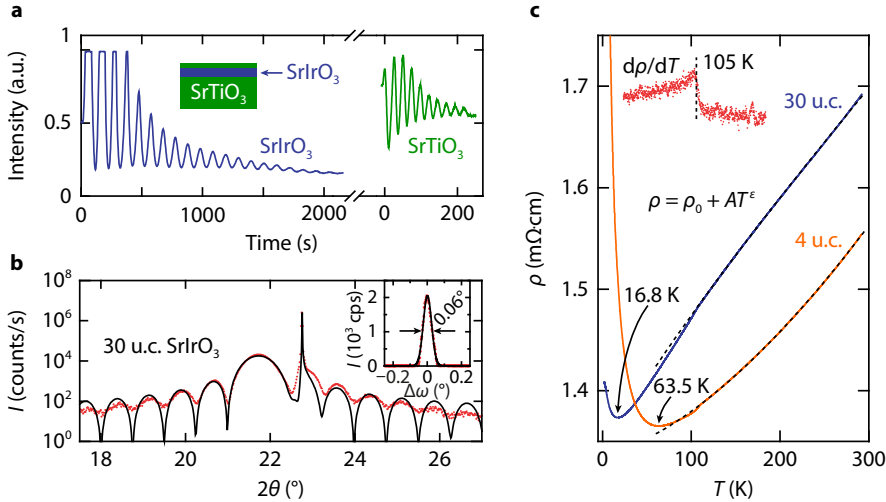


Figure 2.1: **Growth and characterization of SIO/STO heterostructures.** (a) RHEED intensity oscillations of the specular spot during the growth of a 20 u.c. SIO film with a 10 u.c. STO cap layer. (b) XRD scan around the (001) reflection (pseudocubic notation) of an STO-capped 30 u.c. SIO film. Inset: rocking curve around the SIO(001) reflection. (c) Resistivity versus temperature of STO-capped SIO films with thicknesses of 30 u.c. (blue line) and 4 u.c. (orange line). The dashed lines are fits to the data from room temperature to 105 K. The inset shows  $d\rho/dT$  of the 30 u.c. film, where a change of the slope occurs at 105 K.

Figure 2.1c shows the temperature dependence of the resistivity ( $\rho$ ) of two STO-capped SIO films with thicknesses of 30 u.c. (blue line) and 4 u.c. (orange line). In overall agreement with literature, the resistivity of the 30 u.c. film decreases slightly with decreasing temperature and displays a small upturn at low temperature [59–61, 65, 66]. The small resistivity variation over the entire temperature range can be a signature of the semimetallic ground state reported in recent angle-resolved photoemission spectroscopy (ARPES) studies [23, 24]. Interestingly, we observe a slight change of slope at 105 K, which is reproducible across different samples and thermal cycles and is most likely related to the cubic–tetragonal structural transition of the STO substrate [67]. This transition involves a rotation of the oxygen octahedra, shortening the in-plane lattice parameters and increasing the  $c$ -axis of the STO [68]. Such cross-interface coupling has previously been observed for ultrathin correlated  $\text{La}_{1-x}\text{Sr}_x\text{MnO}_3$  (LSMO) films on STO, where a soft phonon mode, whose amplitude diverges at the STO phase transition, propagates into the atomic layers of the LSMO film and modifies its electronic properties [69]. The detection of this slight structural distortion in the electronic properties of the SIO film is a fingerprint of the high quality of the interface, enabling the coupling between octahedral rotations of the substrate and the thin film. In addition, it demonstrates how sensitive the electric properties of SIO thin films are to octahedral rotations.

Despite its small thickness, the 4 u.c. film still shows metallic behavior and has a resistivity comparable to the 30 u.c. film. The resistivity shows an upturn at higher temperature, below which it increases up to approximately  $2.4 \text{ m}\Omega\text{cm}$  at 1.5 K. Films with thicknesses below 4 u.c. were found to display insulating behavior. The resistivity versus temperature data is fit from room temperature to 105 K by  $\rho(T) = \rho_0 + AT^\varepsilon$  (dashed lines). Details regarding the data fitting are presented in Fig. 2.5. In previous reports on SIO films, the temperature exponent  $\varepsilon$  and upturn temperature  $T_{\min}$  were considered as a measure of the film metallicity [62, 66]; here, we obtain  $\varepsilon = 0.9$ ,  $T_{\min} = 16.8 \text{ K}$ , and  $\varepsilon = 1.6$ ,  $T_{\min} = 63.5 \text{ K}$  for the 30 and 4 u.c. films, respectively. Literature reports of  $T_{\min}$  for film thicknesses between 7 and 35 nm vary from 25 K up to 175 K [59–61, 65, 66]. In the following, we will show that  $\varepsilon$  and  $T_{\min}$  are both affected by the progressive laser-induced modification of the target surface and film degradation in air over time.

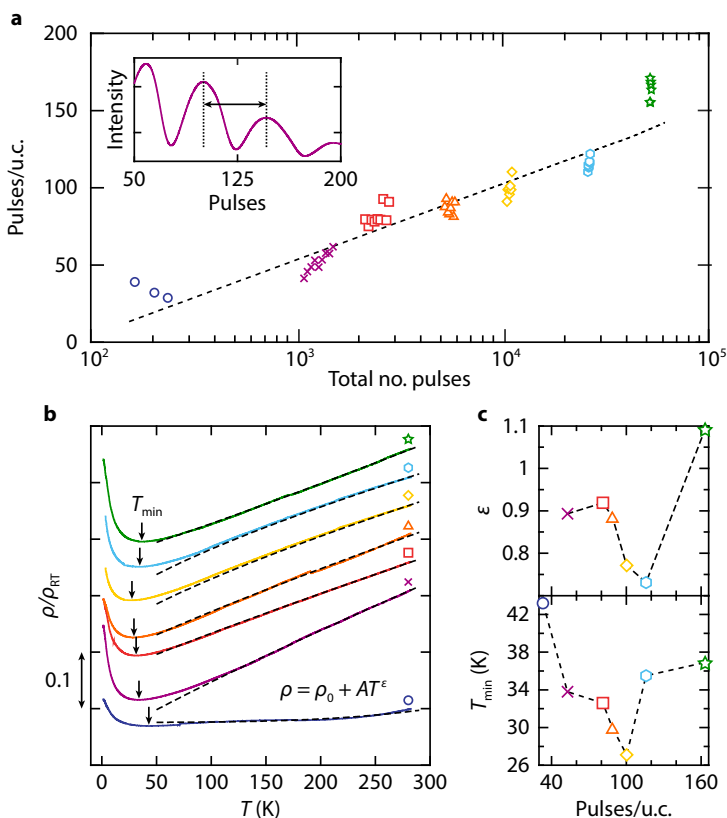


Figure 2.2: **Target surface modification and electronic properties.** (a) Pulses per u.c. estimated from RHEED intensity oscillations during the growth of a series of 10 u.c. SIO films. The inset shows the estimation of the number of pulses/u.c. from the period of the oscillations. (b) Resistivity versus temperature curves of the films shown in panel (a). The curves are rescaled to their room-temperature resistivity values and offset for clarity. (c) Parameters extracted from the  $\rho(T)$  curves as a function of the average number of pulses/u.c.

## 2.2. LASER-INDUCED TARGET SURFACE MODIFICATION

To study how the growth and the electrical properties are affected by the modification of the target surface, a series of seven 10 u.c. SIO films were deposited consecutively. The target was pre-ablated in deposition conditions with an increasing number of pulses between depositions to mimic the extended use of the target. Figure 2.2a shows the number of pulses per u.c. extracted from the period of the RHEED oscillations as indicated in the inset. The entire set of oscillations is shown in Fig. 2.6a. After 50,000 pulses incident on the rotating target, the number of pulses per u.c. increases from 29 to 171. The reduction of the deposition rate can visually be recognized as an increased reflectance of the target surface and a progressive decrease of the plume size. Such a decrease in deposition rate has previously been reported for SIO and  $\text{YBa}_2\text{Cu}_3\text{O}_{7-x}$  thin films and was related to stoichiometric and morphological changes of the target surface [58, 70]. We observe a similar change of target surface morphology by the formation of conical structures which align along the incoming laser direction, of which scanning electron microscopy (SEM) images are shown in Fig. 2.6b. This modification of the target surface was observed not only for  $1 \text{ J/cm}^2$ , but for different fluences ranging from  $0.4$  to  $2.0 \text{ J/cm}^2$ . These conical structures were previously shown to be Ir-rich, indicating that the change in surface morphology is related to an Ir-enrichment of the target surface [58]. To corroborate this, we performed energy-dispersive X-ray spectroscopy (EDX) spectroscopy measurements on the target, finding a decrease of the Sr/Ir ratio of about 5% after 240 pulses incident on the same site (see Fig. 2.7).

The resistivity versus temperature characteristics of the seven 10 u.c. films are presented in Fig. 2.2b. The curves are normalized to their room temperature resistivity values and offset for clarity. Despite the significant decrease of the deposition rate, the resistivity and overall transport behavior of the thin films are comparable. The data is fit down to 105 K (dashed lines) to extract the temperature exponent  $\epsilon$ . As shown in Fig. 2.2c, both  $\epsilon$  and  $T_{\min}$  vary slightly and show a non-monotonic dependence on the deposition rate, displaying a minimum at approximately 100 pulses/u.c. We attribute this to an evolution of the film stoichiometry originating from the interplay between the target surface modification and the preferential scattering of lighter species. As previously reported and suggested by our EDX measurements, the laser ablation causes a progressive Ir-enrichment of the initially stoichiometric target surface, resulting in a crossover from a Sr- to Ir-rich plasma plume as the number of pulses increases. The high background pressure can partially compensate for the incongruent ablation by preferential scattering of the lighter Sr atoms, as has previously been observed for the PLD growth of homoepitaxial STO [71]. In this picture, the minima in Fig. 2.2c are indicative of a film with near-ideal stoichiometry, and the increase of  $\epsilon$  and  $T_{\min}$  on either side of the minima demonstrates that a slight imbalance in the Sr/Ir ratio can directly affect the electrical properties of SIO thin films. Films with optimum electrical properties can be obtained reproducibly by grinding the target surface prior to deposition and performing an in-situ pre-ablation in the growth conditions with a fixed number of pulses. Microscopically, cation off-stoichiometry often results in an expansion of the  $c$ -axis arising from clustering of Sr vacancies or the inclusion of  $\text{IrO}_2$  planes (on the Ir-rich side), or from the inclusion of SrO planes (on the Sr-rich side) [72]. XRD or TEM studies could shed light on how such defects or stacking faults influence the transport properties of thin films.

### 2.3. FILM DEGRADATION IN AMBIENT CONDITIONS

We further found that bare SIO films are subject to degradation in ambient conditions. Over time, films suffer from a loss of conductivity and shift towards insulating behavior. We monitored the progressive degradation of the transport properties by measuring resistivity versus temperature characteristics of a bare 10 u.c. SIO film over the course of 40 days. In the time between measurements, the film was stored in ambient conditions. Figure 2.3a shows the  $\rho(T)$  characteristics measured at different times (red lines) from which we extracted the time evolution of  $\varepsilon$  and  $T_{\min}$ . The change from metallic to insulating behavior is reflected by an increase of the temperature exponent  $\varepsilon$  and of  $\Delta T_{\min}$ , defined as  $T_{\min}(t) - T_{\min}(t = 0)$  (Fig. 2.3a, inset). After 40 days, the metallicity is completely lost: the resistivity monotonically increases with decreasing temperature, and the curve can no longer be fit to the power law behavior to extract the temperature exponent. We note how different  $\rho(T)$  characteristics and values of  $\varepsilon$  and  $T_{\min}$  resemble the scatter of data reported in literature so far; it is thus possible that film degradation is one of the origins of their large variability.

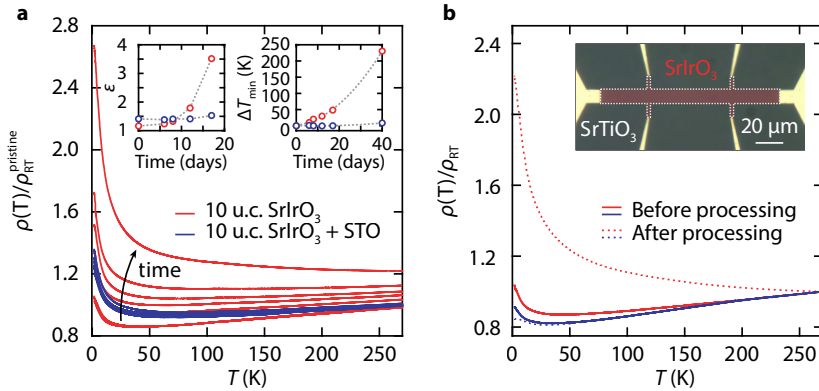


Figure 2.3: **Degradation of SIO films.** (a)  $\rho(T)$  curves of two 10 u.c. SIO films, with (blue line) and without (red line) STO cap layer. The curves were measured for both samples simultaneously over a period of 40 days. The resistivity values are rescaled to the room-temperature resistivity of the measurement on day 0. The inset shows the variation of  $\varepsilon$  and the upturn temperature  $\Delta T_{\min}$  as a function of time. (b)  $\rho(T)$  curves of 14 u.c. films with and without STO cap layers before (solid lines) and after (dashed lines) lithographic processing. Inset: optical image of a capped SIO film patterned into a Hall bar by Ar dry etching.

A more abrupt change of the transport properties was observed when standard lithographic processing was performed (as described in Methods). Figure 2.3b shows rescaled  $\rho(T)$  curves of a bare SIO film (red lines), where the metallic behavior is completely lost after processing. The inability to pattern samples poses a serious roadblock to quantitative magnetotransport characterization of thin films, for which devices such as Hall bars are required. We prevented the degradation of SIO films by the *in-situ* deposition of a crystalline STO cap layer with a thickness of 15 unit cells. The addition of this cap layer preserves the electrical properties over time and enables lithographic processing. Figures 2.3a and 2.3b show the striking difference for the capped film (blue lines), where the  $\rho(T)$  characteristics remain unchanged and  $\varepsilon$  and  $T_{\min}$  are approximately constant. It is

possible that chemical decomposition occurs when bare films are stored in air or when lithography is performed, however no further studies have been performed on this issue.

We also found that encapsulation with amorphous STO yields stable films with no significant differences in their transport behavior, indicating that the choice of cap layer is not limited to crystalline STO (see Fig. 2.8). This flexibility is particularly interesting considering that a crystalline STO cap layer imposes structural constraints to the film and restores a broken inversion symmetry, which could potentially affect its electrical properties. We did not observe significant differences in their  $\rho(T)$  behavior, yet more detailed measurements are required to understand whether the electronic structure of the SIO films is affected by the presence of a crystalline STO cap layer.

## 2.4. CONCLUSIONS

We demonstrated the growth of high-quality epitaxial SIO thin films on STO substrates by PLD. Despite the continuous decrease of the growth rate due to the laser-induced modification of the target surface, the transport behavior of films deposited in different pre-ablation conditions was found to be comparable. The temperature exponent  $\varepsilon$  and the upturn temperature of the films varied slightly, showing a non-monotonic dependence on the growth rate which we attributed to a crossover from Sr- to Ir-rich films. We further demonstrated how thin films suffer from degradation of their electrical properties in ambient conditions and after lithographic processing. The addition of an STO cap layer deposited *in-situ* resulted in stable electrical properties over time and enabled us to measure metallic transport behavior in patterned films with thicknesses down to 4 unit cells. The sensitivity of the electrical properties of SIO thin films to slight deviations in stoichiometry and exposure to ambient conditions underlines the particular care that is required in their growth, characterization and processing.

## 2.5. METHODS

### FILM GROWTH

SIO and STO films were deposited on commercially available  $\text{TiO}_2$ -terminated (001)STO substrates (CrysTec GmbH) by PLD using a KrF excimer laser (Coherent COMPexPro 205, KrF 248 nm). An energy density of  $1 \text{ J/cm}^2$  and a repetition rate of 1 Hz were used. The laser spot size was  $2.5 \text{ mm}^2$ , corresponding to a dose of  $25 \text{ mJ/pulse}$ . The target was rotated during ablation such that the total ablated area forms a ring of  $70 \text{ mm}^2$ . The incident angle of the laser on the target surface was  $45^\circ$  and the target-substrate distance was set to 55 mm. The depositions were performed in an oxygen pressure of 0.1 mbar and with a substrate temperature of  $700^\circ\text{C}$  as measured with an optical pyrometer. The growth conditions used in this work are comparable to those adopted most commonly in literature [59–61, 65]. The relatively high oxygen pressure is required due to the noble metal character of Ir, and causes the plume front to reach a stationary state after approximately 25 mm [63, 64]. The diffusive propagation of the ablated species beyond this distance strongly reduces the deposition rate and can affect the film stoichiometry by preferential scattering of lighter elements with the background gas [71]. In this regime, the kinetic energy of the species is of the order of the thermal energy, which is lower than the activation energy for surface diffusion of adatoms and can affect the

growth mode [73]. The growth was monitored by *in-situ* RHEED. After the growth, the samples were annealed in an oxygen pressure of 300 mbar for 1 hour and cooled down to room temperature in approximately 2 hours to compensate for possible oxygen deficiency. Single-crystal STO and ceramic SIO targets were used. The SIO target was sintered in a sealed container at 950°C for 12 hours, followed by 24 hours at 1050°C. Before use, the target surface was ground with fine grit sandpaper.

## FABRICATION & CHARACTERIZATION

XRD data was acquired using a PANalytical X-PertPRO MRD equipped with a monochromator. Resistivity measurements on the samples shown in Fig. 2.1c were performed in a Hall bar geometry fabricated by Ar dry etching and e-beam evaporation of metal contacts, while the measurements shown in Fig. 2.2b and Fig. 2.3 were performed in a van der Pauw configuration. Electrical contact was established by ultrasonic wire bonding with AlSi bonding wire. The resistivity measurements were performed in a flow cryostat with a base temperature of 1.5 K. The lithographic processing relied on the use of polymethyl methacrylate (PMMA) resists and standard chemicals such as acetone and isopropyl alcohol.

## 2.6. SUPPLEMENTARY INFORMATION

### 2.6.1. ADDITIONAL X-RAY DIFFRACTION MEASUREMENTS

Figure 2.4a shows an XRD scan of an STO-capped 30 u.c. SIO film, where the (001) to (004) Bragg reflections (pseudocubic notation) of the film can be identified. The finite size oscillations evidence long-range crystalline order. No additional peaks from secondary phases are present.

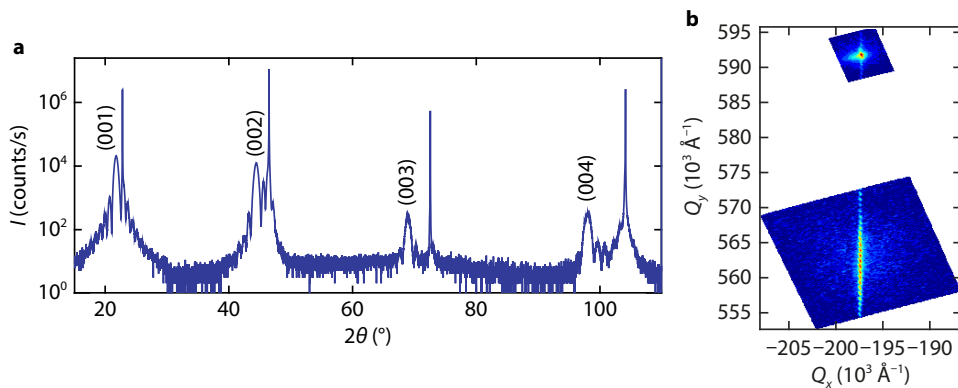


Figure 2.4: **XRD characterization of an STO-capped 30 u.c. SIO film.** (a)  $\theta$ - $2\theta$  scan confirming the films are single-phase SIO. (b) Reciprocal space map showing the STO(103) and SIO(103) reflections (pseudocubic notation).

Figure 2.4b shows a reciprocal space map around the STO(103) and SIO(103) reflections (pseudocubic notation), showing that the SIO film is coherently strained on the STO substrate.

### 2.6.2. MODELING OF RESISTIVITY–TEMPERATURE DATA

Figure 2.5 shows the results from the fitting of the resistivity versus temperature data shown in Fig. 2.1c. The data was fit to  $\rho = \rho_0 + AT^\epsilon$ . To verify the reliability of the fit, different temperature ranges were selected. The data was fit from room temperature down to  $T_{\min}^{\text{fit}}$ , where  $T_{\min}^{\text{fit}}$  ranges from 85 K to 170 K. The change of slope at 105 K is clearly visible in the fitting parameters. To not include the difference in behavior below 105 K, the  $\rho(T)$  data in Figs. 2.1 to 2.3 was fit from room temperature to 105 K. The coherent behavior above this temperature is shown by the saturation of the fitting parameters when approaching 105 K.

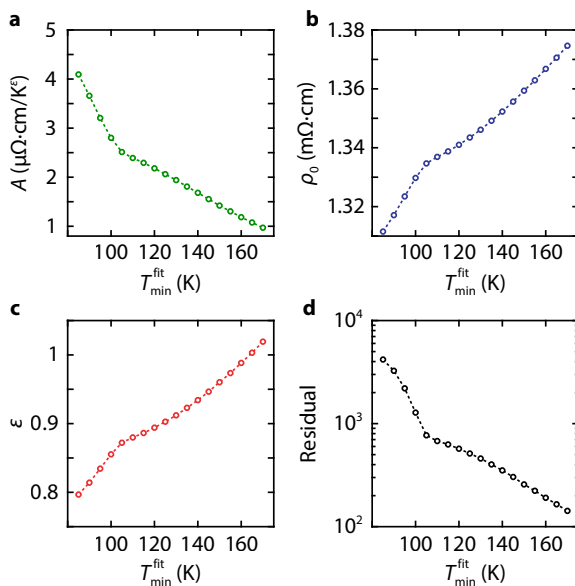


Figure 2.5: Fitting parameters as a function of  $T_{\min}^{\text{fit}}$ .

### 2.6.3. GROWTH RATE AND TARGET SURFACE MORPHOLOGY

To study the influence of the laser-induced surface modification of the target on the growth rate, the target was pre-ablated in deposition conditions with an increasing number of pulses between depositions. Figure 2.6a shows the RHEED intensity oscillations during the growth of the SIO films presented in Fig. 2.2. The numbers next to the curves correspond to the total number of pulses the target has received prior to the deposition of the thin film. As the total dose the target has received increases, the number of pulses required to grow a single unit cell increases. Figure 2.6b shows SEM images of the target surface before (left) and after (right) laser ablation. In the panel on the right, the target surface has received 240 pulses/site with an energy density of  $1 \text{ J}/\text{cm}^2$ . We observe cone-like structures that are aligned to the incoming laser direction (yellow arrow) to which we attribute the decrease of the deposition rate.

EDX spectroscopy was used to measure the change of stoichiometry of the SIO target

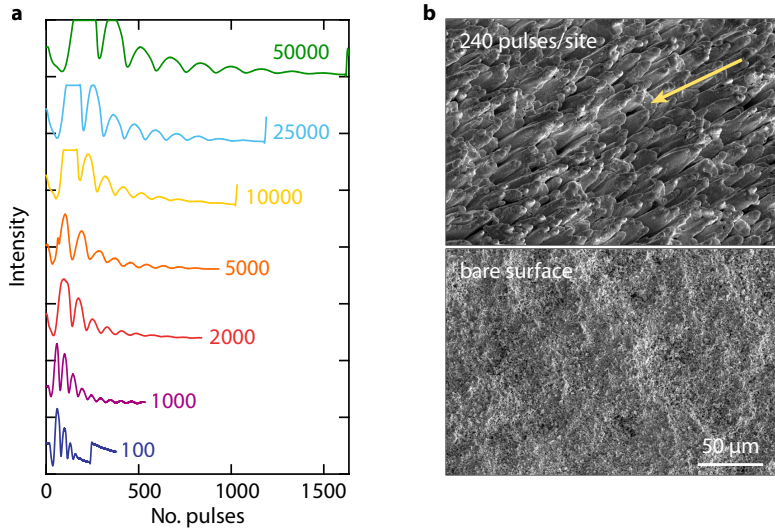


Figure 2.6: **Gradual change of the growth rate and target surface morphology.** (a) RHEED intensity oscillations of the seven 10 u.c. SIO films shown in Fig. 2.2. The number refers to the total number of pulses the target has received prior to the corresponding deposition. (b) SEM images of the surface after 240 pulses/site at  $1 \text{ J/cm}^2$  (top) and the bare target surface (bottom). The arrow indicates the incoming laser direction. The scale bar is equal for both images.

surface. Figure 2.7 shows the ratio of the atomic weight percentages of Sr and Ir as a function of the total dose that the target has received. A trend of Ir-enrichment was observed for increasing number of pulses (120 and 300 pulses for  $2 \text{ J/cm}^2$ ). For a fluence of  $1 \text{ J/cm}^2$ , we measured a decrease of the Sr/Ir ratio of about 5% after 240 pulses incident on the same site.

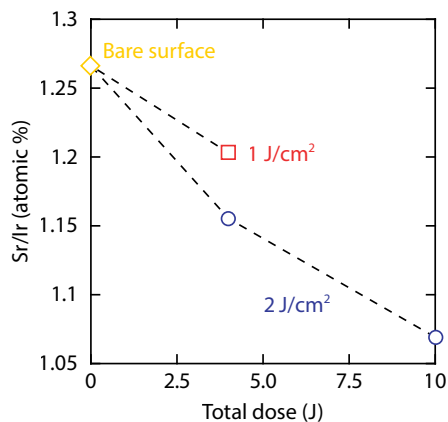


Figure 2.7: **Progressive Ir-enrichment of the SIO target surface.** Sr/Ir ratio as a function of the total dose that the target surface has received.

#### 2.6.4. PRESERVATION OF THE FILM PROPERTIES BY STO ENCAPSULATION

Figure 2.8 shows resistivity versus temperature characteristics of three 6 u.c. SIO films without cap layer (red line), with an amorphous STO (a-STO) cap layer (black line), and with a crystalline STO (c-STO) cap layer (blue line). All films were exposed to air only during the time required for the preparation of the sample for transport measurements (approximately one hour) and the measurements were performed in van der Pauw configuration.

2

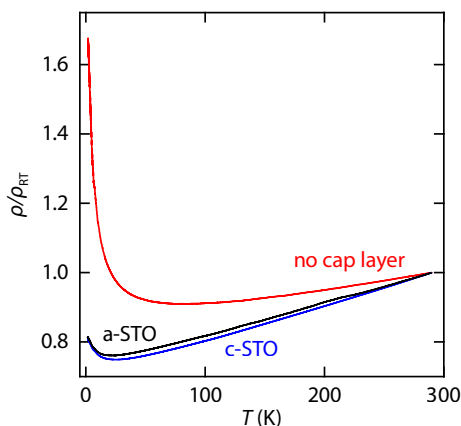


Figure 2.8: **Encapsulation with amorphous STO.**  $\rho(T)$  measurements of 6 u.c. SIO films without cap layer (red line), with an amorphous STO cap layer (a-STO, black line), and with a crystalline STO cap layer (c-STO, blue line).

Both the films with the amorphous and crystalline STO cap layer display metallic behavior with a resistivity upturn around 23 K. The structural constraints imposed by the crystalline STO cap layer do not appear to significantly affect the  $\rho(T)$  behavior. However, the 6 u.c. film without STO cap layer is clearly more insulating than the encapsulated films, showing an upturn of the resistivity at approximately 83 K. This confirms that a cap layer is required to prevent film degradation and measure the intrinsic electrical properties of ultrathin films.



# 3

## BALANCED ELECTRON-HOLE TRANSPORT IN SIO/STO HETEROSTRUCTURES

*Why is this thus? What is the reason of this thusness?*

Artemus Ward

*SIO hosts parabolic bands of heavy holes and light electrons in gapped Dirac cones due to the interplay between electron–electron interactions and spin–orbit coupling. The partial occupation of multiple bands results in properties that are seemingly in contrast with one another, complicating the extraction of their transport coefficients. In this chapter, we present a multifold approach relying on different experimental techniques and theoretical calculations to disentangle its complex electronic properties. By combining magnetotransport and thermoelectric measurements in a field-effect geometry with first-principles calculations, we quantitatively determine the transport coefficients of the different conduction channels. Despite their different dispersion relationships, electrons and holes are found to have strikingly similar transport coefficients, yielding a hole-like response under field-effect and thermoelectric measurements and a linear electron-like Hall effect up to 33 T.*

---

Parts of this chapter have been published in Physical Review B **97**, 081105(R) (2018) by N. Manca, D. J. Groenendijk, I. Pallecchi, C. Autieri, L. M. K. Tang, F. Telesio, G. Mattoni, A. McCollam, S. Picozzi, and A. D. Caviglia [74].

Thermoelectric measurements were performed by I. Pallecchi and F. Telesio. L. M. K. Tang and A. McCollam assisted with the high-field measurements at the High Field Magnet Laboratory in Nijmegen. Theoretical results were obtained by C. Autieri and S. Picozzi.

Oxide heterostructures have been intensely studied in recent years as a versatile platform for controlling electronic properties of materials [1]. Charge transfer, strain engineering and polar instabilities are part of the toolbox available at oxide interfaces for controlling phases of matter, such as 2D superconductors and various magnetic ground states. Although the manipulation of broken symmetries is a well-developed topic in the field, experimental control of topological phases at oxide interfaces has so far been elusive. Symmetry-protected boundary states in oxide heterostructures have been considered theoretically as a promising route to realize novel topological materials. Much attention has been focused on SIO and its heterostructures as candidates for correlated topological insulators [75, 76], topological semimetals [77, 78], topological Hall effect [60] and unconventional superconductors [79–81]. In its bulk form this material exhibits a nodal line at the  $U$  point and characteristic transport signatures of Dirac electrons, such as large and linear magnetoresistances [25, 26, 82]. However, when synthesised as an epitaxial thin film, SIO shows transport characteristics that are inconsistent with this picture and not yet understood, including a linear and strongly reduced magnetoresistance [61, 62]. ARPES measurements show that the degeneracy at the Dirac points is lifted, leading to a Fermi surface with pockets of light electrons together with heavy holes [23, 24]. XRD studies have correlated this modification of the electronic structure to an epitaxially stabilised lattice distortion that breaks the orthorhombic bulk symmetry [28, 83]. An understanding of the charge and transport properties of this correlated semimetal is a fundamental step for the realization of topological phases in oxide heterostructures and is developed here.

In this chapter, we report on an extensive characterization of the transport properties of SIO/STO heterostructures by combined field-effect, magnetotransport and thermoelectric measurements. Numerical analysis, supported by first principles calculations, accounts for the coexistence of an electron-like Hall effect and a hole-like electrical conductivity and thermopower. The emerging picture of a compensated semimetallic state harmonizes transport and spectroscopic data.

### 3.1. BACK-GATE MODULATION OF MAGNETOTRANSPORT

We first investigate how the resistance of SIO films is modified by the application of a back-gate voltage ( $V_{BG}$ ), which can modulate the carrier density through field-effect. This technique is often used in low-density 2D systems and semiconductors to tune the carrier density and consequently the resistance. Figure 3.1a shows  $R(T)$  characteristics of SIO films with thicknesses ranging from 3 to 6 u.c. (solid lines). As recently reported, a metal–insulator transition occurs between 4 and 3 u.c., and bulk-like electrical resistivity is reached above 6 unit cells [84, 85]. The dashed  $R(T)$  curves in Fig. 3.1a show that the resistance is significantly reduced by the application of  $V_{BG} = -180$  V, indicative of the low carrier density of this system. The field-effect efficiency decreases with increasing thickness, and above 6 u.c. the  $R(T)$  curves measured with  $V_{BG} = 0$  V and  $V_{BG} = -180$  V are indistinguishable. The manner in which the electric field affects the  $R(T)$  characteristics provides a first hint of the carrier type of the system: a negative  $V_{BG}$  lowers the resistance, as expected from a conductor with hole-like carriers. Figure 3.1b shows the relative variation of  $R$  for films of different thicknesses as  $V_{BG}$  is varied at 1.5 K. A hole-like response is observed for all film thicknesses, irrespective of the semiconducting or

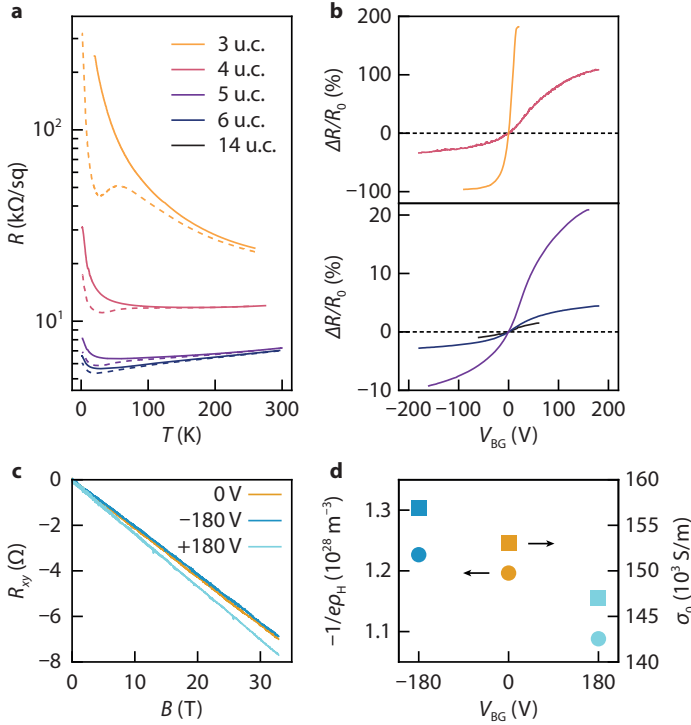


Figure 3.1: **Transport characterization of SIO thin films.** (a)  $R(T)$  of SIO films of different thicknesses measured at  $V_{BG} = 0$  V (the solid lines) and  $V_{BG} = -180$  V (dashed lines). (b) Relative variation of  $R$  as a function of  $V_{BG}$  measured at 1.6 K. (c) Hall resistance of a 6 u.c. SIO film for different values of  $V_{BG}$  at 1.5 K. (d) Carrier density (circles) and conductivity  $\sigma_0$  (squares) as a function of  $V_{BG}$  in a single band model.

metallic behavior [84]. The back-gate is able to induce a larger resistance change for lower SIO thicknesses due to reduced screening, and for the 3 u.c. film we can even induce a fully insulating state (Fig. 3.1b). A small response is observed for the 14 u.c. film, which shows a variation of the order of a few percent. We note that the response to the back-gate is mediated by the dielectric constant of the STO substrate ( $\epsilon_r^{\text{STO}}$ ). Its non-linear temperature and electric field dependence can account for the non-monotonic behavior of the  $R(T)$  curves with applied  $V_{BG}$  (see Fig. 3.1a) and for the reduced field-effect efficiency at high voltages (see Fig. 3.1b) [86, 87]. In Fig. 3.5 we provide further evidence of a hole-dominated electrical conductivity by modulating the concentration of oxygen vacancies.

Previous reports have shown that the Hall effect of SIO is negative and linear [61], which is seemingly at odds with the hole-like field-effect response. We investigate this further by measuring the 6 u.c. film, as its small thickness permits strong tunability by field-effect while it is sufficiently conductive and homogeneous for precise measurements at low temperatures. The Hall effect measured at 1.6 K for three different values of  $V_{BG}$  is presented in Fig. 3.1c. It is linear and negative up to 33 T, as would be observed

in a system dominated by a single band of electrons. However, the field-effect response of the Hall signal ( $\rho_H$ ) and conductivity at zero magnetic field ( $\sigma_0$ ) show that this simple picture is inadequate (see Fig. 3.1d). Despite its negative slope, the Hall signal responds to the back-gate as if electrical transport is dominated by hole-like carriers. Furthermore, the carrier density calculated in a single band picture ( $1/e\rho_H \approx 10^{28} \text{ m}^{-3}$ ) would render the back-gate ineffective due to large screening. The discrepancy between Hall and field-effect data is therefore a clear indication of the multiband character of this system. In a transport model with an electron- and hole-like channel, the Hall resistivity is given by

$$\rho_H \equiv \frac{tR_{xy}}{B} = \frac{1}{e} \frac{n_h \mu_h^2 - n_e \mu_e^2 + (n_h - n_e)(\mu_h \mu_e B)^2}{\sigma_0^2 / e^2 + (n_h - n_e)^2 (\mu_h \mu_e B)^2}, \quad (3.1)$$

where

$$\sigma_0 = \sigma_h + \sigma_e = e(n_h \mu_h + n_e \mu_e), \quad (3.2)$$

and  $t$  is the film thickness,  $R_{xy}$  the Hall resistance,  $e$  the elementary charge,  $B$  the magnetic field,  $n$  the carrier density,  $\mu$  the mobility, and  $e$  and  $h$  indicate electrons and holes, respectively. Since the measured Hall effect in Fig. 3.1c is linear and negative, we can approximate Eq. (3.1) with its low-field limit:

$$\rho_H = \frac{e}{\sigma_0^2} (n_h \mu_h^2 - n_e \mu_e^2). \quad (3.3)$$

Standard analysis on two-band systems is based on the combined measurement of  $\sigma_0$  and  $\rho_{xy}$ , where the presence of inflection points in  $\rho_{xy}(B)$  provides a powerful constraint for the determination of  $n_{e,h}$  and  $\mu_{e,h}$ . For SIO, such inflection points are likely out of the probed range ( $\pm 33 \text{ T}$ ), and the parameters can therefore not be determined in this manner.

### 3.2. TEMPERATURE-DEPENDENT THERMOELECTRIC RESPONSE

Thermoelectric measurements can provide complementary information to magneto-transport, allowing us to determine the transport coefficients of the different bands. For this experiment, we prepared a dedicated series of samples with dimensions of  $10 \times 5 \text{ mm}^2$  and thicknesses of 6, 14 and 20 unit cells. Films with thicknesses below 6 u.c. were not measurable due large contact resistances at low temperatures. We measured the Seebeck coefficient ( $S$ ) of the three SIO films as a function of thickness, temperature, and magnetic field (Fig. 3.2a). All films show a nearly constant positive value  $S \approx 10\text{--}20 \text{ } \mu\text{V/K}$  above 150 K and a linear decrease below 70 K. As opposed to bulk SIO [88], the Seebeck coefficient of SIO thin films does not show multiple sign changes, indicating a drastically different electronic structure. Another difference is the absence of any  $B$  dependence of the thermoelectric response, indicating that the Seebeck effect is dominated by the diffusive mechanism. The high ( $> 150 \text{ K}$ ) and low ( $< 70 \text{ K}$ ) temperature regimes are well described by the Heikes [89] and Mott [90] formulas respectively, which provide a direct relationship between the measured quantities and the material properties. For each

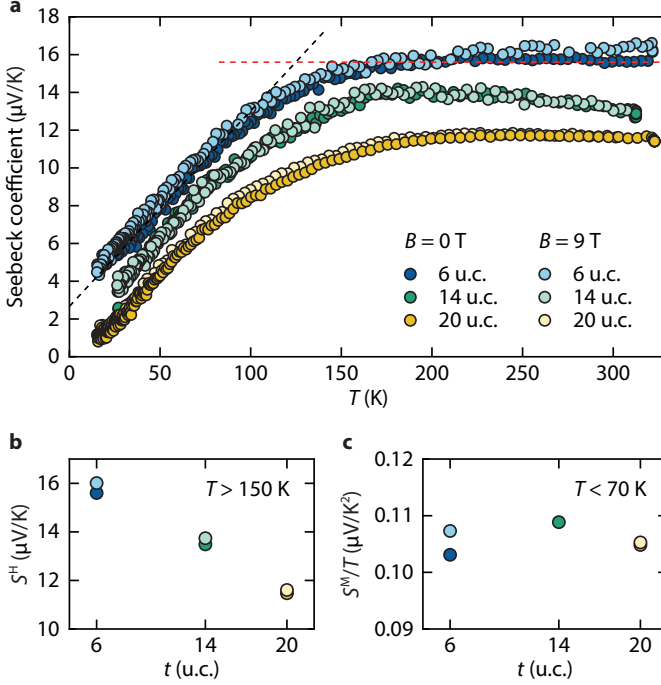


Figure 3.2: **Thermoelectric characterization of SIO thin films.** (a) Seebeck coefficient as a function of temperature, thickness, and magnetic field. (b) Heikes and (c) Mott Seebeck coefficients calculated using Eqs. 3.4 and 3.5, respectively. The dashed lines in (a) are linear fits used to calculate the Seebeck coefficients in (b) (red dashed line) and (c) (black dashed line), corresponding to the high ( $> 150\text{ K}$ ) and low ( $< 70\text{ K}$ ) temperature regimes, respectively.

electron- or hole-like band, the Heikes ( $S^H$ ) and Mott ( $S^M$ ) Seebeck coefficients are given by

$$S_{h/e}^H = \pm \frac{k_B}{e} \log\left(\frac{2 - n\nu}{n\nu}\right), \quad (3.4)$$

$$S_{h/e}^M = \pm \left(\frac{3}{2} - \alpha\right) \left(\frac{2(2\pi)^8}{3^5}\right)^{1/3} \frac{k_B^2}{e\hbar^2} \frac{m^*}{n^{2/3}} T, \quad (3.5)$$

where  $k_B$  is the Boltzmann constant,  $\hbar$  is the reduced Planck constant,  $\nu$  is the unit cell volume,  $\alpha$  is a parameter related to the scattering mechanisms ( $0 \leq \alpha \leq 1$ ),  $m^*$  is the effective mass of the carriers and the  $\pm$  sign corresponds to holes or electrons, respectively. In a multiband model, the total Seebeck coefficient in the diffusive regime can be expressed as

$$S = \frac{e}{\sigma_0} (n_h \mu_h |S_h| - n_e \mu_e |S_e|). \quad (3.6)$$

This, in combination with Eqs. (3.4) and (3.5) allows us to write the Seebeck coefficient in the two temperature regimes as

$$S^H = \frac{k_B}{\sigma_0} \left( n_h \mu_h \log \left( \frac{2 - n_h v}{n_h v} \right) - n_e \mu_e \log \left( \frac{2 - n_e v}{n_e v} \right) \right), \quad (3.7)$$

$$S^M = \frac{e}{\sigma_0} \xi \left( n_h^{1/3} \mu_h m_h^* - n_e^{1/3} \mu_e m_e^* \right) T, \quad (3.8)$$

where  $\xi$  is the numerical pre-factor appearing in Eq. (3.5):

$$\xi = \left( \frac{3}{2} - \alpha \right) \left( \frac{2(2\pi)^8}{3^5} \right)^{1/3} \frac{k_B^2}{e\hbar^2}.$$

The experimental values for  $S^H$  and  $S^M/T$  are presented in Figs. 3.2b and 3.2c as a function of the film thickness, where  $S^H$  is the average of  $S$  above 150 K and  $S^M/T$  is determined from a linear fit of  $S$  below 70 K.  $S^M/T$  does not depend on the film thickness, while  $S^H$  decreases linearly with thickness. This could be an indication of a modified balance of electrons and holes when approaching the metal–insulator transition [84].

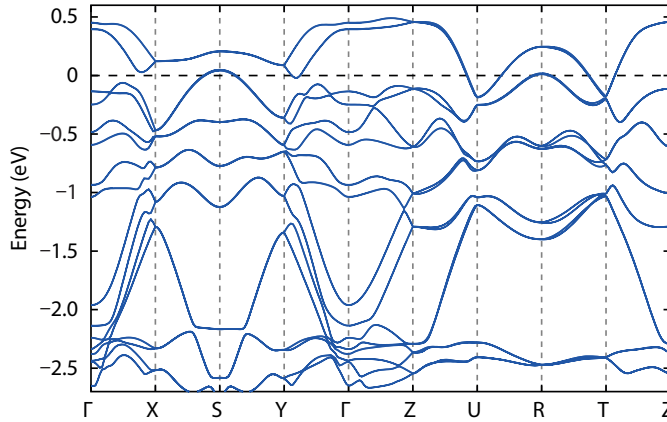


Figure 3.3: **Calculated electronic band structure of thick SIO.** The in-plane parameter was fixed to that of the STO substrate ( $a = 3.905 \text{ \AA}$ ) and the out-of-plane lattice parameter was fixed to  $c = 4.08 \text{ \AA}$ . A Coulomb repulsion of  $U = 0.80 \text{ eV}$  was used.

The analysis of the thermoelectric response requires the determination of the free parameters of Eq. (3.8) ( $\alpha, m_e^*, m_h^*$ ) on the basis of theoretical considerations. Here we use  $\alpha = 0.5$ , which is the typical choice when scattering is dominated by impurities or phonons [91]. To estimate the effective masses of the different bands, we calculate the electronic structure of SIO in the thick-film limit by means of first principles calculations. The in-plane lattice parameters were fixed to those of the STO substrate ( $3.905 \text{ \AA}$ ), and the out-of-plane lattice parameter was fixed to the experimental value for epitaxial SIO ( $4.08 \text{ \AA}$ ) [49]. Figure 3.3 shows the resulting band structure, where the density of

states near the Fermi level is dominated by the  $5d t_{2g}$  contribution as in orthorhombic bulk SIO. We calculate the effective masses of the holes at the maxima of the dispersion relations close to the Fermi level located at the  $S$  and  $R$  points and find an average value of  $m_h^* = 1.55 m_e$ . The band minima occur at the  $U$  and  $T$  points and along the  $Y$ - $\Gamma$  directions, and the corresponding average effective mass of the electrons is  $m_e^* = 0.34 m_e$ . These values are in agreement with the effective masses extracted from ARPES measurements on SIO/STO heterostructures [24].

### 3.3. MODELING OF ELECTRONIC TRANSPORT PARAMETERS

In the following, we evaluate  $n_{e,h}$  and  $\mu_{e,h}$  by using a direct sampling algorithm. Equations (3.2), (3.3), (3.7) and (3.8) are linearly independent and can therefore be combined to determine  $n_i$  and  $\mu_i$ . For each combination of  $(n_e, \mu_e)$ , the corresponding  $(n_h, \mu_h)$  pair is calculated by using the experimental values of  $\sigma_0$  and  $\rho_H$  in Eqs. (3.2) and (3.3). The resulting  $(n_i, \mu_i)$  set is accepted if the Hall effect (calculated with Eq. (3.1)) and the thermoelectric coefficients  $S^H$  and  $S^M/T$  (calculated with Eqs. (3.7) and (3.8)) agree with the experimental data (see Section 3.6.2 for further details).

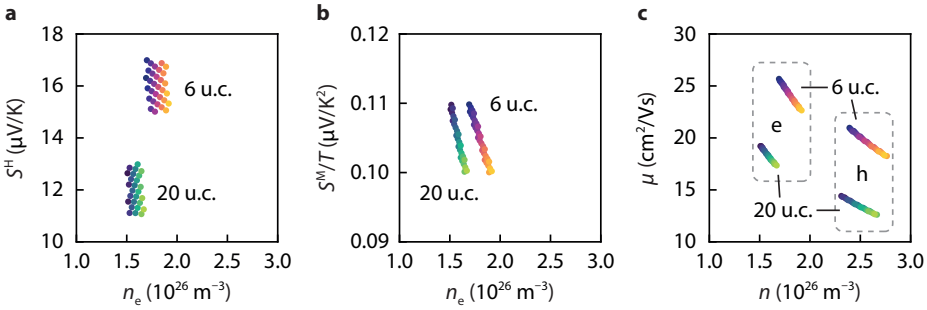


Figure 3.4: **Transport coefficients of 20 and 6 u.c. SIO films.** Seebeck coefficients from the formulas of Heikes (a) and Mott (b) of acceptable  $(n_i, \mu_i)$  combinations. Only electrons are shown for clarity. (c) Carrier densities and mobilities for electrons and holes satisfying the experimental constraints.

Table 3.1 shows the experimental values that are used as input parameters, where the  $\pm$  on the Seebeck coefficients indicates the range of the acceptance condition. Since the values of  $\rho_H$  and  $\sigma_0$  above show no thickness dependence above 15 u.c. [84], we combine electrical transport data of a 30 u.c. film with the Seebeck data of a 20 u.c. to perform the

$t$ (u.c.)	$\rho_H$ ( $\text{n}\Omega \text{ m/T}$ )	$\sigma_0$ ( $\text{S/m}$ )	$S^H$ ( $\mu\text{V/K}$ )	$S^M$ ( $\text{nV/K}^2$ )
30	-1.27	$1.0 \cdot 10^5$	$12 \pm 1$	$105 \pm 5$
6	-0.45	$1.5 \cdot 10^5$	$16 \pm 1$	$105 \pm 5$

Table 3.1: Input parameters of the sampling algorithm.

analysis. The calculated  $(n_i, \mu_i)$  combinations for the 20 and 6 u.c. films are presented in Figs. 3.4a and 3.4b, and the corresponding transport coefficients are shown in Fig. 3.4c. Each  $(n_i, \mu_i)$  set is a possible solution satisfying the the experimental constraints, and multiple sets are accepted because of the tolerances reported in Table 3.1. We find that the carrier densities and mobilities of the electrons and holes are located in two closely spaced groups of points on the  $(n, \mu)$  plane, with the electrons having higher mobility and lower density than the holes. Table 3.2 reports the centers of these groups together with the corresponding conductance of each channel.

3

$t$ (u.c.)	$n_e$ ( $10^{26}/\text{m}^3$ )	$n_h$ ( $10^{26}/\text{m}^3$ )	$\mu_e$ ( $\text{cm}^2/\text{Vs}$ )	$\mu_h$ ( $\text{cm}^2/\text{Vs}$ )	$\sigma_e$ (S/m)	$\sigma_h$ (S/m)
20	1.6	2.5	18	13.5	4.6	5.4
6	1.8	2.6	27	22	7.8	9.1

Table 3.2: Transport parameters extracted from the sampling algorithm under the experimental constraints.

The ratio between electron and hole carrier densities is approximately 1.7, confirming the marked multiband character of this system. The results of this analysis are consistent with the experimental observation of a hole-dominated electrical conductivity ( $\sigma_h > \sigma_e$ ), although this constraint was not explicitly introduced into the analysis. This is in agreement with both back-gate measurements (see Fig. 3.1) and the response to oxygen vacancies reported in Fig. 3.5. The calculated  $n_e$  values are two orders of magnitude lower than those obtained in a single band picture, showing that the measured Hall signals are determined by carrier compensation. The carrier density and mobility values do not depend strongly on temperature, since both  $\rho_H$  and  $\sigma_0$  show small temperature variations [84] and the Seebeck coefficients at low and high  $T$  are in good agreement with Eqs. (3.4) and (3.5). From the results of Table 3.2 we can calculate the cyclotron component of the magnetoresistance and compare it with the measured data. In Fig. 3.6 we show that our analysis is compatible with the experimental data in the framework of the present literature [92–99].

### 3.4. CONCLUSIONS

In conclusion, we investigated the electronic structure of SIO thin films by means of multiple transport techniques. The semimetallic nature of SIO manifests itself in a Hall effect dominated by electrons, and a hole-like electrical conductivity and Seebeck effect. The combination of magnetotransport and thermoelectric measurements with first-principles calculations allows us to obtain a set of possible transport coefficients of the charge carriers. Our results indicate that electrons and holes have similar densities and mobilities, yet the higher conductivity of the hole channel causes it to dominate electrical transport. This analysis constitutes a comprehensive and robust description of the electronic structure of SIO, paving the way for future studies on SIO-based heterostructures. Additionally, this approach can be extended to unravel the electronic structure of other semimetallic compounds.

## 3.5. METHODS

SIO thin films were grown by PLD on  $\text{TiO}_2$ -terminated STO(001) substrates and encapsulated *in-situ* with STO to prevent degradation during lithographic processing [49]. The growth conditions and structural properties are discussed in Ref. [49]. Magnetotransport measurements were acquired in a four-probe configuration in a flow cryostat with a base temperature of 1.5 K. Thermoelectric measurements were performed in a physical properties measurement system (PPMS) from Quantum Design equipped with thermal transport option in the continuous scanning mode with a 0.4 K/min cooling rate. First-principles density functional theory (DFT) calculations were performed within the generalized gradient approximation (GGA) by using the plane wave VASP [100] package and the PBEsol for the exchange-correlation functional [101] with SOC. The Hubbard  $U$  effects on the Ir sites were included within the GGA+ $U$  [102] approach using the rotational invariant scheme [103]. For  $U$  larger than 1 eV, the bulk phase is magnetic. To address non-magnetic Ir compounds [104], we used  $U = 0.80$  eV and  $J_H = 0.15U$ . The core and valence electrons were treated with the projector augmented wave method [105] and a cutoff of 400 eV for the plane wave basis was used. An  $8 \times 8 \times 6$   $k$ -point Monkhorst-Pack grid [106] was used for the calculation of the bulk phase.

## 3.6. SUPPLEMENTARY INFORMATION

### 3.6.1. INFLUENCE OF OXYGEN VACANCIES ON THE RESISTANCE

Oxygen vacancies ( $V_O$ ) are a ubiquitous doping mechanism for oxide materials and can often be reversibly induced by controlling the oxygen partial pressure and sample temperature.  $V_O$  act as electron donors, resulting in a higher or lower conductivity depending on whether electrons or holes dominate electrical transport. In order to verify that the electrical conductivity is dominated by holes, we study the influence of  $V_O$  on the resistance of an SIO thin film (Fig. 3.5). A film thickness of 3 u.c. was chosen to enhance the gas exchange owing to the high surface–volume ratio. Oxygen vacancies were created by increasing the sample temperature in a low-pressure environment. We measured the resistance in a four-probe geometry in a temperature- and pressure-controlled sample holder. The resistance was monitored as a function of temperature and oxygen partial pressure following the sequence illustrated in Fig. 3.5a, where the green curve was measured in  $10^{-3}$  mbar and the yellow curve in 1000 mbar. The labels  $t_1, \dots, t_5$  relate the evolution of the resistance in Fig. 3.5b with the sequence of  $T$  ramps illustrated in Fig. 3.5a. The ramp speed was 0.1 K/s. All the curves show semiconducting behavior, as expected for this film thickness. The absolute resistance value is affected by the oxygen pressure: at  $10^{-3}$  mbar ( $t_2$ ) the resistance increases, while at 1000 mbar ( $t_4$ ) it decreases. This is a signature of hole-dominated transport, which is in-line with the back-gate measurements in Fig. 3.1.

We note that the results of the back-gate measurements and  $V_O$  doping experiments could also be interpreted as originating from a change in the carrier scattering times. In this scenario, the variation of  $\sigma_0$  with  $V_{BG}$  could be related to the movement of the charge carriers towards defects at the SIO/STO interface, and the variations with  $V_O$  could be related to an increased concentration of defects. However, our interpretation of a change in carrier density as the source of the variations in  $R$  is fully consistent with the results

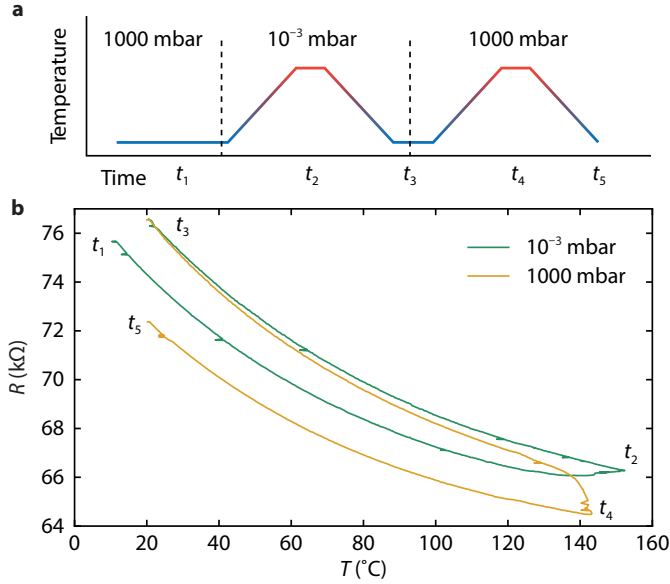


Figure 3.5: **Doping of a 3 u.c. SIO film by oxygen vacancies.** (a) Schematic representation of a sequence of temperature ramps between 20 $^{\circ}\text{C}$  and 150 $^{\circ}\text{C}$  under different pressure conditions. The ramp speed is 0.1 K/s. (b)  $R(T)$  curves with labels  $t_i$  corresponding to the times indicated in (a). At high temperature and low pressure,  $V_{\text{O}}$  are created and the electrical resistance increases.

of our magnetotransport/Seebeck analysis, which show that the electrical conductivity is dominated by holes. Furthermore, although both the capping layer and the substrate of STO could be affected by the formation of  $V_{\text{O}}$ , the observed response is not compatible with the doping of STO by oxygen vacancies, which would result in an increased conductivity.

### 3.6.2. SAMPLING ALGORITHM

The mapping is performed using logarithmic sampling on a grid of  $1000 \times 1000$  points. The initial boundaries are  $n_e \in [10^{20}, 10^{29}] \text{ m}^{-3}$  and  $\mu_e \in [10^{-1}, 10^3] \text{ cm}^2/\text{Vs}$ . These ranges are then narrowed down around the valid combinations (see below) in order to increase the sampling resolution. The  $(n_i, \mu_i)$  combinations compatible with the experimental data are calculated as follows:

1. Several  $(n_e, \mu_e)$  are taken in the probed domain and then the corresponding  $(n_h, \mu_h)$  are calculated by

$$n_h = \frac{(\sigma_0/e - n_e\mu_e)^2}{(\rho_H\sigma_0^2/e + n_e\mu_e^2)}, \quad \mu_h = \frac{(\rho_H\sigma_0^2/e + n_e\mu_e^2)}{(\sigma_0/e - n_e\mu_e)},$$

where  $\rho_H$  and  $\sigma_0$  are the experimental values. If the calculated  $n_h$  or  $\mu_h$  are negative, the initial  $(n_e, \mu_e)$  is discarded.

2. The Hall effect is calculated with its full expression and the low-field linear approximation:

$$\rho_{\text{H}}^{\text{full}} = \frac{1}{e} \frac{n_{\text{h}}\mu_{\text{h}}^2 - n_{\text{e}}\mu_{\text{e}}^2 + (n_{\text{h}} - n_{\text{e}})(\mu_{\text{h}}\mu_{\text{e}}B)^2}{\sigma_0^2/e^2 + (n_{\text{h}} - n_{\text{e}})^2(\mu_{\text{h}}\mu_{\text{e}}B)^2}, \quad \rho_{\text{H}}^{\text{lin}} = \frac{e}{\sigma_0^2} (n_{\text{h}}\mu_{\text{h}}^2 - n_{\text{e}}\mu_{\text{e}}^2).$$

The  $(n_i, \mu_i)$  set is accepted only if the difference between  $\rho_{\text{H}}^{\text{full}}$  and  $\rho_{\text{H}}^{\text{lin}}$  on the  $\pm 33$  T range is less than 5%, consistent with our experimental error in the measured magnetic field range. This condition is evaluated by checking every 2 T that the difference between  $\rho_{\text{H}}^{\text{full}}$  and  $\rho_{\text{H}}^{\text{lin}}$  does not exceed 5%.

3. The expected Seebeck coefficients corresponding to the  $(n_e, \mu_e)$  set are calculated using both the Mott and Heikes formulas and compared with the experimental values. If the results are within the acceptance ranges indicated in Table 3.1, the  $(n_i, \mu_i)$  set is accepted.

### 3.6.3. MAGNETORESISTANCE ANALYSIS

With the carrier density and mobility values we can calculate the cyclotron component of the MR, which for a multiband system is given by:

$$\text{MR} = \frac{1}{e} \frac{n_{\text{h}}\mu_{\text{h}} + n_{\text{e}}\mu_{\text{e}} + (n_{\text{h}}\mu_{\text{e}} + n_{\text{e}}\mu_{\text{h}})(\mu_{\text{e}}\mu_{\text{h}}B)^2}{\sigma_0^2/e^2 + (n_{\text{h}} - n_{\text{e}})^2(\mu_{\text{h}}\mu_{\text{e}}B)^2}. \quad (3.9)$$

The calculated MR for the  $(n_i, \mu_i)$  sets of Fig. 3.4 is shown in Fig. 3.6a. In order to compare this to the experimental data, we consider the measured MR of a 30 u.c. film, which has only a small contribution from quantum corrections due to its large thickness [84]. The magnitude of the calculated cyclotron component is small compared to the experimental MR measured at low  $T$  (Figs. 3.6b and 3.6c), which show a linear dependence on  $B$ . A better agreement between the calculated and experimental curves is found at temperatures between 20 K and 120 K, where the field-dependence is parabolic. At lower temperature, the cyclotron component becomes smaller than other sources of magnetoresistance. This interpretation is supported by the fact that, as discussed in the main text, the experimental parameters determining the transport coefficients are weakly dependent on temperature. Hence, as a consequence of Eq. (3.9), the cyclotron component of the MR is not expected to vary substantially as a function of temperature.

We now discuss possible origins of the linear MR of epitaxial SIO. Linear and non-saturating high-field MR has been observed in several semimetallic compounds and in bulk SIO [82], and can be attributed to different mechanisms. Although it can originate from Dirac cones in the band structure [82, 92, 96, 97], here this is unlikely because in SIO/STO the Dirac cones are gapped [24]. Other possible sources of linear MR are ferromagnetic order [95] and spatial inhomogeneities in the transport parameters [93, 94, 98]. Linear MR is also present in finite-size samples of nearly compensated semimetals due to the interplay between bulk and edge electron-hole recombination [99]. Considering previous reports of diverging magnetic susceptibility at low temperatures, the possible presence of point defects and the semimetallic nature of SIO thin films, several concurrent mechanisms are thus possible. Regardless of the specific source of the linear MR,

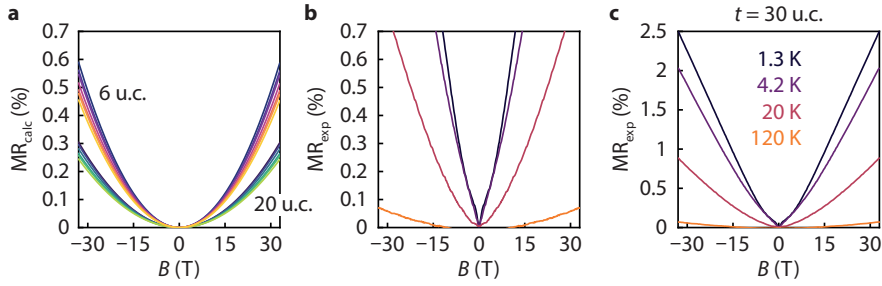


Figure 3.6: **Measured and calculated magnetoresistance.** (a) Semiclassical MR calculated from the  $(n_i, \mu_i)$  sets from Fig. 3.4b. (b) and (c) show the experimental MR of a 30 u.c. film as a function of temperature. The plots have a different y-axis scale to facilitate comparison with the calculated MR.

all contributions get weaker with increasing temperature, making the cyclotron component more visible. This is in agreement with Fig. 3.6b, where above 20 K the measured MR assumes values close to the simulated semiclassical response of Fig. 3.6a.

# 4

## SPIN-ORBIT SEMIMETAL SIO IN THE TWO-DIMENSIONAL LIMIT

*Sometimes science is more art than science.  
A lot of people don't get that.*

Rick, Rick & Morty

*The optimization procedures described in Chapter 2 enabled us to establish that SIO films retain their semimetallic behavior down to a thickness of 4 unit cells. In this chapter, we investigate the electronic properties of ultrathin SIO across the thickness-dependent metal-insulator transition. Low-temperature magnetoconductance measurements show that spin fluctuations in the semimetallic state are significantly enhanced while approaching the transition point. The electronic properties are further studied by scanning tunneling spectroscopy, showing that 4 u.c. SIO is on the verge of a gap opening. Our DFT calculations reproduce the critical thickness of the transition and show that the opening of a gap in ultrathin SIO requires antiferromagnetic order.*

---

Parts of this chapter have been published in Physical Review Letters **119**, 256403 (2017) by D. J. Groenendijk, C. Autieri, J. Girovsky, M. Carmen Martinez-Velarte, N. Manca, G. Mattoni, A. M. R. V. L. Monteiro, N. Gauquelin, J. Verbeeck, A. F. Otte, M. Gabay, S. Picozzi, and A. D. Caviglia [84].

STM measurements were performed by J. Girovsky, M. Carmen Martinez-Velarte, and A. F. Otte. N. Gauquelin and J. Verbeeck performed the HAADF-STEM measurements. Theoretical results were obtained by C. Autieri, M. Gabay, and S. Picozzi.

**T**HROUGH interface and strain engineering it is possible to tailor the delicate balance between competing energy scales and control the ground state of complex oxides [1, 107]. In the 2D limit, the coordination of constituent ions at the interfaces is reduced, typically yielding a decrease of the electronic bandwidth  $W$ . At a critical thickness depending on the relative magnitude of  $W$  and the Coulomb repulsion  $U$ , a metal-insulator transition can occur [108]. This approach has been applied to study the dimensionality-driven MIT in  $3d$  transition metal oxides such as  $\text{SrVO}_3$  and  $\text{LaNiO}_3$ , where a transition from a bulk-like correlated metallic phase to a Mott or static ordered insulating phase occurs in the 2D limit [107, 109–111].

In this chapter, we consider the  $5d$  oxide SIO which, in the three-dimensional limit, is a narrow-band semimetal bordering a Mott transition due to a combination of strong SOC and electronic correlations [23]. We find that an MIT occurs at a film thickness of 4 unit cells and study the evolution of the electronic structure across the transition by (magneto)transport and scanning tunneling spectroscopy (STS). The paramagnetic susceptibility is strongly enhanced while approaching the transition point, which is indicative of the opening of a Mott gap and the concomitant enhancement of magnetic order [112]. Our first-principles DFT calculations reproduce the critical thickness of the transition and show that the insulating state in the 2D limit is antiferromagnetically ordered. Our study highlights ultrathin SIO as a novel platform for engineering the interplay of magnetism and SOC at oxide interfaces.

SIO ( $n = \infty$ ) is the only (semi)metallic member of the RP series of strontium iridates  $\text{Sr}_{n+1}\text{Ir}_n\text{O}_{3n+1}$ . On the other end of the series, 2D  $\text{Sr}_2\text{IrO}_4$  ( $n = 1$ ) is a Mott insulator with canted antiferromagnetic order. Despite the extended  $5d$  orbitals, narrow, half-filled  $J_{\text{eff}} = 1/2$  bands emerge due to the strong SOC ( $\sim 0.4$  eV) and even a relatively small  $U \sim 0.5$  eV is sufficient to induce a spin-orbit Mott ground state [18, 50]. In SIO, the effective electronic correlations are smaller due to the three-dimensional corner-sharing octahedral network [20], but the strong SOC causes a significant reduction of the density of states (DOS) at the Fermi level. Together with octahedral rotations that reduce the crystal symmetry, this places the material at the border of a Mott transition and gives rise to an exotic semimetallic state [23, 88].

To study changes in electronic structure between the two end members of the RP series, previous studies have focused on varying the number of SIO layers in [(SIO) $_m$ , STO] superlattices [60, 113–116]. While these superlattices closely resemble the RP series, they are distinctly different from SIO thin films since they are affected by interlayer coupling. In particular, the superlattices are affected by additional hopping channels and magnetic coupling between SIO layers, which gives rise to a reduction of electronic correlations and the appearance of a net in-plane ferromagnetic moment [60, 114]. This was recently underlined by Hao et al. by demonstrating that the interlayer coupling can be tuned through the number of STO unit cells [115]. By studying single ultrathin SIO layers of different thickness, we directly address the effect of dimensionality and access the intrinsic properties of 2D SIO, which forms the building block for spin-orbit coupled superlattices and heterostructures.

## 4.1. CRITICAL THICKNESS OF THE MI TRANSITION

Figure 4.1a shows an optical image of a Hall bar used for transport measurements. A HAADF-STEM image of a 10 u.c. SIO film is shown in Fig. 4.1b, where atomically sharp interfaces with the substrate and the cap layer are visible. The sheet resistance  $R$  versus temperature  $T$  of SIO films with thicknesses  $t$  from 30 to 2 unit cells is shown in Fig. 4.1c. As the film thickness is reduced,  $R$  continuously increases and two different regimes can be identified. For  $t \geq 4$  u.c., the resistance values are below  $25 \text{ k}\Omega$  and the films show metallic behavior. Thinner films ( $t \leq 3$  u.c.) have a resistance above  $25 \text{ k}\Omega$  and display insulating behavior. Hence, it is apparent that SIO films undergo a semimetal–insulator transition between 4 and 3 u.c., occurring when the sheet resistance crosses  $h/e^2 = 25 \text{ k}\Omega$ . This is in good agreement with photoemission measurements, which show the disappearance of the Fermi cutoff below 4 u.c. and the opening of a charge gap [85]. In two dimensions, the resistance value  $h/e^2$  corresponds to the limit  $k_F l_e \sim 1$ , where  $k_F$  is the Fermi wavevector and  $l_e$  is the mean free path, marking the transition from weak to strong localization [117].

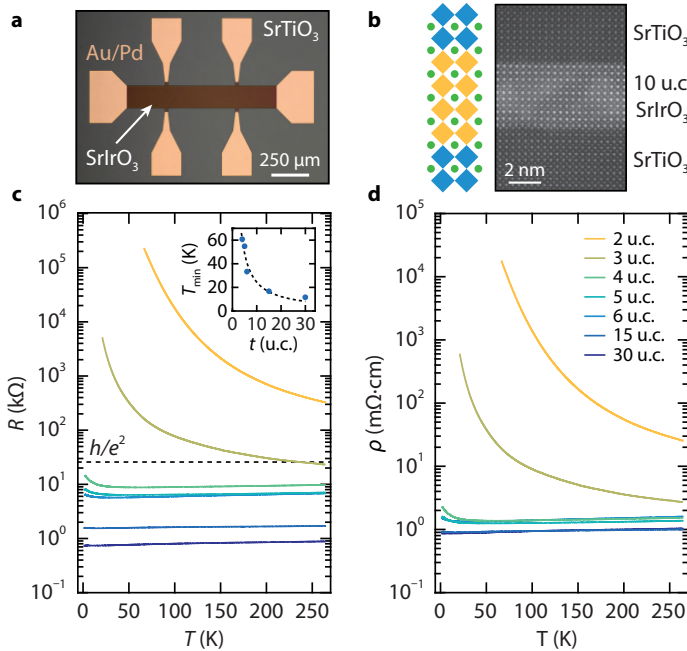


Figure 4.1: **Thickness-dependent MIT.** (a) Optical image of a Hall bar used for transport measurements. (b) HAADF-STEM image of a STO/10 u.c. SIO/STO heterostructure. (c)  $R(T)$  and (d)  $\rho(T)$  curves for films of different thicknesses. The inset shows the temperature of the resistance minimum ( $T_{\min}$ ) as a function of thickness. The dashed line is a guide to the eye.

In the (semi)metallic regime, the films show bad metallic behavior in the high temperature range, consistent with previous reports [49, 61, 62]. The resistance first decreases linearly with temperature until  $T_{\min}$ , below which an upturn occurs. In addition, the residual resistance ratio defined as  $R(300 \text{ K})/R(T_{\min})$  is rather low for all thick-

nesses ( $\sim 1.2$ ). Such anomalous metallic behavior is often observed in materials that are bordering a Mott transition. Upon decreasing the film thickness,  $T_{\min}$  increases from 10 K (30 u.c.) to 60 K (4 u.c.) (Fig. 4.1c, inset). In the semimetallic regime, the resistivity  $\rho$  curves collapse (Fig. 4.1d) and display similar behavior apart from the increasingly strong upturn at low temperature. Interestingly, the resistance upturn is accompanied by an increase of the Hall coefficient  $R_H$  (not shown here), which is likely related to the semimetallic electronic structure as underscored by ARPES measurements [23, 24]. Since the top energy of several hole bands was measured to lie just below the Fermi level, these bands will be progressively depopulated with decreasing temperature, increasing  $R_H$  and the resistance.

Transport in ultrathin films occurs in a strongly localized regime with a sheet resistance well in excess of  $h/e^2$ . For the 3 u.c. film, the conductivity  $\sigma$  can be well described by a variable range hopping (VRH) type of conduction (see Section 4.7.3). In this case, electrons hop between localized states and the conductance is given by  $\sigma = C \exp[-(T_0/T)^\alpha]$ , where  $T_0$  depends on the density of localized states and the spread of their wave functions [118]. VRH conductivity can be of either Mott or Efros-Shklovskii type, which for a 2D system translates into exponents  $\alpha = 1/3$  and  $1/2$ , respectively [119]. The fit to the data yields an exponent  $\alpha = 0.57$ , which is in good agreement with the latter, suggesting the existence of a Coulomb gap. On the other hand, the 2 u.c. film follows Arrhenius-type behavior where  $R \propto \exp(E_g/2k_B T)$ , which yields an energy gap  $E_g$  of approximately 95 meV.

## 4.2. MAGNETOCONDUCTANCE NEAR THE TRANSITION POINT

To probe changes in the electronic structure and spin relaxation while approaching the transition point, we perform magnetotransport measurements. Figure 4.2a shows the out-of-plane magnetoconductance  $\Delta\sigma$  in units of  $e^2/\pi h$  measured at 1.5 K for film thicknesses from 30 to 4 unit cells. In the limit of large thickness, the magnetoconductance is negative and quadratic and displays a cusp around  $B = 0$  T as reported in other works [61, 62]. However, a crossover from negative to positive values occurs as we approach the MIT. We attribute this behavior to weak (anti)localization, the interference of quantum coherent electronic waves undergoing diffusive motion (in the presence of SOC). To investigate this scenario, we fit the curves with the Maekawa-Fukuyama formula (red lines in Fig. 4.2b) in a diffusive regime that describes the change in the conductivity with magnetic field with negligible Zeeman splitting [120], where the extracted parameters  $B_\varphi$  and  $B_{s_0}$  are the effective fields related to the inelastic and spin-orbit relaxation lengths, respectively.

Since all the films have similar resistivity values, we fix  $B_e$  to 1.2 T, corresponding to an elastic length of approximately 11.7 nm and a carrier density in the order of  $10^{19} \text{ cm}^{-3}$ . This value yields the best fits over the entire thickness range (see Fig. 4.9) and is consistent with a Drude contribution. For the 30, 15, and 6 u.c. films, a  $B^2$  component was fitted at high fields and subtracted to account for the classical orbital magnetoconductance. The scattering lengths  $l_i$  are related to the effective fields by  $B_i = \hbar/4el_i^2$ , and their fitted values are shown in Fig. 4.2c. The extracted lengths show a crossover from  $l_\varphi > l_{s_0}$  for the thicker samples (30, 15 u.c.) to  $l_\varphi < l_{s_0}$  for the thinner ones (6, 5, 4 u.c.), cap-

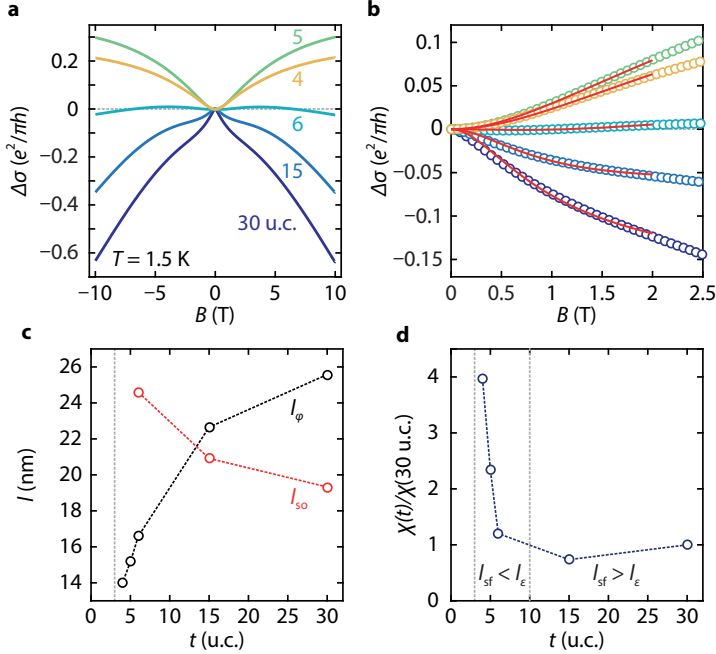


Figure 4.2: **Magnetotransport near the MIT.** (a) Magnetoconductance  $\Delta\sigma = \sigma(B) - \sigma(0)$  in units of  $e^2/\pi h$  measured in out-of-plane magnetic field for films of different thicknesses. (b)  $\Delta\sigma$  fitted by the Maekawa–Fukuyama formula (solid red lines). (c)  $l_{SO}$  and  $l_\phi$  extracted from the fits. (d) Relative susceptibility  $\chi(t)/\chi(30 \text{ u.c.})$  versus thickness.

turing the crossover from negative (weak antilocalization) to positive (weak localization) magnetoconductance as the film thickness is reduced.

A close look at the thickness dependence of  $l_\phi$  reveals deviations from the expected behavior considering only electron–electron corrections to the weak localization expression ( $1/l_\epsilon^2 \sim R \log k_F l_\epsilon$ , where  $l_\epsilon$  is the length associated with electron–electron corrections). To correctly describe the physics at play, one needs to include diffusive spin fluctuations which, when sufficiently large, can set the inelastic scattering length, leading to an effective inelastic scattering time given by  $1/\tau_\phi = 1/\tau_\epsilon + 2/3\tau_{sf}$ , where  $\tau_\phi$  is related to the energy relaxation time  $\tau_\epsilon$  and to the spin fluctuation time  $\tau_{sf}$  ( $l_i^2 = D\tau_i$ , where  $D$  is the diffusion constant) [121]. Since  $1/l_{sf}^2$  is proportional to the paramagnetic susceptibility  $\chi(t)$ , we can qualitatively track the variation of  $\chi$  by studying the thickness dependence of  $l_\phi$ . Figure 4.2d shows the relative susceptibility  $\chi(t)/\chi(30 \text{ u.c.})$  as function of thickness. The increase of  $\chi$  at low thicknesses is characteristic of a magnetic transition. We note that the transition from negative to positive magnetoconductance is set by the relative magnitude of  $l_\epsilon$  and  $l_{sf}$ . Near the transition point,  $l_{sf} < l_\epsilon$ , i.e., spin fluctuations are large, leading to a positive magnetoconductance due to weak localization. In the limit of large thickness,  $l_{sf} > l_\epsilon$ ,  $l_{SO}$ . Here, both electron–electron interactions and weak antilocalization contribute to the negative magnetoconductance. Structural studies have shown that octahedral coupling at the STO/SIO interface suppresses the bulk octahedral

rotations in the SIO film for  $t \leq 3$  u.c., enhancing magnetic interactions [85]. Within this view, the increase of  $\chi$  as the film thickness is reduced can be understood as an increased fractional contribution from the less distorted magnetic interfacial region.

### 4.3. SCANNING TUNNELING SPECTROSCOPY

Further insights on the anomalous behavior in the semimetallic state and the electronic structure near the MIT are obtained by measuring the local DOS across the Fermi energy  $E_F$  by STS measurements. A topographic scanning tunneling microscopy (STM) image (Fig. 4.3a, inset) acquired on a 10 u.c. SIO film shows terraces and steps with height equal to one unit cell, confirming the layer-by-layer growth mode and showing that the surface is single-terminated. Figure 4.3a shows differential conductance ( $dI/dV$ ) spectra acquired at 4 K on films of 4, 6 and 10 u.c. thickness. The spectra show V-shaped behavior with a linear dependence of the DOS for both occupied and unoccupied states. As shown in Fig. 4.3b, the minimum of the spectra is at zero energy (i.e., at  $E_F$ ) for all thicknesses, and while the spectra taken on the 6 and 10 u.c. films exhibit finite DOS, the 4 u.c. sample shows zero DOS at  $E_F$ . Therefore, the evolution of the DOS at  $E_F$  reflects the approach of the MIT, where the 4 u.c. film is on the verge of a gap opening.

4

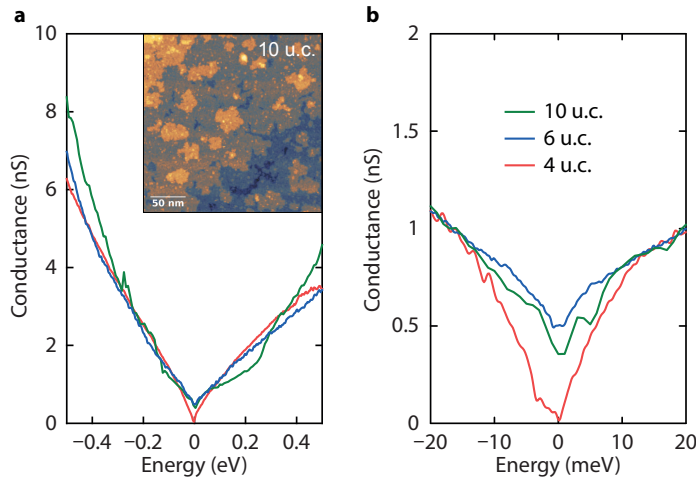


Figure 4.3: **STM near the MIT.** (a) Differential conductance ( $dI/dV$ ) spectra acquired on three different samples with film thicknesses of 4, 6 and 10 unit cells. Inset: STM topographic image of the surface of a 10 u.c. SIO film. (b)  $dI/dV$  spectra measured in a smaller energy range.

V-shaped differential conductance spectra have previously been observed in (i) systems with 2D Dirac surface states such as germanene/Pt(111) and graphene/SiC [122, 123] and (ii) in the pseudogap phase of doped Mott insulators such as cuprates [124, 125]. A Dirac cone is not expected in this system due to the breaking of  $n$ -glide symmetry by epitaxial constraint, as was shown previously for SIO on  $\text{GdScO}_3$  [26, 28]. However, in a recent work similar V-shaped behavior was found for  $\text{Sr}_2\text{IrO}_4$  doped with  $\text{La}^{3+}$ , showing zero DOS at  $E_F$  [126]. This observation was explained as being a result of charge carriers becoming untrapped for La concentrations exceeding 4%. The resemblance between the

two systems could stem from both SIO and doped  $\text{Sr}_2\text{IrO}_4$  being in close proximity to a metal-insulator transition, although on opposite sides of the phase boundary. However, further investigation is required to fully address the exact nature of the V-shaped DOS of SIO thin films.

#### 4.4. FIRST-PRINCIPLES CALCULATIONS

To study the electronic and magnetic structure of SIO in the 2D limit, we perform first-principles calculations. We first consider how the properties of bulk SIO evolve as a function of  $U$ . At low  $U$ , the system shows a nonmagnetic metallic state topologically protected by time-reversal symmetry [127]. Upon increasing  $U$ , a canted G-type antiferromagnetic metallic state with a net in-plane magnetic moment emerges [60]. A further increase of  $U$  opens a gap, leading to a G-type antiferromagnetic insulating state [25] like in  $[(\text{SIO})_m, \text{STO}]$  superlattices [60]. Since both  $U$  and the breaking of time-reversal symmetry are required to open the gap, insulating SIO is located in the intermediate region between a Slater- and a Mott-type insulator. The same qualitative results were obtained in other Ir compounds [128, 129].

When moving from bulk SIO to SIO/STO heterostructures, compressive strain, reduction of the bandwidth and an increase of  $U$  have to be taken into account. Compressive strain ( $\sim 1\%$ ) favors the metallicity [113] because of the increased bandwidth [104]. The other two effects favor the insulating state [130] and are needed to observe the semimetallic or insulating phase in SIO ultrathin films. We note that  $U$  is typically larger in thin films than in superlattices since the SIO layers are expected to exhibit a relaxation of octahedral tilts towards bulk values facilitated by tilts in the STO layers [131]. For our calculations, we focused on the thickness range in the vicinity of the MIT and computed the band structure of SIO layers (4 u.c. and 3 u.c.) on an STO substrate in the slab geometry (including vacuum) for  $U = 1.50$  eV. The results are shown together with the corresponding DOS in Figs. 4.4a and 4.4b, respectively.

The bandwidth reduction when going from 4 to 3 u.c. results in a localization of the carriers, and triggers a transition from a semimetallic to an antiferromagnetic insulating state. Even for a single layer of SIO on STO the nonmagnetic case is found to be metallic, and antiferromagnetic ordering is required for the opening of a gap [85]. The electronic structure of the 4 u.c. film shows a gap-closing behavior, consistent with STS. In the case of 3 u.c. the gap is 60 meV; its precise value is however crucially dependent on many effects such as octahedral distortions, magnetic order, strain, connectivity and Coulomb repulsion. Near the Fermi level, the DOS is dominated by  $5d$   $t_{2g}$  contribution as in bulk SIO. Hence, by reducing the thickness, we approach a state closer to  $J_{\text{eff}} = 1/2$  as in  $\text{Sr}_2\text{IrO}_4$ . However, while the  $t_{2g}$  unoccupied bandwidth is comparable to  $\text{Sr}_2\text{IrO}_4$ , the occupied part shows a mixed  $J_{\text{eff}} = 1/2, 3/2$  behavior rather than a pure  $J_{\text{eff}} = 1/2$  picture.

#### 4.5. CONCLUSIONS

In conclusion, we have shown that SIO can be driven into a correlated insulating state in the 2D limit. Quantum corrections to the conductivity indicate significant changes in scattering mechanisms in the semimetallic regime near the transition point. The diver-

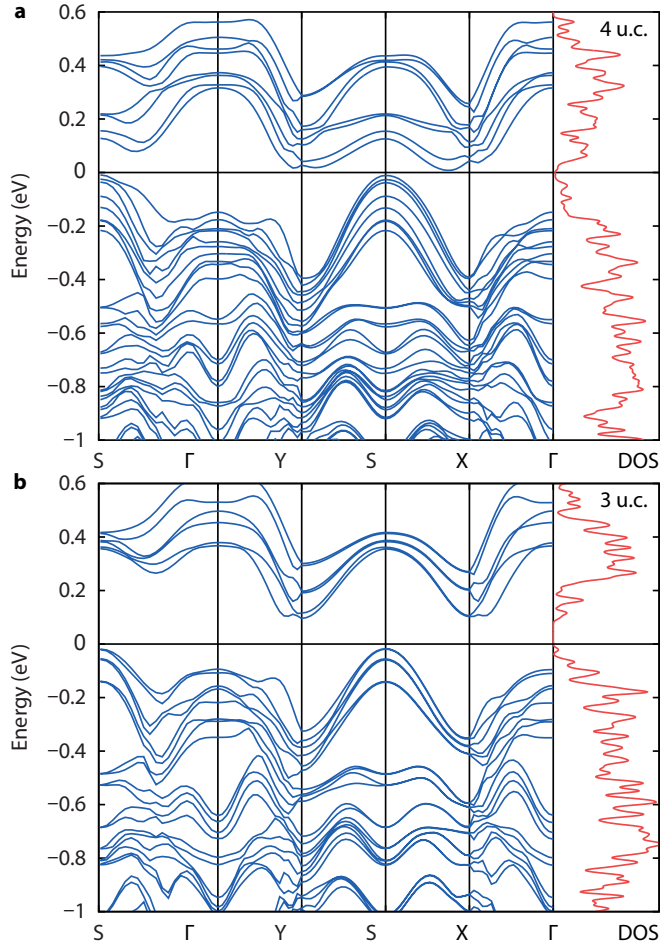


Figure 4.4: **Calculated band structures.** Calculated electronic structure for (a) 4 u.c. and (b) 3 u.c. SIO films on tetragonal STO with  $U = 1.50$  eV. Right: the corresponding DOS per formula unit as a function of energy.

gence of  $\chi$  is indicative of the opening of a Mott gap and the concomitant enhancement of magnetic order. The close proximity of SIO to a correlated insulating state is further corroborated by STS measurements, showing a V-shaped DOS similar to doped  $J_{\text{eff}} = 1/2$  Mott insulator  $\text{Sr}_2\text{IrO}_4$ . In addition, the 4 u.c. film reflects the onset of the gap opening as it shows zero DOS at the  $E_{\text{F}}$ , being at the border of the MIT. Our DFT calculations reproduce the metal-insulator transition for  $U = 1.50$  eV and show that antiferromagnetism develops concomitantly with the opening of a gap.

## 4.6. METHODS

A series of SIO films with thicknesses between 30 and 2 u.c. were grown by PLD on  $\text{TiO}_2$ -terminated STO(001) substrates. As described in previous work, we use an STO cap

layer to prevent film degradation in ambient conditions and enable lithographic processing [49]. Hall bars were patterned by e-beam lithography, and the SIO layer was contacted by Ar etching and in-situ deposition of Au/Pd, resulting in Ohmic contacts. Uncapped SIO films were transferred in an  $N_2$  atmosphere from the PLD chamber to the low-temperature STM setup. More details regarding the growth and sample characterization can be found in Section 4.7.1 and in Ref. [49]. First-principles DFT calculations were performed within the Generalized Gradient Approximation using the plane wave VASP [100] package and PBEsol for the exchange-correlation functional [101] with SOC. The Hubbard  $U$  effects on the Ir and Ti sites were included. To find a unique value of the Coulomb repulsion for the Ir  $5d$  states,  $U$  was tuned in order to reproduce the experimental semimetallic behavior at 4 u.c., while we used  $J_H = 0.15U$ . Using this approach we obtained  $U = 1.50$  eV, which is in good agreement with the typical values used for weakly correlated Ir compounds [104].

## 4.7. SUPPLEMENTARY INFORMATION

### 4.7.1. FILM GROWTH AND HALL BAR FABRICATION

Figure 4.5a shows the RHEED intensity evolution during the layer-by-layer growth of the SIO films and STO cap layers. The intensity variation of the diffraction spots during the SIO growth is rather large and the saturation of the signal is caused by the limited range of the detector. For the 30 and 15 u.c. films, the intensity is only shown for the first 1500 seconds. Figure 4.5b shows XRD measurements of SIO films grown on STO substrates with an amorphous STO cap layer (deposited at room temperature to prevent a diffraction signal from this layer). Clear Laue oscillations are observed for all films, confirming their epitaxial relationship and high quality. Figure 4.5c shows an optical image of a Hall bar before the lift-off of the resist mask used to protect the Hall bar during the Ar etching.

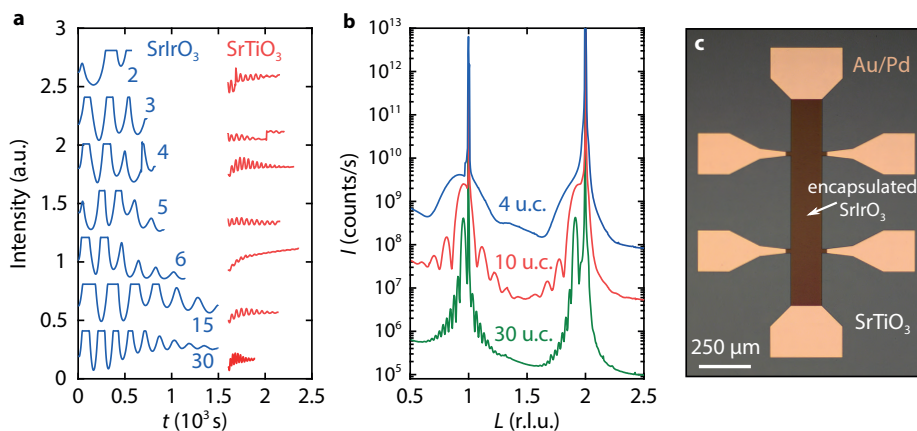


Figure 4.5: **Growth and characterization of SIO thin films.** (a) RHEED intensity evolution during the growth of SIO and STO films of different thicknesses on STO(001) substrates. The thickness of the SIO film is varied from 2 u.c. to 30 u.c. (top to bottom), while the thickness of the STO cap layer is 10 unit cells. (b)  $\theta$ - $2\theta$  scans of SIO films of different thicknesses with an amorphous STO cap layer. (c) Optical image of a Hall bar after the fabrication procedure.

### 4.7.2. INFLUENCE OF THE STO CAP LAYER

Figure 4.6 shows  $R(T)$  curves of SIO films with (Fig. 4.6a) and without (Fig. 4.6b) STO cap layer. The semimetal-to-insulator transition occurs between 6 and 5 u.c. for bare SIO films, while it occurs between 4 and 3 u.c. for encapsulated films. This difference is particularly evident if we consider the 6 u.c. film (Fig. 4.6c), where the temperature of the resistance minimum is 30 K and 256 K with and without STO cap layer, respectively. We attribute this to degradation of bare SIO films in ambient conditions as discussed in Ref. [49]. The properties of uncapped films could also be affected by an increase of octahedral tilts due to lack of “clamping” at the top surface. However, such an increase of out-of-plane octahedral tilts would lower the resistance, which is opposite to what is observed. This indicates that the difference between capped and uncapped films is mainly determined by film degradation of uncapped films in ambient conditions.

4

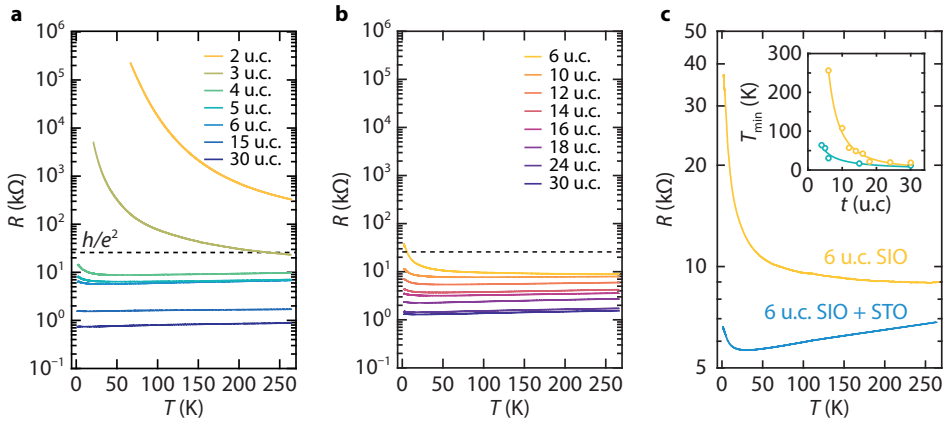


Figure 4.6: **Preservation of metallicity by STO encapsulation.** Resistance vs. temperature curves with (a) and without (b) STO cap layer. (c) Comparison of the  $R(T)$  curves of 6 u.c. SIO films with and without cap layer. The inset shows the temperature at which the upturn occurs ( $T_{\min}$ ) as a function of thickness.

### 4.7.3. TRANSPORT IN THE LOCALIZED REGIME

Figure 4.7a shows  $\ln \sigma$  vs.  $1/T$  of films with thicknesses of 3 and 2 u.c., i.e., in the localized regime. The curves are fitted by

$$\sigma = C \exp[-(T_0/T)^\alpha], \quad (4.1)$$

where  $T_0$  depends on the density of localized states and the spread of their wave functions [118]. Figures 4.7b and 4.7c show  $\ln \sigma$  vs.  $1/T^\alpha$  for the 3 and 2 u.c. films, respectively. For the 3 u.c. film, we find  $\alpha \approx 0.5$ , which indicates that Coulomb interactions play a dominant role [119]. For the 2 u.c. film, we find  $\alpha \approx 1$ , indicating that the temperature dependence of  $\sigma$  is well described by an Arrhenius-type behavior, which yields an energy gap  $E_g = 95$  meV. Hence, by decreasing the thickness from 3 to 2 u.c., the system transitions from hopping between localized states due to strong Coulomb interactions to a fully formed insulator with a well-developed gap.

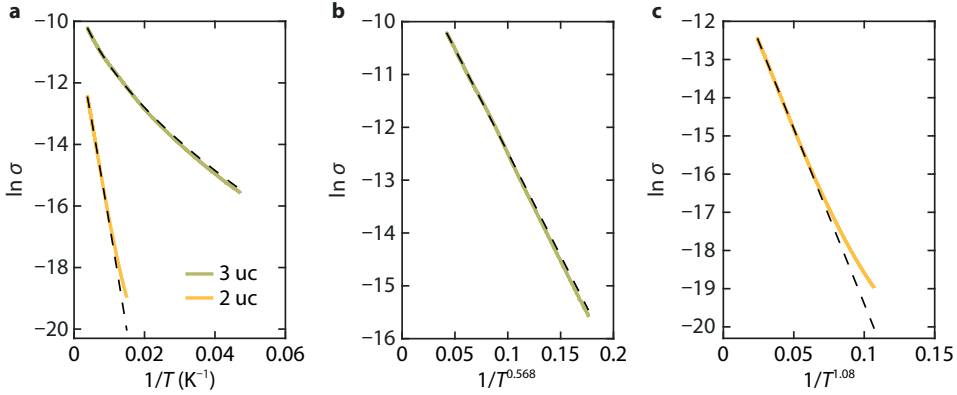


Figure 4.7: **Transport in the localized regime.** (a)  $\ln \sigma$  vs.  $1/T$  for the 3 and 2 u.c. films. The dashed lines are fits to Equation 4.1. (b) and (c) show  $\ln \sigma$  vs.  $1/T^\alpha$  for the 3 and 2 u.c. films, respectively.  $\alpha$  is the value extracted from the fit.

#### 4.7.4. MODELING OF MAGNETOTRANSPORT DATA

The magnetoconductance curves in Fig. 4.2b are fit with the Maekawa–Fukuyama formula in a diffusive regime that describes the change in the conductivity with magnetic field with negligible Zeeman splitting [120], given by

$$\begin{aligned} \frac{\Delta\sigma(B)}{\sigma_0} = & -\psi\left(\frac{1}{2} + \frac{B_e}{B}\right) + \frac{3}{2}\psi\left(\frac{1}{2} + \frac{B_\varphi + B_{\text{so}}}{B}\right) \\ & - \frac{1}{2}\psi\left(\frac{1}{2} + \frac{B_\varphi}{B}\right) - \ln\left(\frac{B_\varphi + B_{\text{so}}}{B_e}\right) \\ & - \frac{1}{2}\ln\left(\frac{B_\varphi + B_{\text{so}}}{B_\varphi}\right), \end{aligned} \quad (4.2)$$

where  $\psi$  is the digamma function,  $\sigma_0 = e^2/\pi h$  is the quantum of conductance and  $B_e$ ,  $B_\varphi$  and  $B_{\text{so}}$  are the effective fields related to the elastic, inelastic and spin–orbit relaxation lengths, respectively. The magnetoconductance comprises two contributions: a classical component that depends on the carrier densities and mobilities (see Eq. 3.9) but is typically proportional to  $B^2$ , and weak (anti)localization at low temperatures. Films with  $t \geq 6$  u.c. were found to display a significant classical component due to their relatively low resistance values. To highlight quantum corrections and accurately determine the scattering lengths, we subtracted the background prior to the fitting with the Maekawa–Fukuyama formula.

Figure 4.8a shows the data with  $cB^2$  fits at high fields (fitted for  $|B| \geq 7.5$  T, black dashed lines), and fits to the Maekawa–Fukuyama formula at low fields (green dashed lines), which saturate at high fields as expected. Their sum describes the behavior at low magnetic fields well (red dashed lines). Figure 4.8b shows the quadratic component for different film thicknesses. The prefactor  $c$  is given by  $c = A_K \sigma_0 / G_0$ , where  $A_K$  is the

Kohler coefficient and  $G_0 = e^2/\pi h$ . The fits yield  $A_K = 0.44 \cdot 10^{-4} \text{ T}^{-2}$ ,  $0.68 \cdot 10^{-4} \text{ T}^{-2}$  and  $0.36 \cdot 10^{-4} \text{ T}^{-2}$  for the 30, 15 and 6 u.c. films, respectively. The values are similar, indicating that the mobility is not strongly thickness-dependent in this regime.

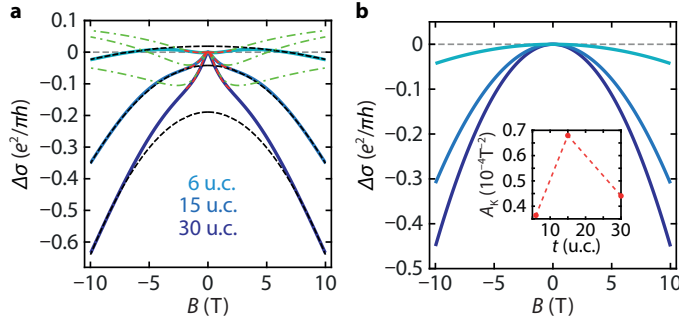


Figure 4.8: **Subtraction of the classical MR component.** (a) Magnetoconductance  $\sigma(B)$  measured for different thicknesses. Black lines:  $B^2$  component fitted at high fields; green lines: fits to the Maekawa–Fukuyama equation; red lines: sum of the two fits. (b) Fitted quadratic component for different film thicknesses. Inset: the Kohler coefficient  $A_K$ , extracted from the quadratic fit by  $c = A_K\sigma_0/G_0$ .

Since all films in the semimetallic regime have similar resistivity values, we set the characteristic field for elastic scattering ( $B_e$ ) to a fixed value during the fitting with the Maekawa–Fukuyama formula.  $B_e$  is related to the elastic length through  $B_e = \hbar/4el_e^2$ , where  $l_e$  is given by  $l_e = \hbar\sigma(3\pi^2n)^{1/3}/ne^2$ , where  $n$  is the carrier density. Due to the semimetallic nature of SIO and the linearity of the Hall effect, it is not possible to straightforwardly determine the carrier density. A single-band model for the electrons would yield a carrier density in the order of  $10^{28} \text{ m}^{-3}$  and an elastic length smaller than the interatomic spacing. Therefore, we fitted the  $\Delta\sigma$  curves for different values of  $l_e$  ( $B_e$ ), of which two are shown in Fig. 4.9. The best fits were obtained for  $B_e = 1.2 \text{ T}$ , corresponding to  $l_e = 11.7 \text{ nm}$  and a carrier density in the order of  $10^{25} \text{ m}^{-3}$ . The extension of the Maekawa–Fukuyama formula to higher fields in Figs. 4.9b and 4.9e shows that the fits saturate correctly for the 1.2 T case. Importantly, the behavior of  $l_\varphi$  and  $l_{so}$  were found to be only weakly dependent on the chosen value of the elastic length.

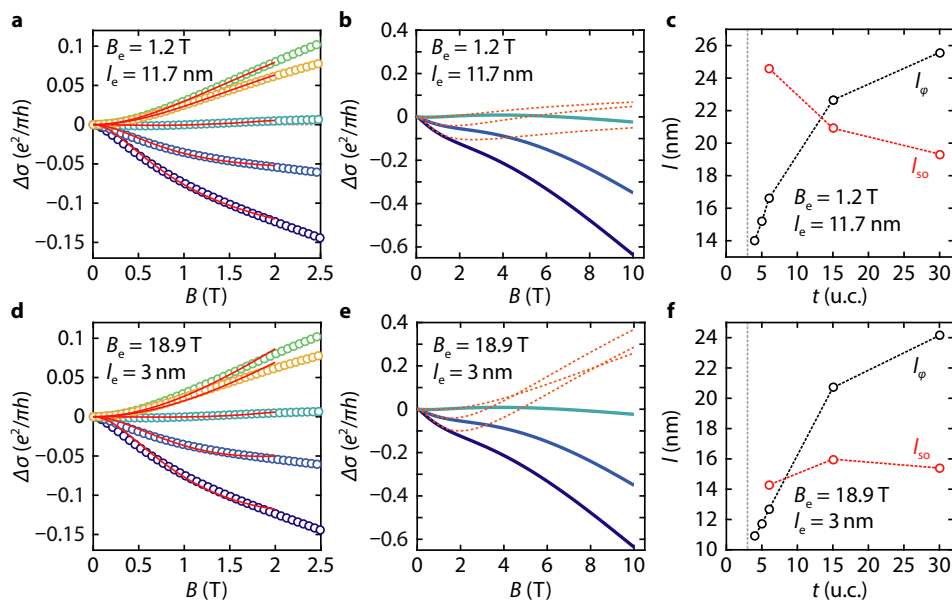


Figure 4.9: **Fitting of magnetoconductance for different values of the elastic length.** (a) and (d) show  $\Delta\sigma$  fitted by the Maekawa-Fukuyama formula including the  $B^2$  background (solid red lines). (b) and (e) show the behavior of the Maekawa-Fukuyama formula at higher fields (without  $B^2$  component). (c) and (f) show the extracted  $l_\varphi$  and  $l_{so}$  as a function of thickness.



# 5

## ANISOTROPIC MAGNETORESISTANCE IN TWO-DIMENSIONAL SIO

*SIO, the three-dimensional member of the Ruddlesden-Popper iridates, is a paramagnetic semimetal due to the delicate interplay between SOC and Coulomb repulsion. In this chapter, we study the anisotropic magnetoresistance (AMR) of SIO thin films, which is closely linked to SOC and probes correlations between electronic transport, magnetic order and orbital states. We show that the low-temperature negative MR is anisotropic with respect to the magnetic field orientation, and its angular dependence reveals the appearance of a fourfold symmetric component above a critical magnetic field. We show that this AMR component is of magnetocrystalline origin, and attribute the observed transition to a field-induced magnetic state in SIO.*

---

Parts of this chapter are being prepared for submission (2019), by D. J. Groenendijk, N. Manca, J. de Bruijkere, L. M. K. Tang, A. M. R. V. L. Monteiro, R. Gaudenzi, A. McCollam, H. S. J. van der Zant, and A. D. Caviglia.

J. de Bruijkere and R. Gaudenzi assisted with the anisotropic magnetoresistance measurements. L. M. K. Tang and A. McCollam assisted with the high-field measurements at the High Field Magnet Laboratory in Nijmegen.

**T**RANSITION metal oxides with  $5d$  elements feature a rare interplay between Coulomb repulsion  $U$ , crystal-field  $\Delta$  and strong SOC that gives rise to novel electronic and magnetic states [132, 133]. A significant body of work has been devoted to the RP series of strontium iridates ( $\text{Sr}_{n+1}\text{Ir}_n\text{O}_{3n+1}$ ) following the discovery of a  $J_{\text{eff}} = 1/2$  Mott state in  $\text{Sr}_2\text{IrO}_4$  [18, 50]. The dimensionality of these compounds can be tuned by varying  $n$ , which increases octahedral connectivity and lowers  $U$  [20]. The resulting bandwidths have been studied through optical spectroscopy, showing an increase from 0.48 eV ( $n = 1$ ,  $\text{Sr}_2\text{IrO}_4$ ) to 1.01 eV ( $n = \infty$ , SIO), where in the 3D limit a semimetallic state is found [19]. Photoemission and transport studies have shown that the unusual electronic structure of SIO consists of heavy hole-like and light electron-like bands [23, 24, 74]. First-principles calculations and diffraction measurements show that these electron-like bands originate from Dirac cones that are gapped due to symmetry breaking in response to strain [28]. This is always the case for epitaxial films, and strain-free SIO can only be studied in polycrystalline form since the single-crystal perovskite phase is thermodynamically unstable [57]. Both polycrystalline samples [82, 134] and thin films [62, 65, 84, 135, 136] have been studied through MR measurements. While the MR in strain-free SIO is 2–3 orders of magnitude larger than in epitaxially strained films, it is qualitatively similar, showing positive, quasilinear behavior.

The proximity of SIO to a metal–insulator phase boundary gives rise to anomalous properties such as non-Fermi liquid behavior and enhanced paramagnetism due to an instability of ferromagnetic ordering [112, 137]. Signatures of non-Fermi liquid behavior such as linear resistivity versus temperature [49] and divergent specific heat [27] have previously been observed. In ultrathin films,  $U$  is further increased by confinement, resulting in an enhancement of spin fluctuations [84]. This brings the system closer to two-dimensional  $\text{Sr}_2\text{IrO}_4$ , in which the magnetic moments display canted in-plane antiferromagnetic order [22, 138]. The magnetic state of  $\text{Sr}_2\text{IrO}_4$  was studied through anisotropic MR (AMR) measurements, which revealed a field-induced metamagnetic transition from an antiferromagnetic to a weakly ferromagnetic state [139–141]. Here, we use AMR measurements to study the correlation between electronic transport and magnetic order in ultrathin SIO. We find that the low-temperature negative MR component is anisotropic, and its angular dependence reveals the appearance of a fourfold symmetric component above a critical magnetic field. We attribute this to field-induced magnetic ordering in the SIO film that is inherently close to a ferromagnetic instability. Since AMR is closely associated with SOC, its study in SIO can complement the understanding of its role in determining the ground state of  $5d$  oxides.

## 5.1. LOW-TEMPERATURE MAGNETOTRANSPORT

Resistivity ( $\rho$ ) versus temperature ( $T$ ) characteristics of three SIO films of different thicknesses are shown in Fig. 5.1a. The films show metallic behavior with an upturn at low temperature similar to previous reports [49, 62, 65, 84]. The out-of-plane MR of the 6 u.c. film measured at  $T = 4$  K and 540 mK is shown in Fig. 5.1b. The MR is quasilinear down to 4 K and increases in magnitude with decreasing temperature. Its magnitude is approximately 2 orders of magnitude smaller than in polycrystalline samples, where it was attributed to a topological transition of a Dirac node and enhanced paramagnetism [82].

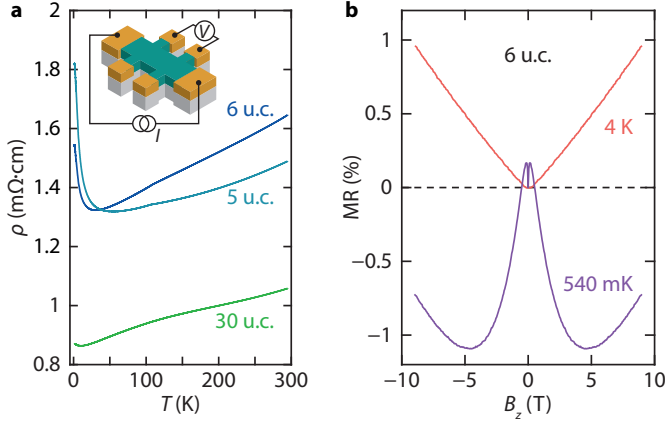


Figure 5.1: **Magnetotransport characterization.** (a) Resistivity versus temperature of SIO films of different thicknesses grown on STO. (b) Out-of-plane MR of a 6 u.c. SIO film measured at two different temperatures.

At low temperature, a negative MR component appears. For the 6 u.c. film, this is below 2 K, however this value depends sensitively on the film thickness. MR measurements on the 5 and 30 u.c. films are shown in Fig. 5.6. In previous work, we showed that this behavior is governed by a crossover from weak antilocalization to weak localization as the film thickness is reduced [84].

## 5.2. ANGULAR DEPENDENCE OF MAGNETORESISTANCE

We further study the MR of the 6 u.c. film by varying the angle between the magnetic field ( $B$ ) and the film normal. Figure 5.2a shows the MR at  $T = 4$  K (top) and 540 mK (bottom) for  $B$  applied along  $z$  and  $y$  (see the inset or Fig. 5.2c for their definition). At 4 K, the two are positive, linear and of equal magnitude, while the negative MR measured at 540 mK shows a pronounced anisotropy. In particular, the magnitude of the negative MR is larger when  $B$  is parallel to the film normal. The angular dependence is shown in Fig. 5.2b, where  $B$  is rotated with fixed magnitude in the  $xy$ -plane (top) and in the  $yz$ -plane (bottom). Interestingly, 4 peaks are observed at 540 mK, while there is no measurable anisotropy at 4 K. Additionally, the MR in the  $yz$ -plane displays two peaks of larger magnitude, while the peaks heights are equal in the  $xy$ -plane.

AMR consists of a non-crystalline and a crystalline component, which have very different microscopic origins. The non-crystalline component depends on the angle between the magnetization ( $M$ ) and current ( $I$ ), reflecting the difference between transport scattering matrix elements of electrons with momentum parallel to the current in the  $I \parallel M$  and  $I \perp M$  configurations. The crystalline component, instead, originates from the changes in the equilibrium relativistic electronic structure induced by the rotating magnetization and is thus related to SOC. It manifests itself as a difference between scattering matrix elements for the electrons with momentum parallel and perpendicular to  $M$ . Owing to the anisotropy of the electronic structure with respect to the magnetization angle, these matrix elements may change when  $M$  is rotated [140].

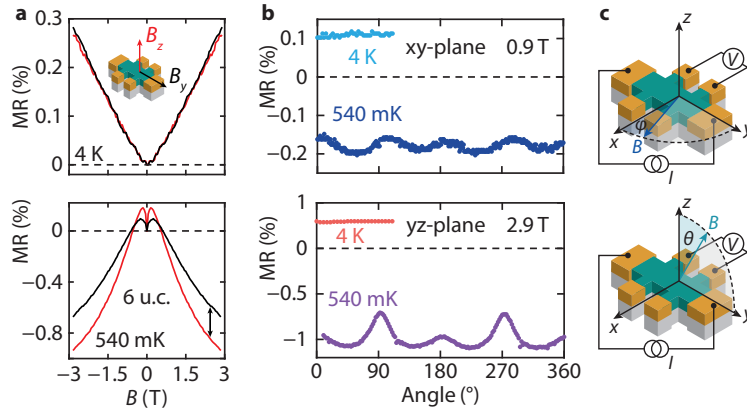


Figure 5.2: **Angular dependence of the MR.** (a) MR of a 6 u.c. SIO film measured at 4 K (top) and 540 mK (bottom) for magnetic fields applied along  $z$  (out-of-plane) and along  $y$  (in-plane,  $B \parallel I$ ). (b) Angular dependence of the MR in the  $xy$ -plane (top) and the  $yz$ -plane (bottom) at 4 K and 540 mK. (c) Schematics of the measurement configuration.

5

The two contributions to the AMR can be identified by measuring the magnitude of the MR while rotating  $B$  across the different planes defined by our sample geometry (illustrated in Fig. 5.2c). In a rotating magnetic field,  $M$  follows  $B$  if  $|B|$  is larger than the coercive field. This implies that the angle  $\theta$  between  $M$  and the electrical current  $I$  may vary, which, for non-crystalline AMR, results in a signal proportional to  $\sin^2(\theta)$ . If the magnetic field rotates along in the plane perpendicular to the current ( $xz$ -plane), the angle between  $M$  and  $I$  remains constant and the AMR is determined by the varying angle between magnetization and crystal axes. In this way, the crystalline component of the AMR can be isolated.

### 5.3. ANISOTROPIC MAGNETORESISTANCE IN DIFFERENT PLANES

Figure 5.3 shows the angular dependence of the MR measured while rotating  $B$  in the  $xy$ -,  $yz$ -, and  $xz$ -planes. The measurements are performed at the base temperature of the system ( $T = 75$  mK). At this temperature, we use a Wheatstone bridge circuit to accurately measure the change in resistance ( $\Delta R$ ) due to the large resistance and its small variation with magnetic field. At  $B = 0.15$  T [Fig. 5.3a (top)], the symmetry of the AMR is twofold, and the magnitude of  $\Delta R$  is nearly equal when rotating the field in the  $xz$ - and  $yz$ -planes. The difference (and the small signal in the  $xy$ -plane) is likely due to a slight misalignment in angle. This indicates that this component [proportional to  $\sin^2(\phi)$ ] does not depend on the angle between  $I$  and  $M$ , as it varies in the  $yz$ -plane whereas it is always  $90^\circ$  in the  $xz$ -plane. Instead, this component depends on the relative angle between  $B$  and the film normal. It cannot be attributed to classical MR, as this would provide a positive contribution to the MR when  $B$  is perpendicular to the plane. Therefore, this MR most likely originates from the anisotropy of quantum corrections, as the negative MR associated with weak localization is largest when  $B$  is along  $z$ .

At higher fields ( $B = 1$  T, bottom panel),  $\Delta R$  increases significantly and 4 peaks of

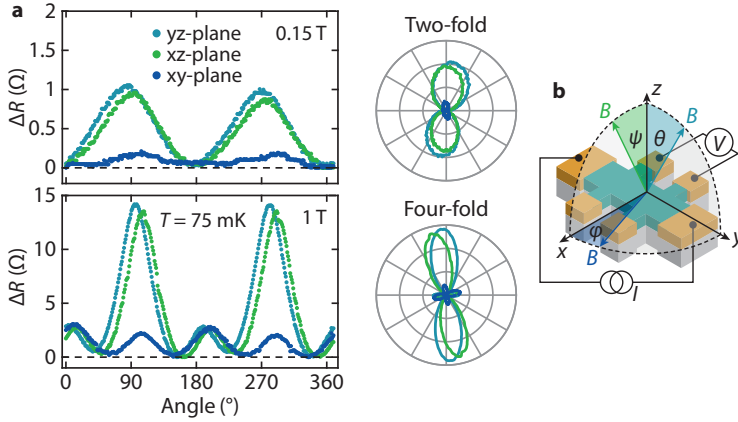


Figure 5.3: **AMR in different planes.** (a) Angular dependence of the MR in the  $xy$ -,  $xz$ - and  $yz$ -planes measured at 75 mK with an applied field of 0.15 T (top) and 1 T (bottom). On the right, polar plots of the MR are shown.  $\Delta R$  is defined as the relative resistance measured during the angular sweep. (b) Schematic of the measurement configuration.

equal magnitude appear in the  $xy$ -plane. In the  $xz$ - and  $yz$ -planes, the peaks at  $90^\circ$  and  $270^\circ$  increase in magnitude and additional peaks appear at  $0^\circ$  and  $180^\circ$ . The polar plots (right) confirm that the MR in the  $xy$ -plane is fourfold symmetric, while it shows two large and two small lobes in the  $xz$  and  $yz$ -planes. The magnitude of the fourfold symmetric component [proportional to  $\cos^2(2\phi)$ ] is equal in all planes: this component is thus solely affected by the relative orientation of  $B$  and the crystal axes. We note that this AMR component cannot be measured in polycrystalline samples as the contributions from different crystalline domains average out. The sign and symmetry of this component is not compatible with classical MR or weak (anti)localization. The negative MR is largest when the field is oriented at  $45^\circ$  with respect to the tetragonal unit cell. Since crystalline AMR requires a net magnetization that rotates with respect to the crystal axes, we attribute this to field-induced magnetic ordering in the SIO film. This is consistent with reports of a divergent magnetic susceptibility at low temperatures [27] and signatures of a magnetic transition below 2 K in polycrystalline samples [82].

## 5.4. FIELD-INDUCED MAGNETIC TRANSITION

To determine the field at which the crystalline AMR appears, we measure the angular dependence of the MR for different magnitudes of  $B$  as shown in Fig. 5.4. The magnitude of the AMR gradually increases, and the field at which the additional peaks appear can be determined by tracking  $\Delta R$  at  $\theta$  and  $\phi = 0$  and  $90^\circ$ . The bottom panel shows that this occurs at approximately 0.2–0.3 T. A field-induced magnetic transition in SIO has previously been inferred from specific heat measurements in monoclinically distorted SIO [27]. There, it was suggested that a quantum critical point (QCP) between a non-Fermi liquid and field-induced ferromagnetic state is located at  $T = 0$  K and  $\mu_0 H = 0.23$  T. This value corresponds well to the magnetic field at which the fourfold symmetric AMR appears.

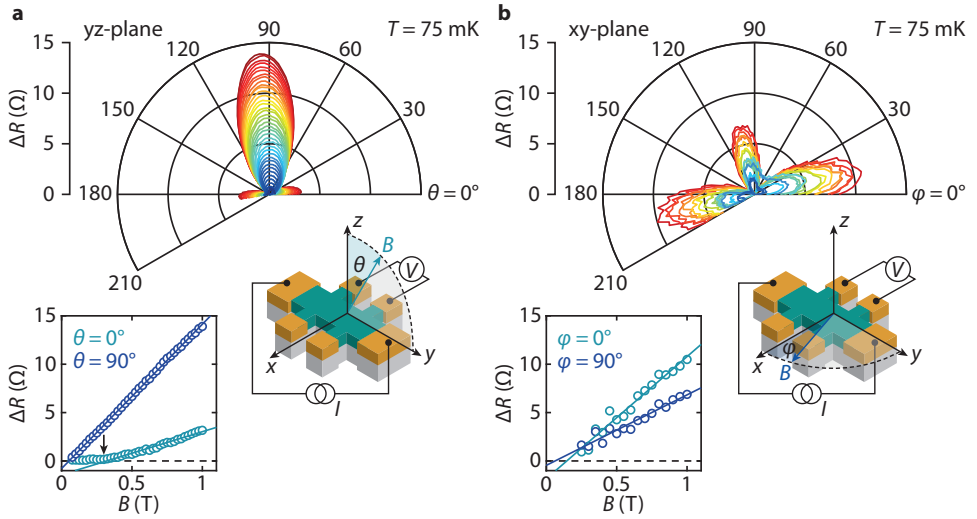


Figure 5.4: **Determination of the critical field of the crystalline MR.** (a) Polar plot of the MR in the  $yz$ -plane measured at 75 mK. The bottom panel shows the relative resistance change along  $z$  ( $\theta = 0^\circ$ ) and  $y$  ( $\theta = 90^\circ$ ). (b) Polar plot of the MR in the  $xy$ -plane. The bottom panel shows the MR along  $x$  ( $\phi = 0^\circ$ ) and  $y$  ( $\phi = 90^\circ$ ).

Finally, we compare the measured AMR of SIO to that of  $\text{Sr}_2\text{IrO}_4$ , which is on the other side of the metal-insulator phase boundary. In  $\text{Sr}_2\text{IrO}_4$ , the canting of  $J_{\text{eff}} = 1/2$  moments leads to an uncompensated moment within each of the  $\text{IrO}_2$  planes, and these moments can be aligned by an external magnetic field, leading to a weakly ferromagnetic state [139–141]. The magnetic moments are coupled to the octahedral-site rotations by strong SOC, and the measured AMR originates from lattice distortions induced by magnetoelastic coupling. In SIO, such a strong single ion anisotropy is not present. Instead, the net magnetization likely originates from the enhanced paramagnetic state. The fourfold symmetry of the AMR is therefore intimately related to the crystal structure, band structure, and orbital symmetry of  $5d$  electrons with strong SOC.

## 5.5. CONCLUSIONS

In conclusion, we showed that the low-temperature, negative MR component in SIO thin films is anisotropic with respect to the magnetic field orientation. The twofold symmetric component, present only when the angle between  $B$  and the film normal is varied, is attributed to the anisotropy of weak (anti)localization. A fourfold symmetric component appears as  $B$  is increased, and the critical field corresponds well to the QCP previously reported by Cao et al. [27]. We attribute this to crystalline AMR originating from a field-induced magnetic state in ultrathin SIO. Our study underlines the connection between SOC, magnetization and orbital character in strontium iridates. The discovery of a field-induced magnetic state has important implications for interfaces with SIO, where interfacial magnetism, easy-axis reorientation and topological Hall effect have been observed [43, 142, 143].

## 5.6. METHODS

SIO films were grown by PLD on  $\text{TiO}_2$ -terminated STO(001) substrates. Hall bars were patterned through Ar etching and *in-situ* evaporation of Pd/Au contacts. RHEED oscillations show that both SIO and STO grow in layer-by-layer mode. XRD and HAADF-STEM measurements show that the films are in a tetragonal state due to the suppression of octahedral tilts by the STO substrate. Magnetotransport measurements were performed in a dilution fridge with a base temperature of 70 mK equipped with a vector magnet and low-noise electronics. The resistance was measured in four-probe configuration with lock-in amplifiers. A Wheatstone bridge circuit was used to measure small resistance variations.

## 5.7. SUPPLEMENTARY INFORMATION

### 5.7.1. GROWTH OF SIO/STO HETEROSTRUCTURES

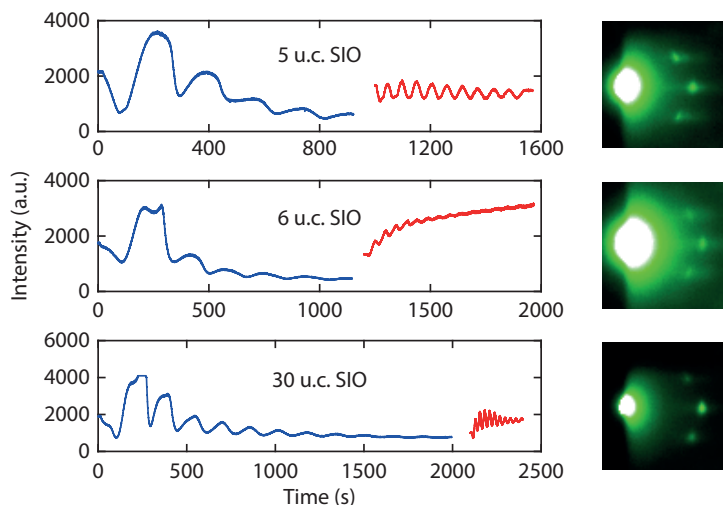


Figure 5.5: **Growth of SIO/STO heterostructures.** From top to bottom: RHEED oscillations during the growth of 5, 6, and 30 u.c. SIO films, followed by 10 u.c. STO. For the 30 u.c. film, only 12 oscillations are shown. Right: RHEED diffraction pattern after the growth of SIO.

Figure 5.5 shows the RHEED intensity during the growth of 5, 6, and 30 u.c. SIO films on  $\text{TiO}_2$ -terminated STO(001) substrates. The growth of SIO is followed by the growth of a 10 u.c. STO cap layer to enable patterning of Hall bars and prevent degradation of the SIO [49]. The clear intensity oscillations indicate that both the SIO and STO grow in layer-by-layer mode.

### 5.7.2. MAGNETORESISTANCE OF 5 AND 30 U.C. FILMS

Figure 5.6 shows high-field MR measurements of a 30 and a 5 u.c. SIO film. The magnitude of the MR of the 30 u.c. film increases with decreasing temperature (Fig. 5.6a) and

reaches approximately 2.5% at 33 T. Below 4.2 K, the MR displays a cusp at low fields which can be attributed to quantum corrections.

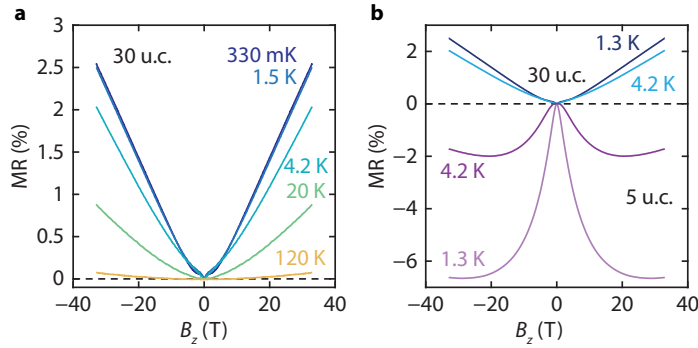


Figure 5.6: **Temperature evolution of the MR of 30 and 5 u.c. SIO films.** (a) High-field MR of a 30 u.c. SIO film measured at different temperatures. (b) High-field MR of a 30 and 5 u.c. SIO film measured at 4.2 K and 1.3 K.

Figure 5.6b shows the MR of the 30 and 5 u.c. SIO films measured at 4.2 K and 1.3 K. The 5 u.c. film displays a large negative MR which can be attributed to weak localization. Figure 5.7a shows the MR of the 30 and 5 u.c. films measured at 1.3 K for  $B$  oriented parallel (red) and perpendicular (black) to the film normal.

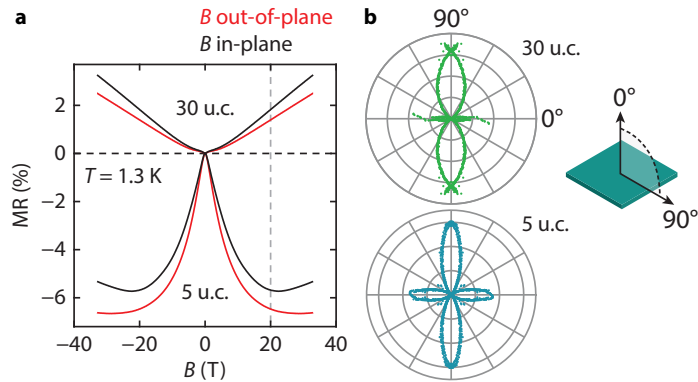


Figure 5.7: **Angular dependence of the high-field MR.** (a) High-field MR of the 30 and 5 u.c. SIO films for  $B \parallel n$  (red) and  $B \perp n$  (black), where  $n$  is the film normal. (b) Polar plots of the MR measured at  $B = 20$  T. To the right, a schematic of the two orientations is shown.

For both films, the negative MR is larger when  $B$  is oriented along the film normal. To study the anisotropy in more detail, the MR is measured as a function of angle with an applied magnetic field of 20 T. The polar plots in Fig. 5.7b show two large and two small lobes, similar to the measurements on the 6 u.c. film shown in Fig. 5.2b (bottom) and Fig. 5.3b (bottom). We attribute the large suppression at  $\phi = 90^\circ$  and  $\phi = 270^\circ$  to the anisotropy of weak (anti)localization. The other two lobes at  $\phi = 0^\circ$  and  $\phi = 180^\circ$  arise

from the fourfold symmetric signal, which we attributed to magnetocrystalline AMR. This indicates that films of different thicknesses also develop a field-induced magnetization at low temperatures. The magnitude of the AMR appears to increase as the film thickness is reduced, however its precise evolution should be further investigated.



# 6

## BERRY PHASE ENGINEERING IN STO/SRO/SIO HETEROSTRUCTURES

*Deep in the human unconscious is a pervasive need for a logical universe that makes sense. But the real universe is always one step beyond logic.*

Frank Herbert, Dune

*Having established the electronic and magnetic properties of SIO in the ultrathin limit (Chapters 4 and 5), we investigate how it affects the properties of a complex oxide ferromagnet by forming atomically sharp interfaces. In particular, we demonstrate how electronic transport in ultrathin SRO can be manipulated by imposing asymmetric boundary conditions in the form of two dissimilar interfaces with STO and SIO. Measurements of the anomalous Hall effect (AHE) reveal the presence of two interface-tunable spin-polarized conduction channels. Using theoretical calculations, we show that the tunability of the AHE at SRO interfaces arises from the competition between two topologically nontrivial bands. Our results demonstrate how reconstructions at oxide interfaces can be used to control emergent electrodynamics on a nanometer-scale, opening new routes towards spintronics and topological electronics.*

---

Parts of this chapter appeared online in preprint ([arXiv:1810.05619](https://arxiv.org/abs/1810.05619)) and are submitted for peer review (2018) by D. J. Groenendijk, C. Autieri, T. C. van Thiel, W. Brzezicki, N. Gauquelin, P. Barone, K. H. W. van den Bos, S. van Aert, J. Verbeeck, A. Filippetti, S. Picozzi, M. Cuoco, and A. D. Caviglia [144].

HAADF-STEM measurements were performed by N. Gauquelin, K. H. W. van den Bos, S. van Aert, and J. Verbeeck. Theoretical results were obtained by C. Autieri, W. Brzezicki, P. Barone, S. Picozzi, and M. Cuoco.

**I**N topologically nontrivial band structures, electrons acquire an additional phase factor when their wavefunctions traverse a closed loop in momentum space [35]. Although this concept is now commonly referred to as the Berry phase mechanism, Karplus and Luttinger already demonstrated decades earlier that the anomalous Hall effect—which is prevalent in itinerant ferromagnets—finds its origins in band topology [41]. In addition to the usual band dispersion contribution, electrons in an electric field  $\mathcal{E}$  acquire an anomalous velocity:

$$v(k) = \frac{1}{\hbar} \frac{\partial E(k)}{\partial k} - \frac{e}{\hbar} \mathcal{E} \times b(k), \quad (6.1)$$

where  $E(k)$  is the dispersion relation and  $b(k)$  is the Berry curvature. The latter describes the nontrivial geometry of the band structure and acts as an effective magnetic flux [38]. The anomalous velocity is transverse to the electric field and gives rise to a Hall current, with a sign and magnitude that depend sensitively on the band structure topology. In systems with ferromagnetic order and sizable SOC, the Berry curvature is strongly enhanced near avoided band crossings which act as a source or sink of the emergent magnetic field [145]. A prototypical system is the transition metal oxide SRO, a 4*d* itinerant ferromagnet exhibiting an AHE that is well reproduced by first-principles calculations [34]. Its anomalous Hall conductivity depends sensitively on the position of the Fermi level with respect to the avoided band crossings and on the magnetization [34, 38, 146, 147], forming an ideal platform to be tuned through symmetry breaking at interfaces. A suitable material for this purpose is SIO, a 5*d* paramagnetic semimetal with strong atomic SOC ( $\sim 0.4$  eV) [19, 23] and excellent structural compatibility with SRO. In this chapter, we investigate the AHE in ultrathin SRO films with (a)symmetric boundary conditions. We show that transport at SRO/SIO and SRO/STO interfaces occurs through topologically nontrivial bands with opposite Berry curvature. Remarkably, in the tricolor STO/SRO/SIO system the two spin-polarized conduction channels are found to be coexisting.

## 6.1. ANOMALOUS HALL EFFECT OF ULTRATHIN SRO

We first analyse theoretically the properties of ultrathin SRO starting from the Ru-based  $t_{2g}$  electronic structure close to the Fermi level. Our ab-initio derived tight binding calculations show that the Berry curvature of the individual bands is strongly enhanced at avoided band crossings due to next-nearest-neighbor interorbital hopping (Fig. 6.1a) in the presence of SOC. We first focus on the monolayer SRO system. Its electronic structure can be arranged in two groups of 3 bands with different spin-orbital parity. Within each sector, there are two topologically nontrivial bands carrying a Chern number  $C = \pm 2$ , accompanied by a single, trivial band with  $C = 0$ , (see Fig. 6.1b). The ensuing Berry curvature of the nontrivial bands, which have predominantly  $d_{xz}$  and  $d_{yz}$  character, is shown in Fig. 6.1c. We find sharp peaks located at the avoided bands crossings. Since the lowest energy bands in Fig. 6.1b have a nontrivial Chern number, the Berry curvature contribution of each band cannot vanish and is robust to changes in the Fermi level or, in general, of the corresponding electron occupation. Their splitting and relative occupation leads to a dominance of one of the channels, including sign changes when considering the averaged Berry curvature. A complete compensation is improbable and can only acci-

dentally occur by electronic fine tuning. SOC influences the character of the avoided crossings and causes the bands with opposite Berry curvature and  $d_{xz/yz}$  orbital character to have a distinct momentum dependence of the spin polarization, with an opposite sign developing nearby the points of maximal Berry curvature accumulation, as shown in Fig. 6.1d.

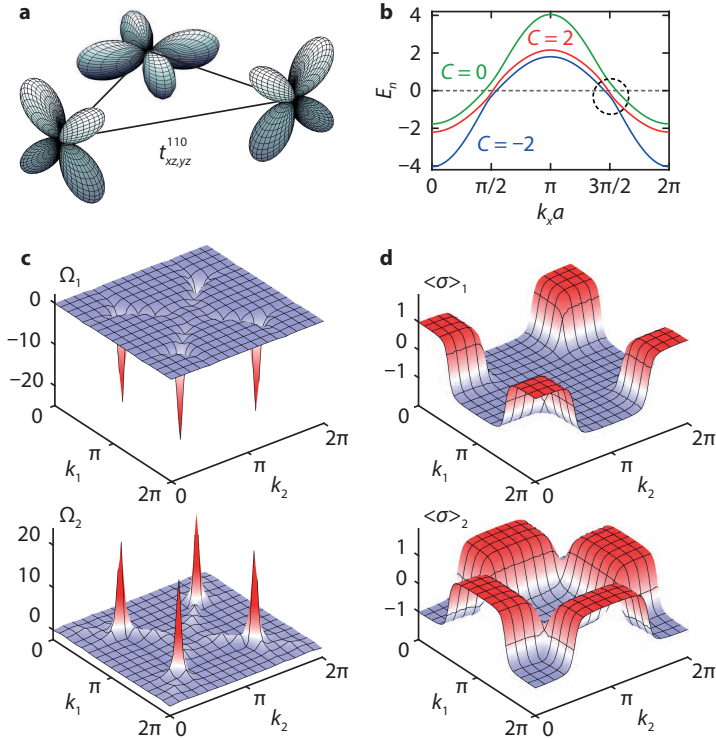


Figure 6.1: **Electronic structure and Berry curvature of monolayer SRO.** (a) Next-nearest-neighbor inter-orbital hopping. (b) Dispersion of Ru  $t_{2g}$  bands along  $k_x = k_y$  for a representative value of the magnetization. (c) Berry curvature associated with topologically nontrivial Ru  $t_{2g}$  bands close to the Fermi level (Chern numbers  $\mathcal{C} = \pm 2$ ).

We now investigate the AHE of SRO films with symmetric boundary conditions, shown in Figs. 6.2a and 6.2b. We consider heterostructures composed of STO/2 u.c. SIO/4 u.c. SRO/2 u.c. SIO/10 u.c. STO and STO/4 u.c. SRO/10 u.c. STO. Strikingly, we find that the sign of the AHE is opposite for SIO/SRO/SIO (Fig. 6.2a) and STO/SRO/STO (Fig. 6.2b) heterostructures. This immediately shows that symmetry breaking in ultrathin SRO directly controls the magnitude and sign of its Berry curvature. The magnitude ( $R_{xy}^{AH}$ ) as a function of temperature is shown in Fig. 6.2c. While  $R_{xy}^{AH}$  of the STO/SRO/STO is mainly negative and changes sign as near the Curie temperature ( $T_C$ ),  $R_{xy}^{AH}$  of the SIO/SRO/SIO remains positive in the entire temperature range. This confirms the expectation that the occupation of the topologically active Ru  $t_{2g}$  bands depends sensitively on the electronic

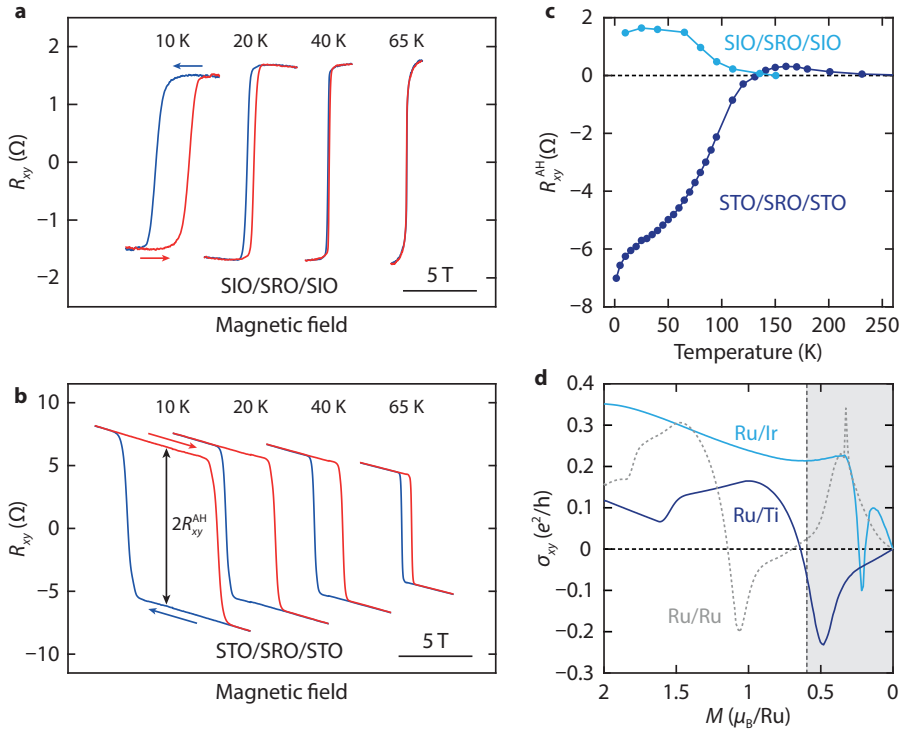


Figure 6.2: **Anomalous Hall effect of ultrathin SRO with symmetric boundary conditions.** Hall resistance of symmetric SIO/SRO/SIO (a) and STO/SRO/STO (b) heterostructures as function of temperature. The curves are offset horizontally. (c) Temperature evolution of the amplitude of the AHE ( $R_{xy}^{\text{AH}}$ ). (d) Evolution of the intrinsic contribution to  $\sigma_{xy}$  for Ru/Ti, Ru/Ir and Ru/Ru bilayers as a function of the average Ru magnetization. The dashed black line indicates the approximate saturated magnetization value of the STO/SRO/SIO determined from SQUID measurements.

matching at the interface. This behavior can be qualitatively captured by modeling Ru/Ti and Ru/Ir bilayers, i.e., systems with a  $\text{RuO}_2$  monolayer coupled a  $\text{TiO}_2$  or  $\text{IrO}_2$  monolayer. As shown in Fig. 6.2d, for small/intermediate amplitude of the Ru magnetization the AH conductivity is negative for the Ru/Ti bilayer while it is positive for the Ru/Ir bilayer. In the former, only the Ru  $d_{xz/yz}$  contribute since the STO is electronically inert, while for the latter, the intrinsic Berry curvature sign competition of the Ru topological bands is modified through the hybridization of the Ir/Ru  $d_{xz/yz}$  orbitals, and interfacial magnetic canting/reconstructions.

To study the effect of asymmetric boundary conditions, we now investigate the tri-color STO/SRO/SIO system (Fig. 6.3). Given the different trends observed in the symmetric systems, we expect competition in the total  $R_{xy}^{\text{AH}}$  in this case. The atomic arrangement at the interfaces is investigated by HAADF-STEM imaging (Fig. 6.3b). Chemical analysis by electron energy loss spectroscopy (EELS) shows that the interfaces are atomically sharp and that the thicknesses of both the SRO and SIO layers are 4 u.c. as designed (see

Fig. 6.9). After quantifying atomic column positions in the HAADF-STEM image using StatSTEM [148], a detailed analysis of the atomic positions shows that octahedral tilts are suppressed and both the SRO and SIO are tetragonal rather than orthorhombic as in their bulk form. In addition, we find that the tetragonality ( $c/a$ ) of the unit cell varies strongly across the SRO and SIO layers (Fig. 6.3a). Since the magnetic anisotropy of SRO is known to be very sensitive to strain and tetragonality [149–151], this affects the easy axis direction of the different SRO layers and hence the local magnetization of the Ru ions. This is confirmed by SQUID measurements, included in Fig. 6.8, which show that the STO/SRO/SIO has a larger in-plane magnetization than STO/SRO/STO. This indicates that the magnetization of the SRO layers near the SIO interface is canted, which is consistent with the reduction of  $c/a$  close to the SIO interface.

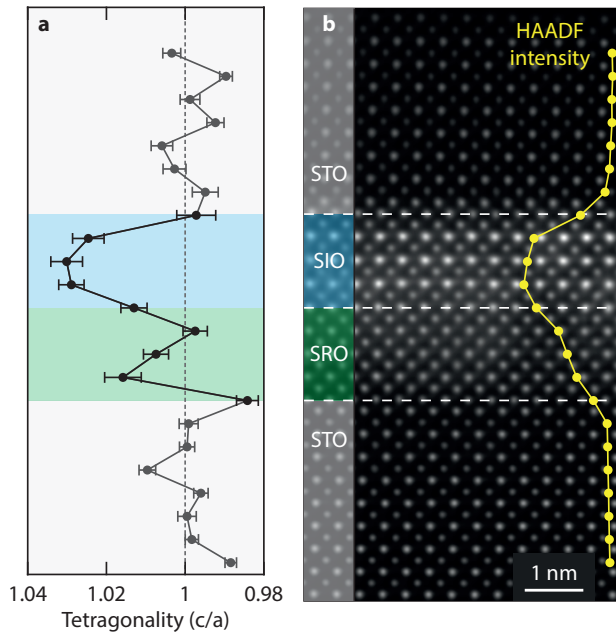


Figure 6.3: **Structural characterization of STO/SRO/SIO by HAADF-STEM.** (a) Tetragonality of the perovskite unit cell across the heterostructure. (b) HAADF-STEM measurement of an STO/SRO/SIO heterostructure.

The AHE of the STO/SRO/SIO is shown in Fig. 6.4a. With increasing temperature, the AHE changes sign at the reversal temperature  $T_R = 48$  K and peaks appear to be superimposed on the Hall effect, slightly above and below the coercive field ( $B_c$ ). This is in stark contrast with the AHE of an STO/SRO/STO heterostructure (Fig. 6.4b), where the magnitude decreases with increasing temperature. The sign reversal is not related to a change in carrier type, as the ordinary Hall component remains electron-like and its slope is approximately constant (see Fig. 6.11c). The peaks superimposed on the Hall effect are present between 35 and 58 K and reach their maximum amplitude at  $T_R$ , i.e., when  $R_{xy}^{AH}$  appears to be zero. This strongly suggests that their occurrence is intrinsically linked to the sign reversal of the AHE. In the following, we will show that the AHE can be modeled

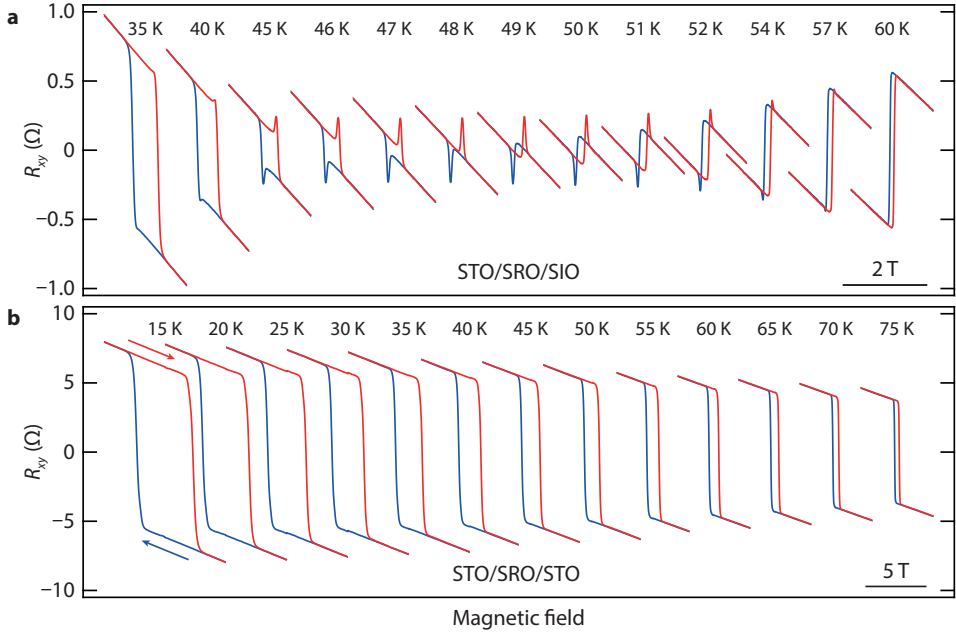


Figure 6.4: **Anomalous Hall effect of ultrathin SRO heterostructures with asymmetric boundary conditions.** Measured Hall resistance of (a) an asymmetric STO/SRO/SIO heterostructure and (b) a symmetric STO/SRO/STO heterostructure at different temperatures. The curves are offset horizontally.

by the superposition of two anomalous Hall channels with opposite sign and different  $B_c$ .  $R_{xy}^{AH}$  of each channel is determined by the balance between topologically nontrivial  $\mathcal{C} = 2$  and  $\mathcal{C} = -2$  bands, which is modified by the STO and SIO interfaces. This gives rise to two conduction channels with a different  $R_{xy}^{AH}(T)$  dependence. Within this picture,  $T_R$  of the two channels no longer coincide, resulting in a temperature window in which  $R_{xy}^{AH}$  of the two channels is of opposite sign. We are able to resolve these two channels due to their different  $B_c$ , governed by the interfacial modification of the magnetic anisotropy. We note that it is not possible to assign an exact spatial profile to the two channels due to strong out-of-plane orbital hybridization and the two-dimensional character of the film.

## 6.2. PRESENCE OF TWO ANOMALOUS HALL CHANNELS

To illustrate the total AHE in this case, we consider a heterostructure with two independent anomalous Hall channels (labeled I and II) with  $R_{xy}^{AH}$  of opposite sign and  $B_{c,II} < B_{c,I}$ . This situation is sketched in Fig. 6.5a for three cases:  $|R_{xy,II}^{AH}| < |R_{xy,I}^{AH}|$  (left),  $|R_{xy,II}^{AH}| = |R_{xy,I}^{AH}|$  (middle), and  $|R_{xy,II}^{AH}| > |R_{xy,I}^{AH}|$  (right). When a current  $I$  is applied in the plane of the heterostructure and the magnetic field is varied in the range  $[0, B, -B, 0]$ , the total AHE is given by the sum of the AHE of the two layers. Depending on their relative magnitudes, three different behaviors can be discerned for  $B_{c,II} < B_{c,I}$ . This concept was first introduced in 1981 [152] and forms the basis for a device called the extraordinary Hall

balance [153, 154].

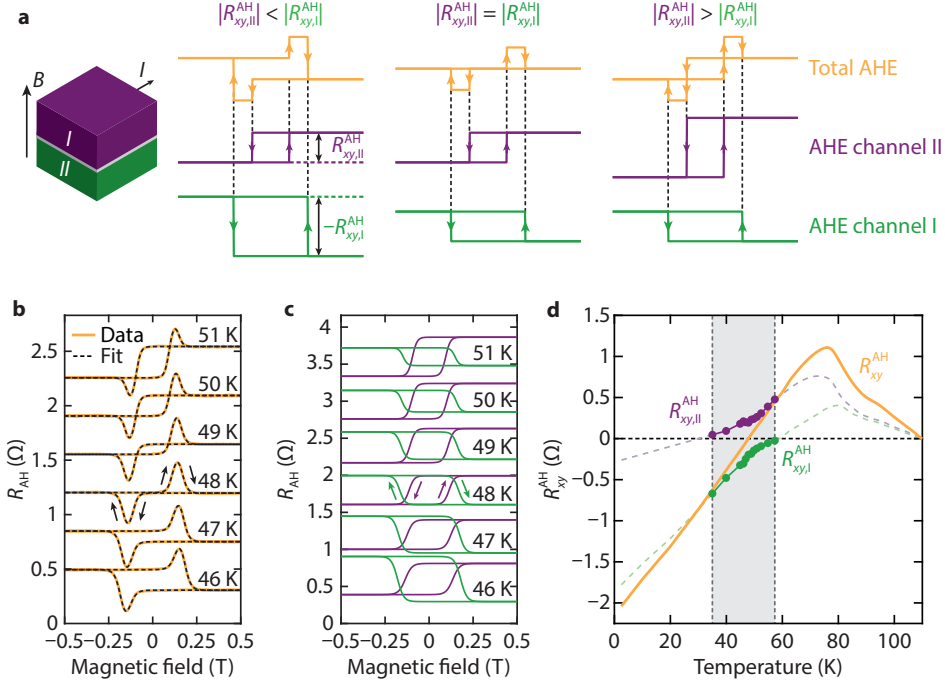


Figure 6.5: **Presence of two anomalous Hall channels.** (a) Addition of the AHE for two decoupled ferromagnetic layers with opposite sign of  $R_{xy}^{AH}$ . (b)  $R_{AH}$  as function of temperature. The black dashed lines are fits to the data and the curves are offset vertically. (c) The two anomalous Hall components that add up to the total  $R_{AH}$  curves in (b). (d) Total  $R_{xy}^{AH}$  and the extracted  $R_{xy}^{AH}$  from the two anomalous Hall components. The dashed lines illustrate a possible temperature dependence of  $R_{xy}^{AH}$ .

The measured AHE of the STO/SRO/SIO in Fig. 6.4a. bears striking resemblance to the curves in Fig. 6.5a. The ordinary Hall component has been subtracted and the remaining anomalous Hall component ( $R_{AH}$ ) is presented in Fig. 6.5b. As the temperature is increased from 46K towards 51K, the behavior of the total AHE evolves from the leftmost scenario in Fig. 6.5a to the rightmost scenario, with the middle scenario emerging at  $T_R = 48$ K. This is consistent with two anomalous Hall contributions of opposite sign, each with a slightly different temperature dependence. We investigate this further by considering a phenomenological model of the anomalous Hall data with  $R_{AH} = R_{xy,I}^{AH} \tanh(\omega_I(B - B_{c,I})) + R_{xy,II}^{AH} \tanh(\omega_{II}(B - B_{c,II}))$ , where  $\omega$  is a parameter describing the slope at  $B_c$ . An excellent agreement is obtained between this model (dashed black lines in Fig. 6.5b) and the data, enabling us to extract the individual AH components as a function of temperature (Fig. 6.5c). The corresponding  $R_{xy}^{AH}$  values are shown in Fig. 6.5d; both components show a smooth evolution in temperature, with one disappearing above 58 K (green) and the other below 35 K (purple). At 48K the two components are equal, leading to the fully compensated case.

In Fig. 6.5d we illustrate a possible dependence of  $R_{xy}^{\text{AH}}(T)$  (dashed lines) at higher and lower temperatures, which suggests that  $R_{xy}^{\text{AH}}$  and  $B_c$  of the two channels follow a qualitatively similar temperature dependence, shifted by 23 K. This implies that, for  $T < 35$  K and  $T > 58$  K,  $R_{xy}^{\text{AH}}$  of the two channels are of the same sign or the positive contribution is below the detection limit of our experiment, rendering the total AHE indistinguishable from that of a single spin-polarized channel (see Fig. 6.12). However, it should be noted that any two curves that add up to the total  $R_{xy}^{\text{AH}}$  are in principle possible.

### 6.3. CONTROL OF THE RELATIVE SPIN POLARIZATIONS

The presence of two channels with different coercive fields provides the possibility to control their relative spin polarizations by choosing the magnetic field span interval  $B_{\text{max}}$  appropriately. By varying  $B$  in the range  $[0, B_{\text{max}}, -B_{\text{max}}, 0]$ , the polarization of one channel can be (partially) switched while the other is less affected. This is illustrated in Fig. 6.6a for different values of  $B_{\text{max}}$ . The simulations are performed by traversing the individual  $R_{\text{AH}}$  curves (determined from the data at 45 K) up to  $B_{\text{max}}$  and summing them to obtain the total  $R_{\text{AH}}$ . It follows that increasing  $B_{\text{max}}$  changes the relative magnitudes of  $R_{xy,I}^{\text{AH}}$  and  $R_{xy,II}^{\text{AH}}$ , replicating the temperature evolution of the AHE. This is summarized in the diagram in Fig. 6.6b, where the magnitudes of  $R_{xy,I}^{\text{AH}}$  and  $R_{xy,II}^{\text{AH}}$  are plotted against  $B_{\text{max}}$ . The crossing of the curves at 0.18 T constitutes the compensation point where  $|R_{xy,I}^{\text{AH}}| = |R_{xy,II}^{\text{AH}}|$  and the height of the apparent peaks is maximum.

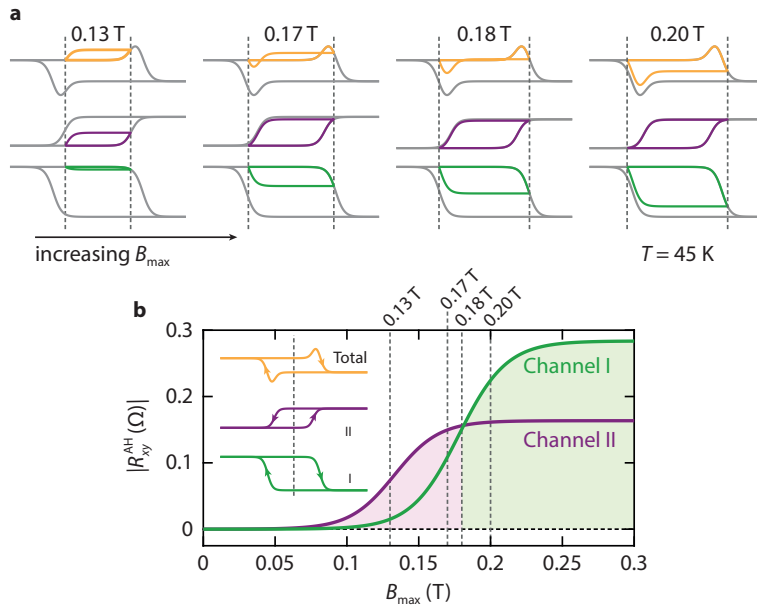


Figure 6.6: **Control of the spin polarization of the two channels.** (a) Simulated  $R_{\text{AH}}$  curves for different values of  $B_{\text{max}}$ . (b)  $|R_{xy}^{\text{AH}}|$  of the separate AH components as a function of  $B_{\text{max}}$ .

The behavior predicted by the simulations is indeed found in the measurements, which is showcased in Fig. 6.7. A difference between the experimental data and the simulations is found at low  $B_{\max}$ , where an asymmetry is observed in the measured  $R_{\text{AH}}$  curves. This can be attributed to a degree of interlayer coupling, quantifiable in the order of tens of mT, which reduces the field required to restore the original magnetic state. Given that the channels have the same spin polarization and carrier type, the opposite anomalous Hall voltages indicate that spin-polarized electrons are accumulated on opposite sides of the two channels. Within this picture, the system is brought to a metastable state at  $B_{\max}$  and tends to restore the initial spin distribution, causing the asymmetry observed in the data. Figure 6.13a shows that the same behavior is observed when the measurement starts from the bottom branch (opposite spin polarization) and is traversed in the opposite direction (in the range  $[0, -B_{\max}, B_{\max}, 0]$ ). As expected, this gives rise to an offset of the center of the hysteresis loop in the opposite  $B$  direction (see Fig. 6.13c).

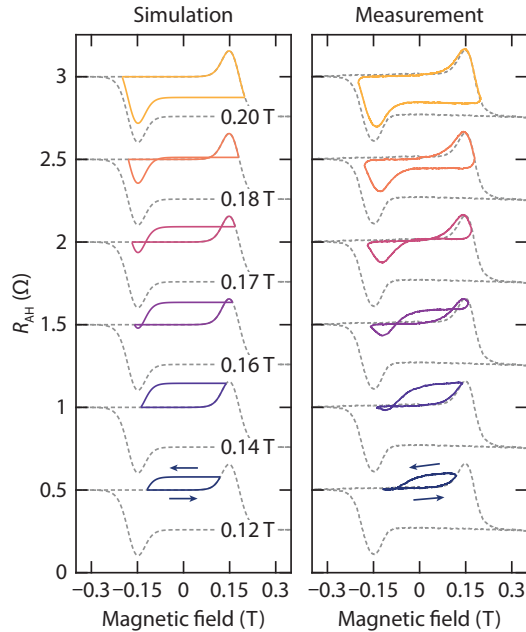


Figure 6.7: **Control of the spin polarization of the two channels.** Simulated (left) and measured (right)  $R_{\text{AH}}$  curves. The curves are offset vertically.

Finally, we compare our results to recent work on SRO thin films and interfaces, where similar anomalous Hall characteristics were observed and attributed to the topological Hall effect due to a skyrmion phase [43–45]. Within this picture, the topological Hall effect should be enhanced in the SIO/SRO/SIO case due to Dzyaloshinskii-Moriya (DM) interaction at both interfaces. Instead, we find that this system displays a regular anomalous Hall effect due to the restoration of inversion symmetry. Additionally, this

scenario relies on the skyrmion phase being present symmetrically around the temperature at which the AHE changes sign, which is highly coincidental. However, two anomalous Hall effects with a shifted  $R_{xy}^{\text{AH}}(T)$  dependence naturally produces this temperature window around  $T_R$ , as there the AHE is of opposite sign. We also show in Figs. 6.11a and 6.11b that considering an anomalous and topological Hall contribution results in an unphysical discontinuity of the coercive field, which is not present in our model. Finally, our model can quantitatively describe the behavior of  $R_{\text{AH}}(B)$ , and correctly predicts the behavior when sweeping the magnetic field to values below saturation. Recent works have shown that Ru vacancies or BaTiO<sub>3</sub> overlayers can also affect the AHE, but the studied systems also present an asymmetry in the form of dissimilar interfaces and a gradient of octahedral rotations [47, 155] which can explain the observed characteristics.

## 6.4. CONCLUSIONS

The atomic-scale control of spin and charge accumulation through Berry phase engineering opens new avenues for spintronic devices and topological electronics. In this respect, transition metal oxides are an ideal platform owing to a delicate interplay between spin, charge and lattice degrees of freedom. Our results establish that oxide interfaces host tunable topological phenomena, thereby providing new perspectives in the field of complex oxides.

# 6

## 6.5. METHODS

SRO/STO, SRO/SIO/STO, and SIO/SRO/SIO/STO heterostructures were prepared by PLD on TiO<sub>2</sub>-terminated STO(001) substrates (CrysTec GmbH). The films were deposited at 600°C in an oxygen pressure of 0.1 mbar. The laser fluence was 1.2 J/cm<sup>2</sup> and the repetition rate was 1 Hz. To refill possible oxygen vacancies formed during the growth, the samples were annealed at 550°C in an oxygen pressure of 300 mbar and cooled down in the same pressure at a rate of 20°C/min. The growth was monitored by RHEED, indicating a layer-by-layer growth mode for the three films.

Atomic scale characterization of the lattice structure was performed on an aberration-corrected scanning transmission electron microscope (STEM). The FEI Titan 80–300 microscope was operated at 300 kV. The samples were prepared in a vacuum transfer box and analyzed in a Gatan Vacuum transfer holder to avoid any influence of air on the film [156, 157]. Collection angles for HAADF imaging, annular bright-field (ABF) imaging and EELS were 44–190 mrad, 8–17 mrad and 47 mrad, respectively. The interfaces are atomically sharp and the STEM-EELS measurements show no diffusion of Ru and Ti, whereas there is a slight diffusion of Ir into the top RuO<sub>2</sub> layer. The heterostructures were further investigated by STM and synchrotron XRD measurements (see Figs. 6.8b and 6.8c). Hall bars were patterned by e-beam lithography, and the heterostructure was contacted by Ar etching and *in-situ* deposition of Pd and Au, resulting in low-resistance Ohmic contacts. An STO cap layer was used to impose symmetric boundary conditions and prevent degradation of the SIO layer [49, 84]. Transport measurements were performed in a He flow cryostat with a 10 T superconducting magnet and a base temperature of 1.5 K. Measurements in current-bias configuration were performed using lock-in amplifiers and custom-made low noise current sources and voltage amplifiers.

First-principles DFT calculations were performed using the VASP [158] package based on plane wave basis set and projector augmented wave method [100]. A plane-wave energy cut-off of 500 eV was used. For the treatment of exchange-correlation, the local spin density approximation (LSDA) with the Perdew–Zunger [159] parametrization of the Ceperly–Alder data [160] for the exchange-correlation functional was considered. The choice of LSDA exchange functional is suggested by a recent paper [161], where it was shown that the Generalized Gradient Approximation is a worse approximation than LSDA for bulk SRO and its heterostructures [130, 162]. In our simulations, the STO/SRO/SIO heterostructure was constructed using a lateral supercell of  $\sqrt{2}a \times \sqrt{2}a$ , while the phases without rotations were contracted using a lateral supercell of  $a \times a$ . The in-plane lattice parameter was fixed to that of the STO substrate, while for the out-of-plane lattice parameters we used the experimental values of the SRO and SIO unit cells. The hopping parameters were estimated from the electronic structure of the non-magnetic SRO/SIO and SRO/STO interfaces without Coulomb repulsion. After obtaining the Bloch wave functions from DFT, the maximally localized Wannier functions [163, 164] were constructed using the WANNIER90 code [165]. Starting from an initial projection of atomic  $d$ -basis functions belonging to the  $t_{2g}$  manifold and centered on metal sites, we obtained the  $t_{2g}$ -like Wannier functions. To extract the hopping parameters from the electronic bands at low energies, we used the Slater–Koster interpolation as implemented in WANNIER90. This approach is applied to determine the real space Hamiltonian matrix elements in the  $t_{2g}$ -like Wannier function basis for the SRO/SIO and SRO/STO interfaces.

## 6.6. SUPPLEMENTARY INFORMATION

### 6.6.1. STRUCTURAL AND MAGNETIC CHARACTERIZATION

In Fig. 6.8 we present the structural and magnetic characterization of our films using various techniques. Figure 6.8a shows the RHEED intensity during the growth of a 4/4/10 u.c. SRO/SIO/STO heterostructure. The clear intensity oscillations indicate that all three layers grow in layer-by-layer mode. The strong initial oscillation during the SRO growth can be attributed to a change in surface termination from  $\text{TiO}_2$  to  $\text{SrO}$ , which is well established for the growth of SRO on  $\text{TiO}_2$ -terminated STO(001) [166]. Figures 6.8b and 6.8c show an STM topographic map and synchrotron diffraction measurements, respectively. The atomically flat surface and clear Laue oscillations indicate that the heterostructures are of high crystalline quality and have sharp interfaces. The magnetization  $M$  of an STO/SRO/STO and an STO/SRO/SIO heterostructure (with 4 u.c. SRO and 2 u.c. SIO) are measured by SQUID magnetometry. Figure 6.8d shows the in- and out-of-plane magnetization of the two samples. Both films have a predominantly out-of-plane magnetization with values reaching approximately 0.6 and 0.8  $\mu_B/\text{Ru}$  at 20 K for STO/SRO/STO and STO/SRO/SIO, respectively. Compared to the STO/SRO/STO, the out-of-plane magnetization of the STO/SRO/SIO is slightly reduced and an in-plane component appears. The appearance of an in-plane magnetization can be attributed to a change of the magnetic anisotropy driven by the modified tetragonality of the SRO unit cell near the SIO interface.

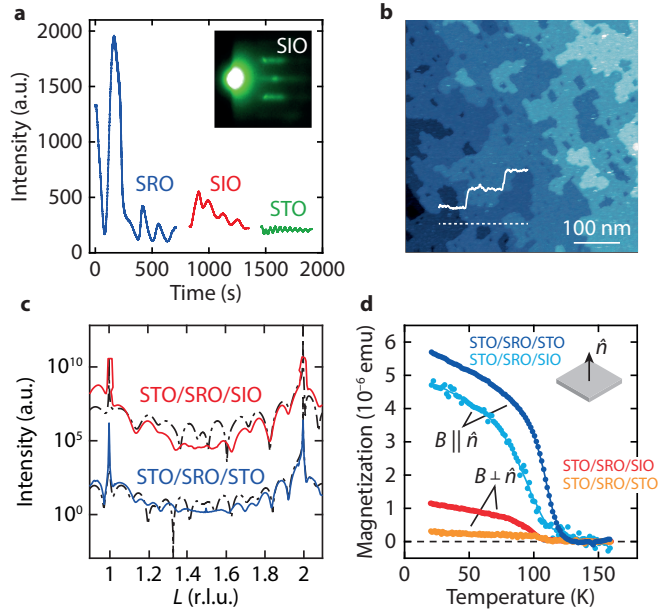


Figure 6.8: **Structural and magnetic characterization.** (a) RHEED intensity oscillations during the growth of SRO, SIO, and STO. Inset: diffraction pattern after SIO growth. (b) STM image of the surface of an STO/SIO/SRO heterostructure. (c) XRD measurements of STO/SRO/STO and STO/SRO/SIO heterostructures. The black dashed lines are simulations of the diffracted intensity. (d) In- and out-of-plane  $M(T)$  of STO/SRO/STO and STO/SRO/SIO. The data was acquired during field-cooling with an applied field of 50 mT.

6

The atomic structure of each interface was investigated using HAADF-STEM combined with EELS. An ADF measurement and EELS chemical maps at the Ti-L<sub>2,3</sub>, Ru-M<sub>4,5</sub>, Sr-L<sub>2,3</sub> and Ir-L<sub>4,5</sub> edges are shown in the first 5 panels of Fig. 6.9. The Ir M edge is at high energy (2 keV) and close to the Sr edge, making it difficult to discern. A combined EELS chemical map (panel 6 of Fig. 6.9) is obtained from the normalized integrated intensities of the aforementioned edges. The color code in this color composite is Sr (red), Ti (yellow), Ir (blue) and Ru (green). A profile of the normalized integrated intensities along the growth direction is shown in the rightmost panel. Since the A-site ion is shared throughout the heterostructure, the interfaces are formed at the B-sites (only the B-site profile is displayed). The Ti/Ru and Ti/Ir interfaces are atomically sharp, and only a single B-site layer displays intermixing. At the Ru/Ir interface, a slight diffusion of Ir into the topmost RuO<sub>2</sub> layer is observed, which corresponds to an Ir content of approximately 20 ± 10%.

### 6.6.2. ADDITIONAL MAGNETOTRANSPORT CHARACTERIZATION

Hall measurements were performed in a wide temperature range to track the evolution of  $R_{xy}^{AH}$  and  $B_c$ . Figure 6.10 shows the AHE of the STO/SRO/STO and STO/SRO/SIO heterostructures (from Figs. 6.4a and 6.4b) from 10 K up to  $T_C$ . Careful analysis of the hysteresis loops enables the extraction of  $R_{xy}^{AH}$  and  $B_c$  as a function of temperature. Near  $T_C$ , the determination of  $R_{xy}^{AH}$  and  $B_c$  is complicated by the more gradual switching of  $M$ .

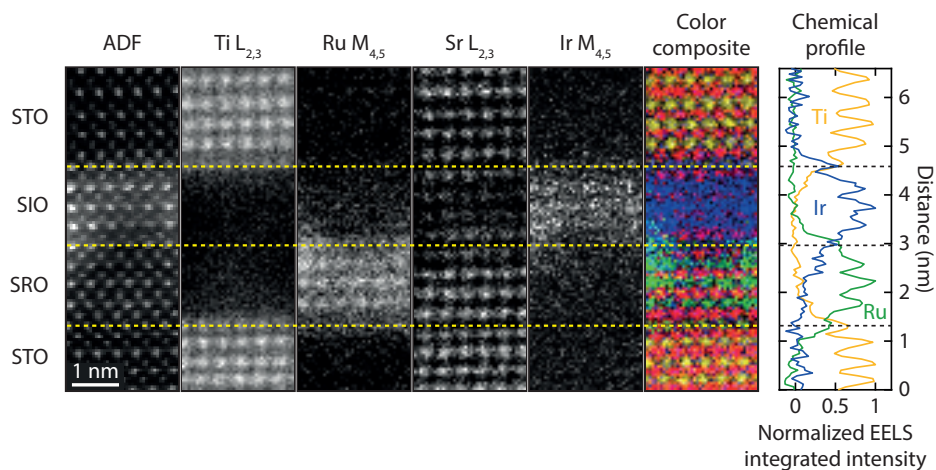


Figure 6.9: **Compositional analysis by STEM-EELS.** From left to right: ADF atomic Z-contrast image, with simultaneously acquired EELS maps of the Ti-L<sub>2,3</sub>, Ru-M<sub>4,5</sub>, Sr-L<sub>2,3</sub> and Ir-M<sub>4,5</sub> edges for an STO/SRO/SIO heterostructure. All atomic maps are overlapped to form the color composite shown in the next panel with Sr (red), Ti (yellow), Ir (blue) and Ru (green). The corresponding normalized intensity profile of the B-sites is shown in the rightmost panel.

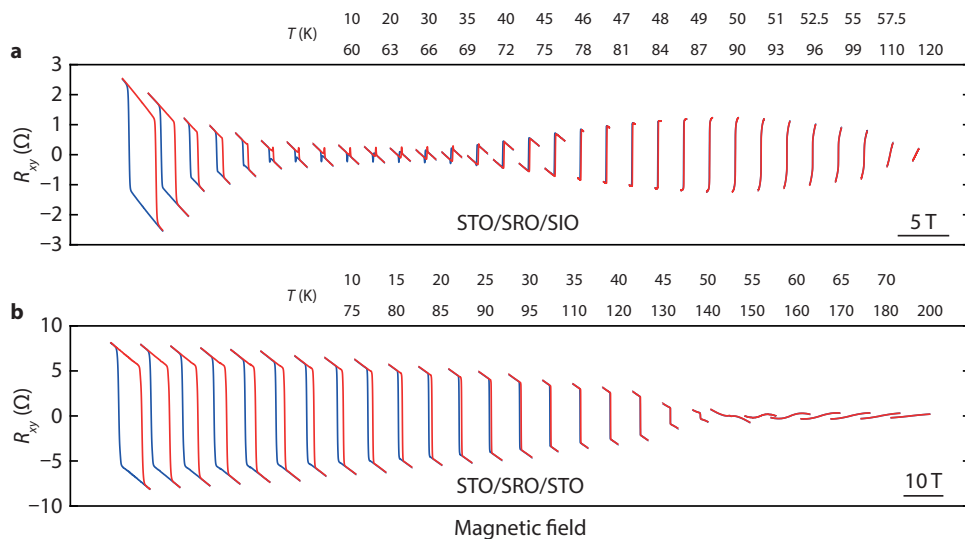


Figure 6.10: **Temperature evolution of the AHE.** Hall effect of (a) an STO/SRO/SIO heterostructure and (b) an STO/SRO/STO heterostructure measured at different temperatures. The AHE of the STO/SRO/STO shows a sign reversal close to  $T_C$ , in agreement with previous measurements on bulk and thin-film SRO.

We now focus on the behavior of  $B_C$  as the sample is cooled through  $T_R$ , the temperature at which the AHE changes sign.  $B_C$  can be determined from by finding the first

zero-crossing of  $R_{xy}$  for  $B > 0$ . This procedure is shown in Fig. 6.11a for the AHE of the STO/SRO/SIO heterostructure around  $T_R$  (the black circles indicate  $B = B_c$ ). It is immediately apparent that this approach fails in assigning a  $B_c$  value to the curve at 48 K. The extracted  $B_c$  values are plotted versus temperature in Fig. 6.11b (left), which reveals an unphysical discontinuity occurring at  $T_R$ . This problem arises within any interpretation that views the total Hall effect as comprising a single anomalous Hall component, with the apparent peaks arising from for example a topological Hall component due to skyrmions. The coercive fields determined from the fits with two anomalous Hall components (right) show a continuous behavior as a function of temperature, which lends strong support to the presence of two anomalous Hall channels. Notably, the carrier density (Fig. 6.11c) determined from the ordinary Hall component does not show an anomaly around  $T_R$ .

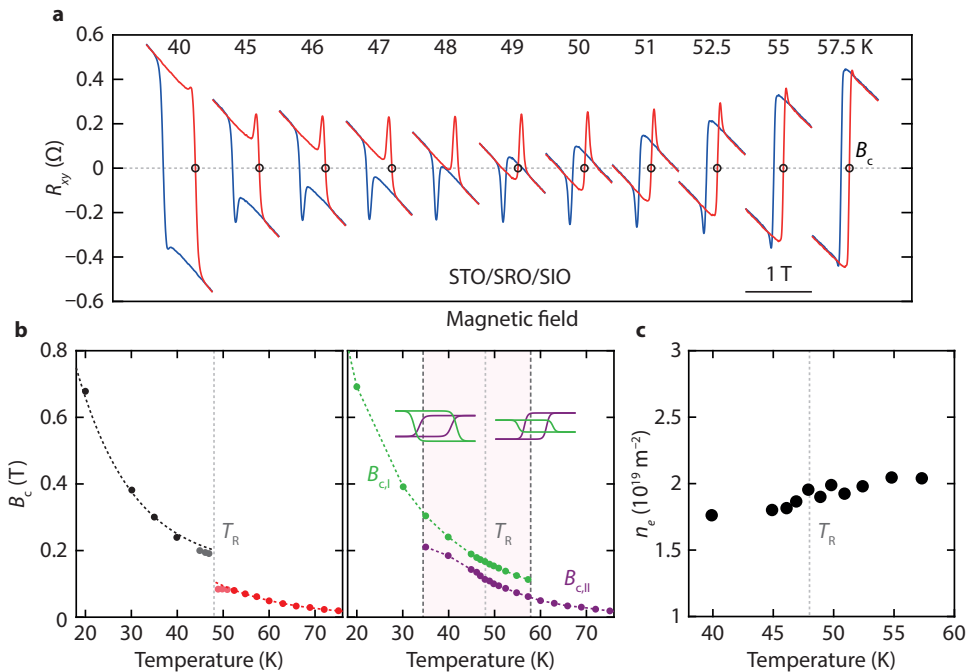


Figure 6.11: **Determination of  $B_c$ .** (a) AHE around the sign reversal. The circles indicate the determined  $B_c$ . (b) Left:  $B_c$  as a function of temperature. At  $T_R$ ,  $B_c$  displays a sudden jump. Right:  $B_c$  determined from the fits with two anomalous Hall components. (c) Carrier density ( $n_e$ ) as a function of temperature, determined from the high-field slopes in (a).

In Fig. 6.12 we investigate the anomalous Hall effect outside of the temperature window where  $R_{xy}^{\text{AH}}$  is of opposite sign ( $35 \text{ K} \leq T < 58 \text{ K}$ ). Based on the extrapolation of the data in Fig. 6.12a (filled circles), we expect  $R_{xy}^{\text{AH}}$  of both channels to be negative for  $T < 35 \text{ K}$  and positive for  $T > 58 \text{ K}$ . This raises the question as to why we do not observe two switching events in the AHE at higher and lower temperatures. We investigate this in Fig. 6.12b by summing the extrapolated loops (green and purple), assuming extrapo-

lated values for  $B_c$  at 30 and 60 K from Fig. 6.12a. The result of the summation (orange) is shown in the panel below, and is compared to a single-loop fit of the data (black lines) in Figs. 6.12c and 6.12d. Due to (i) the slight difference in  $B_c$ , (ii) the considerable slope at  $B_c$  and (iii) the fact that  $R_{xy}^{\text{AH}}$  of one channel is always much smaller than the other, the difference is extremely subtle. This implies that, outside the temperature window, it is nearly impossible to distinguish the two components from AH measurements. Other techniques such as neutron scattering or Lorentz TEM could provide more insight into the magnetic switching at these temperatures and the spatial extent of the two channels.

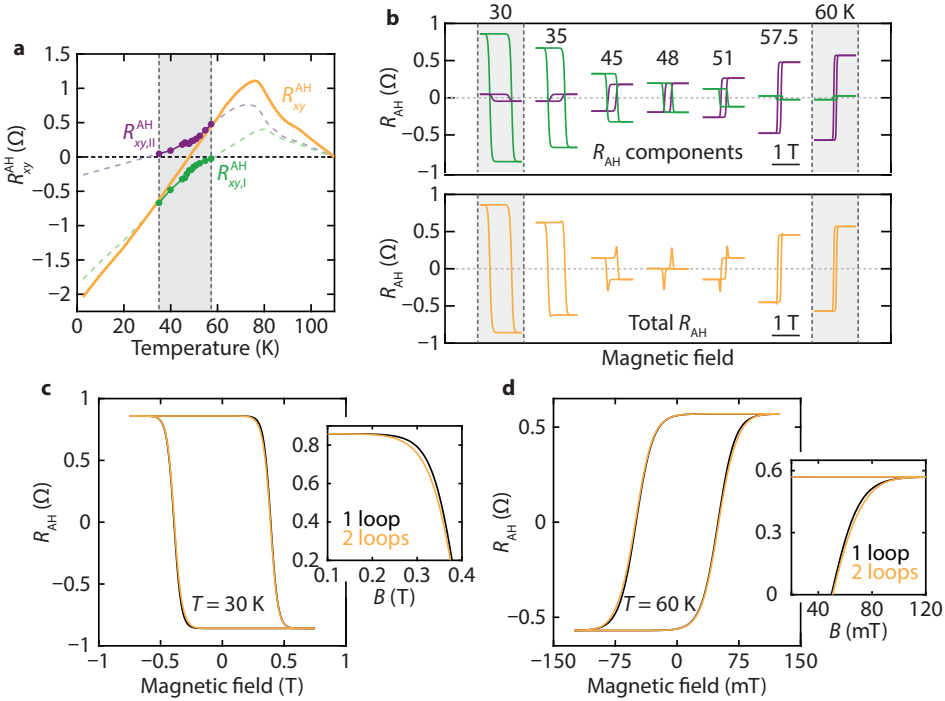


Figure 6.12: **Extrapolation of the anomalous Hall channels.** (a) Total  $R_{xy}^{\text{AH}}$  and the extracted  $R_{xy}^{\text{AH}}$  from the two AH components. The dashed lines illustrate a possible temperature dependence of  $R_{xy}^{\text{AH}}$ . (b) Two AH components (top) that add up to the total  $R_{\text{AH}}$  curves (bottom). At 35 and 60 K, the two components cannot be discerned and the smaller component is based on extrapolation of the data in panel (a). (c) and (d) show a comparison between a single AHE and a total AHE resulting from two anomalous Hall components of the same sign at 30 and 60 K, respectively.

In Fig. 6.13 we present additional measurements on the partial switching of the spin polarization of the two channels. Figure 6.13a shows simulated and measured  $R_{\text{AH}}$  curves similar to those in Fig. 6.7. However, in this case the measurement starts from the bottom branch (opposite spin polarization) and is traversed in the opposite direction (in the range  $[0, -B_{\text{max}}, B_{\text{max}}, 0]$ ). As expected, the measurements are mirrored with respect to those with opposite spin polarization. In Fig. 6.13c we show that the offset of the center of the hysteresis loop is in the opposite  $B$  direction. The shift of the loop is about 37 mT

at 45 K and  $B_{\max} = 0.12$  T (Fig. 6.13b). At higher  $B_{\max}$ , the shift of the center of the loop becomes smaller, which can be understood by the partial switching of polarization of the channel with larger  $B_c$ .

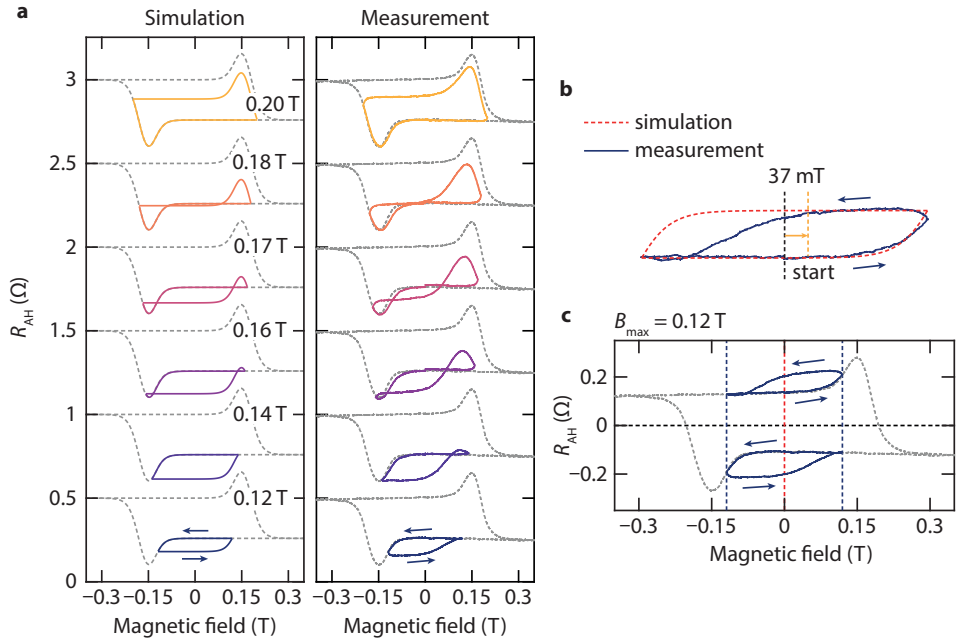


Figure 6.13: **Control of the spin polarization of the two channels.** (a) Simulated (left) and measured (right)  $R_{\text{AH}}$  curves. The curves are offset vertically. (b) Top: comparison of simulated and measured  $R_{\text{AH}}$  for  $B_{\max} = 0.12$  T. (c) Measured  $R_{\text{AH}}$  starting with positive or negative spin polarization.

We next study how varying the SIO and SRO layer thicknesses affects the (magneto)transport properties of the heterostructures. In Fig. 6.14a we show the sheet resistance versus temperature of an STO/4 u.c. SRO/STO heterostructure and three STO/4 u.c. SRO/SIO heterostructures with different SIO layer thicknesses. We find that increasing the number of SIO layers lowers the resistance, indicating that the SIO layer acts as a parallel resistor. Peaks appear around the sign reversal of the AHE irrespective of the film thickness (Fig. 6.14b), strongly suggesting that they originate from interfacial effects. In addition, the residual resistance ratio ( $\text{RRR} = R_{300\text{K}}/R_{1.5\text{K}}$ ) is the same for all STO/SRO/SIO heterostructures and is lowered with respect to the STO/SRO/STO. This further supports that interfacing SRO with SIO (instead of STO) modifies the electronic structure of the SRO film. We note that the temperature at which the AHE changes sign and the magnitude of the apparent peaks are slightly different for the three samples. Since the value of  $T_{\text{R}}$  depends sensitively on the magnetization and only  $T_{\text{R}}$  of the 4/2 heterostructure is different, it is likely due to sample-to-sample variations (e.g., a slight discrepancy in the thickness or crystalline quality of the SRO film). This could also be responsible for the variation in the peak magnitude, which depends on the relative contribution of the each channel to the anomalous Hall resistivity ( $\rho_{xy}$ ).

In the limit of small Hall angles, the total anomalous Hall resistivity is given by

$$\rho_{xy}^{\text{tot}} = \left( \frac{\sigma_{xx}^i}{\sigma_{xx}^{\text{tot}}} \right)^2 \rho_{xy}^i + \left( \frac{\sigma_{xx}^{ii}}{\sigma_{xx}^{\text{tot}}} \right)^2 \rho_{xy}^{ii}, \quad (6.2)$$

where  $\sigma_{xx}$  is the longitudinal conductivity and the indices refer to the two channels. Comparison of our longitudinal and Hall conductivity data shows that  $\sigma_{xy}/\sigma_{xx} = \mathcal{O}(10^{-3})$ , hence the addition of Hall resistivities (measured transverse voltages) is valid. This equation shows that the magnitude of  $\rho_{xy}^{iii}$  is weighted by the respective  $\sigma_{xx}$ . The conductivity of each channel depends on the number of unit cells that contribute, i.e., the number of SRO layers of which the magnetization is affected by each interface. As the two AH channels coexist within the SRO film, their magnitude should in principle not depend on the SIO thickness. However, interlayer hybridization of the electronic states of SRO and SIO could also cause several layers of the SIO film to participate in the AH transport, which would affect the magnitude of  $R_{xy}^{\text{AH}}$ . However, a more systematic study is required to establish such a relation and exclude possible variability in growth conditions.

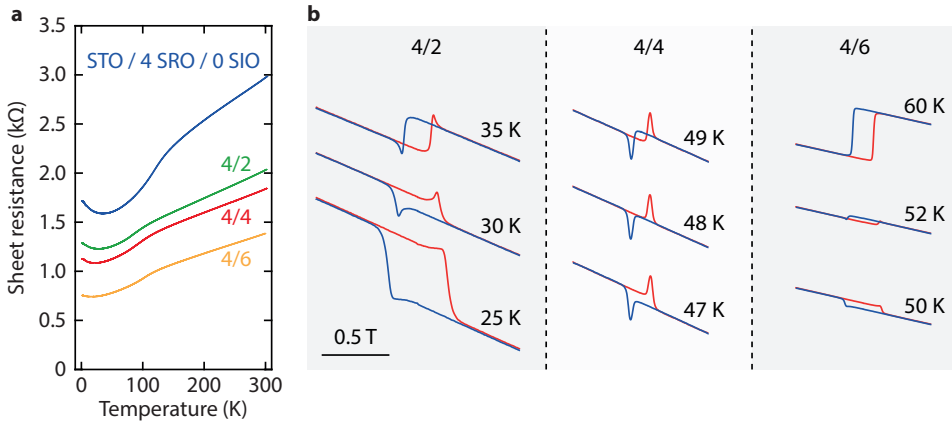


Figure 6.14: **Variation of the SIO film thickness.** (a) Sheet resistance and (b) Hall resistance of STO/SRO/SIO heterostructures with different SIO thicknesses versus temperature.

Figure 6.15a shows the sheet resistance of STO/SRO/4 u.c. SIO heterostructures with SRO thicknesses ranging from 4 to 6 unit cells. With increasing thickness, the resistance is lowered and the magnitude of the low-temperature resistance increase is reduced. Their AHE is shown in Fig. 6.15b for three temperatures around  $T_R$ . All films display an AHE with peaks appearing around  $T_R$ . In Fig. 6.15c we plot  $R_{xy}^{\text{AH}}$  versus temperature, which shows that  $T_R$  increases with film thickness. This can be attributed to an increase of  $M$  with film thickness, which is consistent with the work of Matsuno et al. [43]. Interestingly, the peak magnitude appears to decrease with increasing SRO thickness. This could be due to a smaller contribution of the SRO layers of which the magnetic state is affected by the SIO interface. Considering that the magnetic anisotropy of SRO favors an

out-of-plane magnetization, we expect the canting of the easy-axis induced by the SIO interface to be limited to a few unit cells. Within this picture, the contribution of the channel constituted by the SRO layers near the SIO interface to  $\rho_{xy}$  would be reduced as the SRO thickness is increased, which is in agreement with our observations.

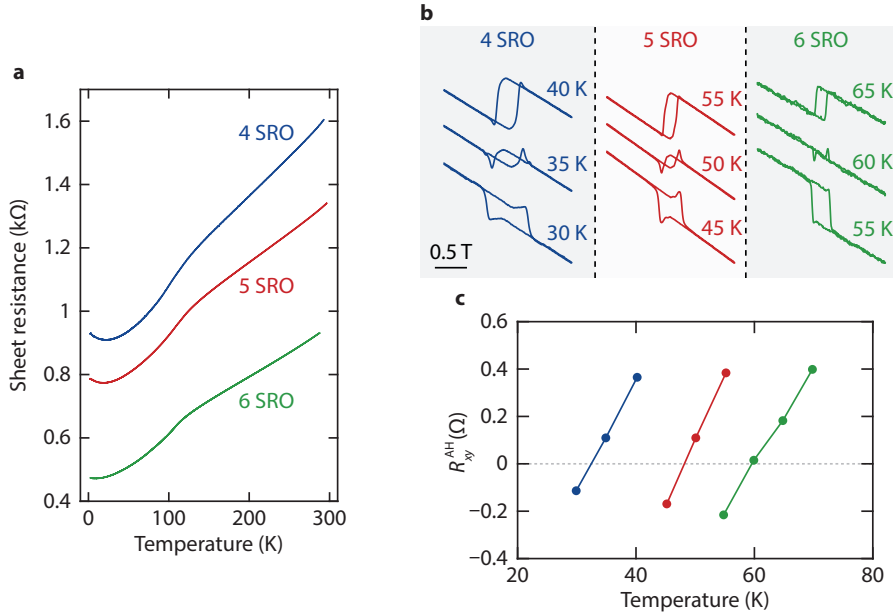


Figure 6.15: **Variation of the SRO layer thickness.** Sheet resistance (a) and Hall resistance (b) of STO/SRO/SIO heterostructures with different SRO thicknesses versus temperature. (c)  $R_{xy}^{AH}$  as a function of temperature.

### 6.6.3. ANOMALOUS HALL EFFECT IN ULTRATHIN SRO BILAYERS

Based on the proposed mechanism underlying the unconventional AHE in STO/SRO/SIO heterostructures, we designed the following experiment. We consider a heterostructure with two ultrathin SRO films separated by an insulating spacer layer rather than two channels that coexist within a single SRO film. In either case, (magneto)transport measurements will probe both channels as they are electrically in parallel. To be able to discern the two AH components, both  $T_R$  and  $B_C$  of the two channels have to be significantly different, while their magnitudes ( $R_{xy}^{AH}$ ) have to be comparable. In the case that  $B_C$  is nearly equal, a difference in the slope at  $B_C$  (the parameter  $\omega$ ) would still allow the identification of two AH channels. In this case, similar characteristics as those shown in Fig. 6.5a should appear. We prepared a heterostructure composed of STO/4 u.c. SRO/4 u.c. STO/5 u.c. SRO/10 u.c. STO to test this hypothesis (see Fig. 6.16a). The same number of pulses were used to grow the bottom and top SRO layers, which differ 1 u.c. in thickness due to the initial change of the STO surface termination from  $\text{TiO}_2$  to SrO.

The two layers are contacted by ultrasonic wire bonding to the 4 corners of the sample with AlSi bonding wire, and the four-terminal resistance is measured in van der Pauw

configuration. An  $R(T)$  measurement of the heterostructure is shown in Fig. 6.16b. The bilayer system is rather metallic, with an RRR of over 2. The derivative ( $dR/dT$ ) is shown in the inset, where a sharp peak is observed at approximately 130 K. Careful inspection reveals a shoulder slightly to the left of this peak, which is suggestive of a second magnetic transition at around 120 K. The temperature evolution of  $R_{xy}^{\text{AH}}$  is determined by measuring  $R_{xy}(T)$  with +50 mT and -50 mT and calculating the difference between the two curves. This removes any voltage offset originating from misalignment of the contacts and/or inhomogeneous current flow, thus providing the height of the AHE plus a (negligible) contribution from the ordinary Hall effect that remains approximately constant in temperature. The result of this measurement is shown in Fig. 6.16c (bottom). The behavior is similar to that of a single SRO layer (see Figs. 1.8a and 6.2c) and does not show a clear signal of a second magnetic phase.

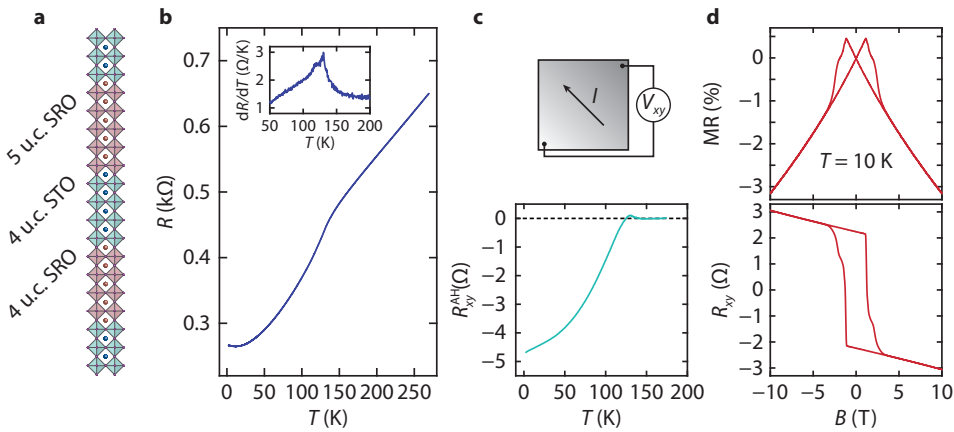


Figure 6.16: **Magnetotransport in ultrathin SRO bilayers.** (a) Schematic of the heterostructure. (b) Sheet resistance versus temperature. The inset shows the derivative ( $dR/dT$ ). (c) Top: schematic of the measurement configuration. Bottom: magnitude of the AHE ( $R_{xy}^{\text{AH}}$ ) as a function of temperature. (d) MR (top) and Hall resistance (bottom) as a function of temperature.

Signatures of a second magnetic phase can however be detected in the magnetic field dependence of the longitudinal and Hall resistance (Fig. 6.16d). Both the MR (top) and Hall data (bottom) show that two magnetic transitions take place at different  $B_c$ . This provides a clear indication of the presence of two spin-polarized conduction channels. From the Hall measurement we can clearly recognize that the magnetization of one channel switches very abruptly, while that of the other channel switches more gradually. We attribute the channel that switches abruptly to the bottom SRO layer, as it is likely more ordered due to the growth on the atomically flat surface of the STO substrate. This is consistent with the abrupt switching observed for a single SRO layer (see e.g. 6.2b). We expect the second SRO layer to be more disordered as it is grown on top of the STO/SRO/STO stack, which has accumulated some surface roughness. The concomitant variations in thickness could give rise to magnetic domains which switch at slightly different fields, resulting in a larger slope at  $B_c$ .

Having established the presence of two spin-polarized conduction channels, we next

study their evolution by measuring the AHE at different temperatures (Fig. 6.17). With increasing temperature, the overall sign of the AHE changes from negative to positive consistent with Fig. 6.16c. In addition, features are present that are reminiscent of the peaks observed in SRO/SIO heterostructures and previously referenced work. This is particularly clear in Fig. 6.17b, where three measurements close to  $T_R$  are shown.

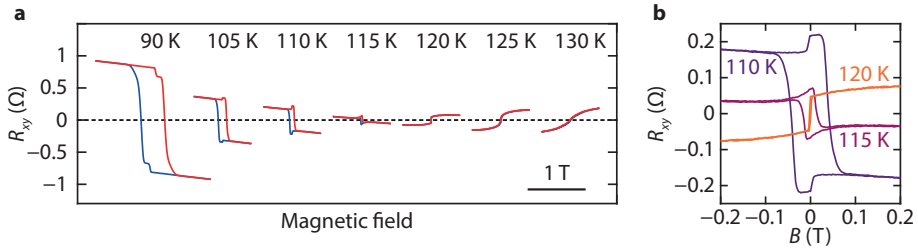


Figure 6.17: **Temperature evolution of the AHE in SRO bilayers.** (a)  $R_{xy}$  measured at different temperatures. The curves are offset horizontally. (b)  $R_{xy}$  measured at three temperatures close to  $T_R$ .

## 6

An overview of the qualitatively different behaviors is presented in Fig. 6.18. The top row shows the measured  $R_{xy}$ , while the middle and bottom rows show simulated AH curves. The green curves (middle row) are modeled by  $R_0 B + R_{xy,I}^{AH} \tanh(\omega_I(B - B_{c,I})) + R_{xy,II}^{AH} \tanh(\omega_{II}(B - B_{c,II}))$  to qualitatively match the measured  $R_{xy}$ . The blue and red curves (bottom row) are the individual AH components used for the simulation. Note that both the width ( $B_c$ ) and the height ( $R_{xy}^{AH}$ ) of the hysteresis loops in this figure are arbitrary. The simulated curves provide an excellent description of the experimentally observed behavior. Both AH components show a sign change and a decrease of  $B_c$  with increasing temperature, consistent with the behavior of single SRO layers. The large variety of observed behaviors arises from the crossover of the coercive fields with temperature and the different  $T_R$  of the two films. As discussed previously,  $T_R$  is determined by the balance between topologically nontrivial  $\mathcal{C} = 2$  and  $\mathcal{C} = -2$  bands, which depends on the magnitude of the out-of-plane magnetization. The crossover of  $B_c$  can be clearly seen in Fig. 6.18: at 10 K,  $B_c$  of the blue curve (bottom SRO) is larger than that of the red curve (top SRO), while at 90 K it is smaller. This is a consequence of the different switching mechanisms which could be influenced either by the crystal structure (magnetic anisotropy) or by inhomogeneity (magnetic domains).

The results presented in this section lend strong support to the two-channel explanation proposed for (001)-oriented STO/SRO/SIO trilayer systems. An important difference is that, in the SRO bilayer case,  $B_c$  and  $\omega$  of the two channels are sufficiently different to allow for their identification even when the AHE is of the same sign. In addition, here the two channels are electrically and magnetically decoupled owing to the STO spacer layer. The situation is therefore less complex than that of asymmetric SRO interfaces, where the two channels are coexisting.

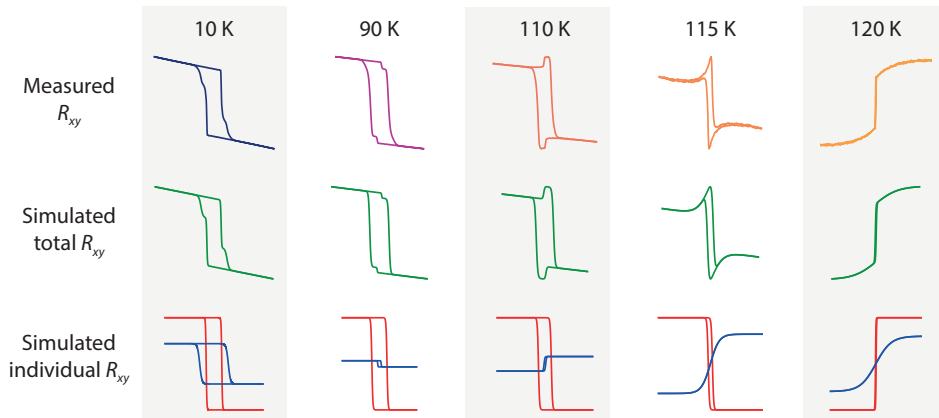


Figure 6.18: **Overview of the qualitatively different behaviors of the AHE.** Measured (top row) vs. simulated (middle and bottom rows)  $R_{xy}$ . The bottom row shows the individual AH components that, together with the ordinary Hall component, constitute the total Hall effect (middle row).

#### 6.6.4. (111)-ORIENTED STO/SRO/SIO HETEROSTRUCTURES

We now consider the DM interaction at (001)- and (111)-oriented SRO/SIO interfaces. At (001)-oriented interfaces, the Ir ions are situated directly above the Ru ions. As a result, the DMI between two Ru sites mediated by the Ir ion is not well defined. In fact, due to the tetragonal symmetry (as is the case for our SRO/SIO interfaces), interactions mediated by neighbouring Ir atoms produce DM vectors with opposite signs, causing the net DMI to be zero. A net DMI can only result from two Ru sites by tilting of Ru-O-Ru bonds, as described in Ref. [47]. This calls into question the role of Ir in producing a topological Hall effect at (001)-oriented SRO/SIO interfaces as first presented in ref. [43]. However, the symmetry at (111)-oriented SRO/SIO does allow for a net DMI, as shown in Fig. 6.19. The DM vectors are however oriented differently from other systems with skyrmion lattices such as Fe/Ir(111) [37].

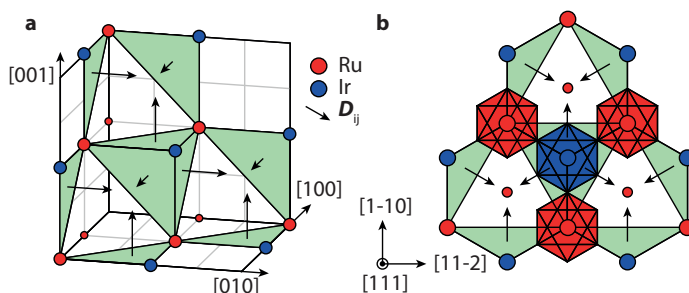


Figure 6.19: **DMI at (111)-oriented interfaces.** (a) Schematic of a heterostructure consisting of two  $\text{Ru}^{4+}$  planes and one  $\text{Ir}^{4+}$  plane stacked along the (111) crystallographic direction. The  $(\text{SrO}_3)^{4-}$  planes are not shown for clarity. The green triangles and black arrows denote the DMI triangles and vectors, respectively. (b) Top view of the  $\text{Ru}^{4+}$  and  $\text{Ir}^{4+}$  layers. Oxygen octahedra are shown for the central Ir atom and its neighboring Ru atoms.

The transition metal ions in a (111) bilayer are located on a honeycomb lattice consisting of two trigonal sublattices on different layers. In this structure, neighbouring spins on the Ru sites experience a DMI mediated by the Ir atom in the upper layer, resulting in DM vectors that are oriented along the (100), (010), and (001) axes. (111)-oriented SRO/SIO interfaces are therefore promising candidates for the stabilization of skyrmion spin textures. We prepare SRO/SIO interfaces by depositing SRO and SIO films on commercially available Ti-rich terminated STO(111) substrates. The growth temperature was 600°C, the deposition pressure 0.1 mbar and the laser fluence 1.2 J/cm<sup>2</sup>. The growth was monitored by RHEED, shown in Fig. 6.20. The RHEED intensity oscillations indicate a layer-by-layer growth mode, and AFM measurements (inset) show that the step-and-terrace structure of the substrates is preserved and the surfaces are atomically flat. The film thicknesses were 8 and 2 u.c. of SRO and SIO, respectively. Both films were capped with 10 u.c. STO to preserve the properties during lithographic processing. The film thickness of 8 u.c. was chosen to be similar to that of 5 u.c. SRO along the (001) direction ( $\approx 2$  nm).

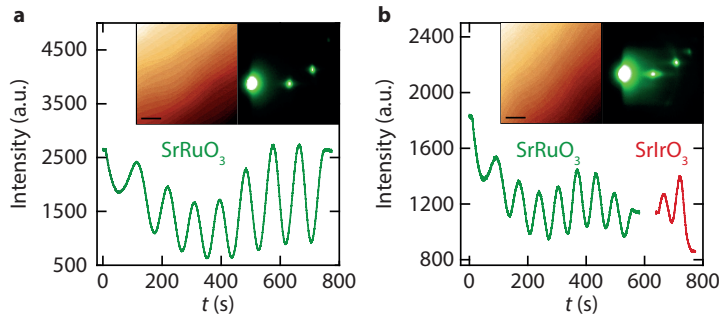


Figure 6.20: **Growth and characterization of (111)-oriented heterostructures.** RHEED oscillations during the growth of (a) SRO and (b) STO/SRO/SIO heterostructures on (111)STO. The insets show AFM measurements of the film surface and RHEED diffraction patterns after the growth of the (a) SRO and (b) SIO layer.

The films were patterned into Hall bars (Fig. 6.21c) in order to perform accurate (magneto)transport measurements. Figure 6.21a shows  $R(T)$  curves of (001)- and (111)-oriented STO/SRO/STO and a (111)-oriented STO/SRO/SIO heterostructure. The  $R(T)$  curves of the (001)- and (111)-oriented SRO are similar, the latter being slightly more metallic. In contrast with the (001) case, interfacing SRO with SIO along the (111) direction increases the resistance of the system below  $T_C$ . This indicates that the SIO layer does not act as a parallel conduction channel. The interface with SIO does, however, affect electronic transport in the SRO layer as the SRO becomes ferromagnetic.

Hall measurements (Fig. 6.21b) reveal more differences between (001)- and (111)-oriented SRO films and SRO/SIO interfaces. First, we find that  $B_C$  of SRO(111) is substantially lower than that of SRO(001). Second, the ordinary Hall effect of SRO(111) is found to be strongly nonlinear, while SRO(001) always displays a linear ordinary Hall effect. This could be due to the occupation of multiple electron bands or a secondary magnetic phase that provides an additional anomalous Hall contribution. The nonlinear Hall component can be subtracted from the data by selecting the following segments

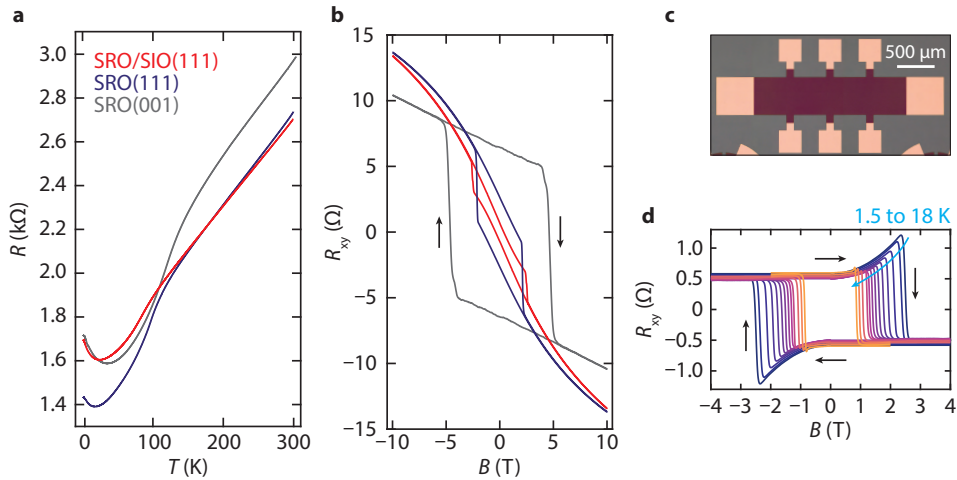


Figure 6.21: **(Magneto)transport in (001)- and (111)-oriented SRO and STO/SRO/SIO.** (a) Sheet resistance versus temperature. (b) Hall effect measured at 1.5 K. (c) Optical image of a patterned Hall bar before lift-off of the resist mask. (d)  $R_{xy}$  measured at different temperatures after subtraction of the ordinary Hall component.

of the  $R_{xy}(B)$  data:  $[-10, 0 \text{ T}]$  and  $[10, 0 \text{ T}]$ . Doing so for the SRO(111) film produces a conventional anomalous Hall effect. For the SRO/SIO(111) heterostructure, however, a strong curvature is observed below the coercive field, as shown in Fig. 6.21d. This increase of the Hall resistance is present at all temperatures below  $T_c$ . Given the net DMI at the SRO/SIO(111) interface, this could originate from a noncollinear magnetic state. However, considering our discussion of the origin of the unconventional AHE in (001)-oriented SRO/SIO, it could also be attributed to a second anomalous Hall channel that provides a positive contribution to the AHE. Further investigation is required to uncover its origin and that of the nonlinear Hall effect in (111)-oriented SRO films.



# 7

## ULTRATHIN COMPLEX OXIDE NANOMECHANICAL RESONATORS

*Sometimes I've believed as many as six  
impossible things before breakfast.*

Lewis Carroll

*In previous chapters we have seen that the electronic and magnetic properties of thin films can be strongly affected by epitaxial interfaces, which are often used to control properties on demand by engineering strain or symmetry mismatches. However, the use of a substrate for thin film growth is unavoidable and can also constrain the possibilities for mechanical manipulation, integration with electronics, and optical studies. Recently it has become possible to isolate thin films from their substrate using a buffer layer, enabling the study of their properties in the absence of interface effects. In this chapter, we create ultrathin membranes of strongly correlated materials and fabricate nanomechanical resonators made of freestanding STO and SRO films. Using laser interferometry, we successfully actuate and measure the motion of the nanodrum resonators. By measuring the temperature dependence of their mechanical response, we observe signatures of structural phase transitions in the STO, which affect the strain and mechanical dissipation of the resonators. This approach can be extended to investigate phase transitions in a wide range of materials.*

---

Parts of this chapter have been submitted for peer review (2018) by D. Davidovikj, D. J. Groenendijk, A. M. R. V. L. Monteiro, A. Dijkhoff, D. Afanasiev, Y. Huang, E. van Heumen, H. S. J. van der Zant, A. D. Caviglia, and P. G. Steeneken.

D. Davidovikj performed the mechanical characterization of the resonators. D. Afanasiev performed the second harmonic generation measurements.

IT is well established that the electronic and magnetic properties of complex oxides are extremely sensitive to mechanical strain due to the strong coupling between the lattice and the charge, spin, and orbital degrees of freedom [167–170]. This sensitivity stems from rotations and distortions of the corner-connected  $\text{BO}_6$  octahedra (where B is a transition metal ion situated in the centre of the octahedron formed by the oxygen atoms), which determine the overlap between orbitals on adjacent atomic sites [171]. The B–O bond lengths and rotation angles are routinely controlled by strain through heteroepitaxy, which forms a powerful tool to tune the properties of ultrathin films. The strong dependence of their electronic properties on mechanical strain has attracted a lot of attention towards their implementation in nanoelectromechanical sensors and actuators [172], but exploiting this trait to the fullest has been limited by the requirement of a substrate for the epitaxial growth. This constrains the possibilities for their mechanical manipulation and integration with electronics and it could not be circumvented until recently, when single-crystal films of complex oxides were successfully released and transferred [173, 174]. This sparked a new wave of interest in studying the intrinsic properties of these materials, this time in their isolated, ultrathin form.

On the other hand, a wide variety of mechanical manipulation techniques have been developed for another family of ultrathin materials, the so-called van der Waals materials [175], where weak interlayer bonding enables exfoliation of single- and few-layer films. Their ease of manipulation has enabled the top-down fabrication of a variety of nanomechanical elements, such as suspended membranes and ribbons. This, combined with their flexibility, low mass and remarkable strength, has made them extremely promising candidates for nanomechanical sensing applications [176–179]. The well-developed field of nanomechanics has established a solid basis for characterizing the thermal and mechanical properties of van der Waals materials [180–182]. In this chapter, we utilize the mechanical manipulation techniques for van der Waals materials to realize ultrathin nanomechanical resonators made of epitaxially grown single-crystal complex oxide films. We show that these devices can be used to detect signatures of temperature-induced phase transitions in the material, which are related to its intrinsic properties and the configuration and dynamics of structural domains.

## 7.1. PREPARATION OF FREESTANDING FILMS

The fabrication of the complex oxide mechanical resonators is described in Fig. 7.1. To isolate the epitaxial STO and SRO thin films from the substrate, a water-soluble epitaxial  $\text{Sr}_3\text{Al}_2\text{O}_6$  (SAO) layer is first deposited by PLD on a  $\text{TiO}_2$ -terminated STO(001) substrate. Figure 7.1a shows the RHEED intensity of the specular spot during the growth of SAO and STO. Oscillations are observed during the growth of both films, indicating that the growth occurs in layer-by-layer mode. An AFM topographic map shows that the STO surface has a step-and-terrace structure, corroborating the growth mode. SRO grows in step-flow mode, as can be inferred from the atomically flat surface and the absence of RHEED oscillations. An XRD measurement of an STO/SAO/SRO heterostructure is shown in Fig. 7.6c in Section 7.6.1.

To dissolve the sacrificial layer and detach the thin film from the substrate, a polydimethylsiloxane (PDMS) layer is adhered to the surface before the entire stack is immersed in deionized water. After the dissolution of the SAO layer (approximately 1 hour

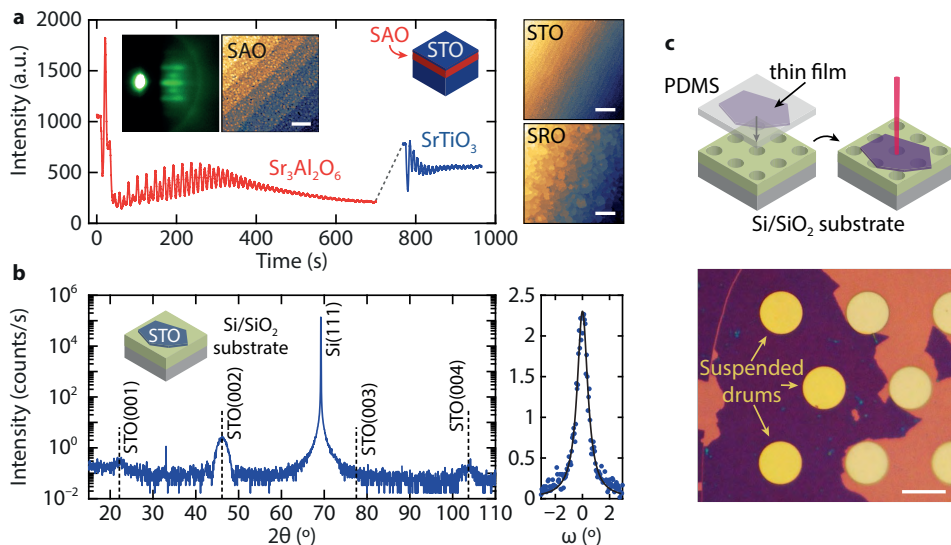


Figure 7.1: **Sample fabrication and basic characterization.** (a) Left: RHEED intensity oscillations during the growth of SAO and STO. Inset: RHEED diffraction pattern (left) and AFM image (right) of the SAO surface. The scale bar is 200 nm. Right: AFM images of the STO (top) and SRO (bottom) film surfaces. The scale bar is 1  $\mu\text{m}$ . (b) XRD measurement of a 10 u.c. STO film transferred on a Si/SiO<sub>2</sub> substrate. Right: rocking curve around the (002) reflection. (c) Top: schematics of the transfer of a thin SRO film onto a pre-patterned Si/SiO<sub>2</sub> substrate. Bottom: optical image of suspended 9 u.c. SRO drums with a diameter of 13  $\mu\text{m}$ . The scale bar is 10  $\mu\text{m}$ .

for a  $5 \times 5 \text{ mm}^2$  50 nm-thick SAO film), the film can be transferred onto other substrates such as Si/SiO<sub>2</sub> using a deterministic dry-transfer technique [183]. An XRD measurement of a 10 u.c. STO flake on a Si/SiO<sub>2</sub> substrate is shown in Fig. 7.1b (left). Finite size oscillations are still visible, indicating that the films are of excellent crystalline quality after the release and transfer process. Since the film is no longer epitaxial on the substrate, the rocking curve (right) is a measure of the morphology of the STO film lying on the SiO<sub>2</sub>. The small full width at half maximum ( $0.95^\circ$ ) indicates that the film lies very flat on the Si/SiO<sub>2</sub> substrate. Here the technique for releasing oxide films is extended by transferring STO and SRO films onto Si/SiO<sub>2</sub> substrates pre-patterned with circular cavities, demonstrating the feasibility of creating suspended complex oxides membranes. An optical image of 9 u.c. (thickness:  $h = 3.6 \text{ nm}$ ) thick SRO drums (diameter:  $d = 13 \mu\text{m}$ ) is shown in Fig. 7.1c. It is remarkable that these materials, much like their van der Waals counterparts, have the flexibility and tensile strength required to be suspended with aspect ratios exceeding  $d/h > 3600$ .

## 7.2. MECHANICAL CHARACTERIZATION OF OXIDE RESONATORS

We characterize the high-frequency dynamics of the complex oxide nanodrums using the optical actuation and detection setup shown in Fig. 7.2. The drums are mounted in the vacuum chamber ( $10^{-6}$  mbar) of a closed-cycle cryostat with optical access. Their motion is read out using a red HeNe laser ( $\lambda = 632.8 \text{ nm}$ ). The complex oxide membrane

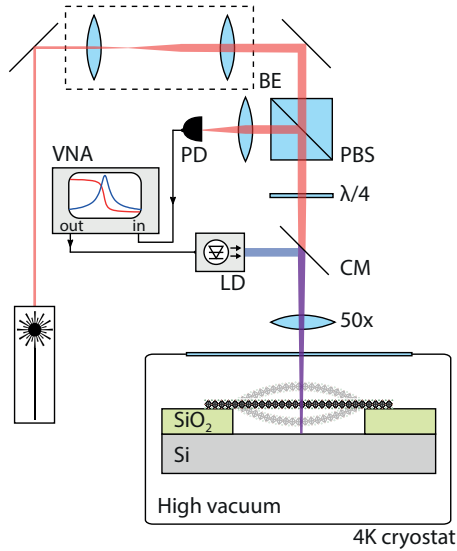


Figure 7.2: **Optical actuation and detection setup.** Setup for interferometric displacement detection (VNA: vector network analyser, PD: photodiode, LD: laser diode, BE: beam expander, PBS: polarised beam splitter, CM: cold mirror).

## 7

and the silicon underneath form a Fabry–Pérot cavity, where the motion of the membrane modulates the intensity of the reflected light, which is measured by a photodiode. The resonators are actuated optothermally using a blue laser that is coupled into the optical path via a cold mirror [184, 185]. Measurements are performed in a homodyne detection scheme using a vector network analyser (VNA), simultaneously sweeping the actuation and detection frequencies.

The mechanical resonances of several STO and SRO drums are shown in Fig. 7.3. Although STO is transparent in the visible range [186], the motion of the drums can still be actuated and measured optically since the refractive index of the STO is different from that of vacuum. Figures 7.3a and 7.3b show measurements of two STO drums, and Figs. 7.3d and 7.3e of two SRO drums of different diameters. Measurements over a wider frequency range show that higher order resonances of the drums can also be detected; two examples are shown in Figs. 7.3c and 7.3f, where up to four higher order resonances are visible. By taking the ratio of the second harmonic to the fundamental mode, we can estimate whether the mechanical properties are dictated by the pre-tension (theoretical ratio 1.59) or if they are dominantly determined by the bending rigidity (theoretical ratio 2.09), the latter being dependent on the Young’s modulus of the material ( $E$ ). It can be seen from Fig. 7.3c that the STO drums are in a crossover regime (ratio 1.72), similar to what has been observed in drums of similar dimensions made of  $\text{MoS}_2$  [185] and  $\text{TaSe}_2$  [187]. On the other hand, the mechanical properties of the SRO drums are almost entirely determined by their pre-tension since  $f_1/f_0 = 1.47$ , which is close to the theoretical value of 1.59.

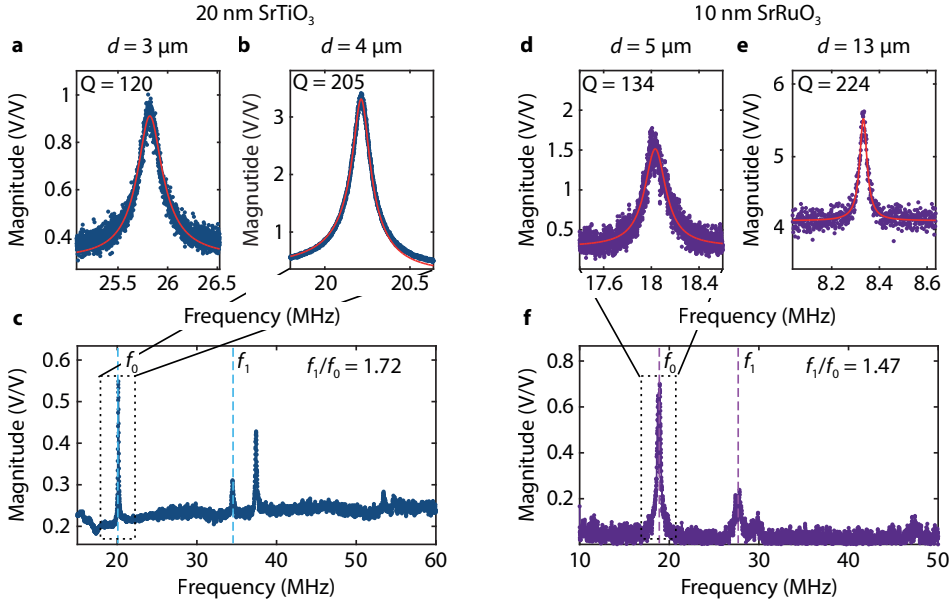


Figure 7.3: **Mechanical characterization of STO and SRO nanodrums.** Frequency spectra of two STO drums with diameters of (a)  $3 \mu\text{m}$  and (b)  $4 \mu\text{m}$ . The red lines are linear harmonic oscillator fits. The extracted quality factors are shown in the top left corners of the panels. (c) Wide-range frequency spectrum of the drum shown in (b). The positions of the fundamental resonance mode ( $f_0$ ) and the second resonance mode ( $f_1$ ) are marked with vertical dashed lines. (d) and (e) show frequency spectra of two SRO drums with diameters of  $5 \mu\text{m}$  and  $13 \mu\text{m}$ , respectively. (f) Wide-range frequency spectrum of the drum shown in (d).

### 7.3. TEMPERATURE-DEPENDENT MECHANICAL PROPERTIES

Having confirmed that the resonators can be mechanically characterized at room temperature, we now investigate how their mechanical properties change with temperature. STO is known to undergo a number of phase transitions as a function of temperature, which are expected to influence the mechanical properties of the resonators. Figure 7.4 shows the temperature dependence of the mechanical properties of an STO nanodrum. The resonance frequency (Fig. 7.4a) shows a temperature evolution which is commonly observed in 2D materials [188–190]. This behavior is usually ascribed to a difference in thermal expansion coefficient between the membrane and the substrate [189, 190], which results in thermally induced tensile stress. Since the resonance frequency is related to the thermal expansion coefficient ( $f_0^2 \propto \alpha_{\text{eff}} T$ ), an abrupt change in  $\alpha_{\text{eff}}$  will noticeably affect  $f_0$ . Interestingly, two discontinuities are observed in Fig. 7.4a: a deviation of  $f_0$  below 165 K and a kink in  $f_0$  at around 30 K (Fig. 7.4a, inset).

Below 105 K, the cubic structure of bulk STO breaks up into locally ordered tetragonal domains joined by ferroelastic domain walls [191, 192]. Another phase transition occurs at around 30 K, below which the Sr-ions disorder along [111] directions, rendering the structure locally triclinic [193–195]. Both transitions are accompanied by changes in mechanical properties [196–200], as well as in the thermal expansion coef-

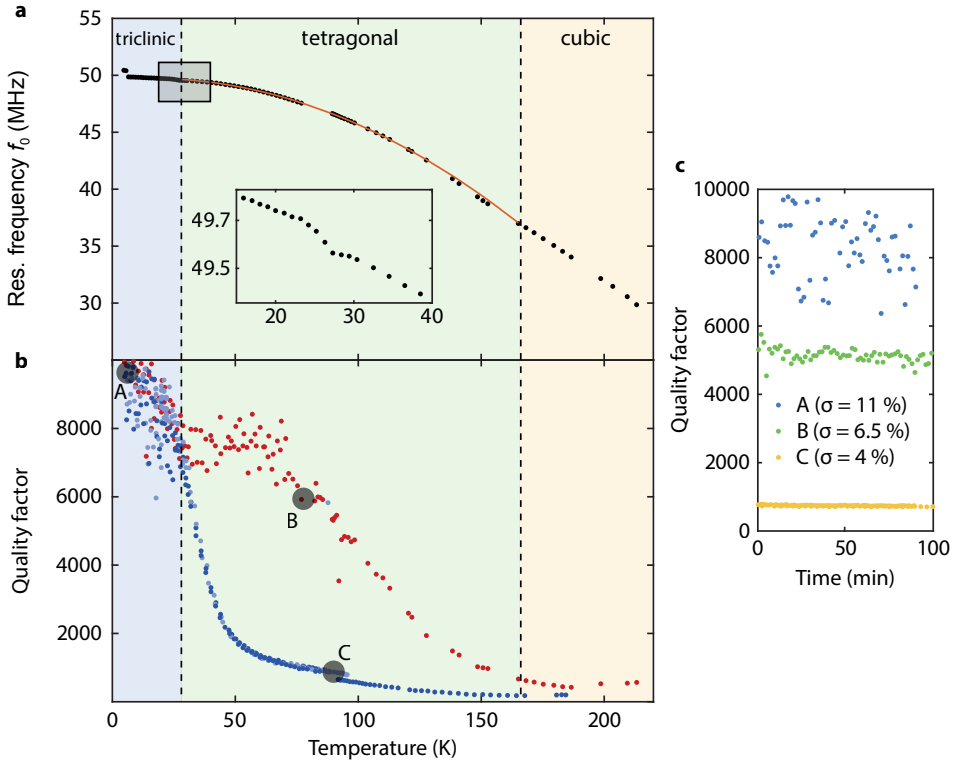


Figure 7.4: **Temperature dependence of the mechanical properties of a 4  $\mu\text{m}$  STO drum.** (a) Resonance frequency as a function of temperature (upward sweep). The red line is a parabolic fit to the data. The inset shows a zoomed-in region in the range between 15 and 40 K. (b) Quality factor as a function of temperature for seven alternating temperature sweeps. Two distinct branches are distinguishable in the region between 30 and 165 K (dashed lines), coloured in red and blue. The light blue points correspond to cooling cycles. (c) Quality factor as a function of time at constant temperatures, where A, B, and C correspond to the points shown in (b).

efficient of STO [201] and can therefore be responsible for the signatures at 165 K and 30 K in Fig. 7.4a. The difference between the observed transition temperature of 165 K and the bulk value of 105 K can be attributed to surface effects [202] and thermally induced strain [203]. Additional evidence for an elevated cubic-to-tetragonal transition temperature is found from second harmonic generation (SHG) measurements that show a feature around 157 K (see Fig. 7.7). The fact that the resonance frequency increases with decreasing temperature, despite the decrease of the Young's modulus of bulk STO below the transition temperature [197, 200] indicates that the mechanical behavior of the resonator is dominated by tension, rather than bending rigidity [185].

While the phase transitions only lead to relatively small shifts in the resonance frequency, they greatly impact the measured mechanical dissipation, as shown in Fig. 7.4b. To characterize dissipation we use the quality factor of the resonator, which is extracted from the frequency domain measurements as  $Q = f_0/\Delta f$  ( $\Delta f$  is the full width at half maximum of the resonance peak). Whereas  $f_0$  is influenced both by the pre-tension of

the membrane and the Young's modulus of the STO, the quality factor is also dependent on the intrinsic losses in the material ( $Q \propto E_1/E_2$  for a complex Young's modulus  $E = E_1 + iE_2$  [204]). In Fig. 7.4b we show the evolution of the  $Q$  factor for 7 alternating upward and downward temperature sweeps. At temperatures below 30 K and above 165 K, the curves overlap. At intermediate temperatures however, two distinct branches are observed: a low-dissipation branch, traced out by the red data points (belonging to the first two temperature sweeps, including the measurement from Fig. 7.4a), and a high-dissipation branch traced out by the blue data points. The light blue points correspond to measurements taken during cooling down and the red and dark blue points are measurements taken during warming up. The overlap between the measurements in both directions implies that there is no correlation between the dissipation state and the direction of the temperature sweep. Despite the upward shift of the resonance frequency after the first temperature cycle, in all subsequent measurements the  $f_0(T)$  curves are reproducible with only small variations of the order of 1 MHz. This suggests that the effect responsible for the different  $Q$  branches does not influence the mechanical stiffness of the nanodrum and is not correlated to or caused by a change in the resonance frequency. Subsequent measurements indicate that dissipation states in between the red and the blue data points are also accessible, but values of  $Q$  outside of the range defined by the measurements in Fig. 7.4b were not measured.

The trend of decreasing dissipation (increasing  $Q$ ) at lower temperatures is often observed in 2D materials [188, 190, 205] and in MEMS in general [206] and is a subject of ongoing discussion. A proposed explanation for this effect is the increased in-plane tension which is known to lower dissipation by increasing the energy stored per vibrational cycle in nanomechanical structures [187, 204, 207, 208]. However, the different dissipation states of the STO drums between 30 and 165 K is, to our knowledge, a phenomenon that has not been observed in other nanomechanical systems, and is most likely related to the ferroelastic domain structure of the STO. The domain walls are a mechanism of releasing stress and are formed in a random configuration when the STO is cooled below its transition temperature. These domain walls are known to be easily displaced in response to external stimuli such as electric fields [209] and mechanical stress [200]. In turn, the motion of the domain walls has been directly linked to mechanical dissipation [195]. Their mobility, i.e., the extent to which they can contribute to the dissipation, is dependent on temperature and their exact spatial arrangement [194, 195, 210]. Additionally, the (ferroelectric) polarization of domain walls changes with temperature [194], and increased polarization has been linked to increased mobility [195].

The seemingly arbitrary occupancy of the  $Q(T)$  branches suggests that the different states are linked to the (random) spatial distribution of domains and domain walls within the drum. This can influence the dissipation in two ways. First, the exact location of a domain wall and its distance from the centre of the membrane determine the local dynamic load experienced by the wall during an oscillation cycle and hence its displacement. Second, domain walls can intersect [210], with the number of crossing points depending on the number (density) of the domain walls. These crossings can act as pinning sites that hinder their propagation, resulting in “jamming” of the domains [210], effectively reducing the dissipated energy per oscillation cycle. In this framework, the high dissipation state (blue points in Fig. 7.4b) would correspond to a situation with a

high density of domain walls at the edges of the nanodrum, where the concentration of strain is the highest. We propose that the red data points correspond to domain wall arrangements where very few run along the drum's surface and, those that do, form a connected matrix that renders them immobile and lessens their contribution to the mechanical dissipation. At low temperatures the domain walls are further known to exhibit erratic movement [210]. The overlap of all data points below 30 K indicates that in this regime the dissipation is no longer dependent on the spatial arrangement of the domain walls in the intermediate temperature range. A curious consequence of this is the large spread of the quality factor as a function of time at 5 K, compared to that at higher temperatures, regardless of the dissipation state the resonator occupies. This is shown in Fig. 7.4c, where the quality factor at the points indicated in Fig. 7.4b is plotted over the course of 100 minutes.

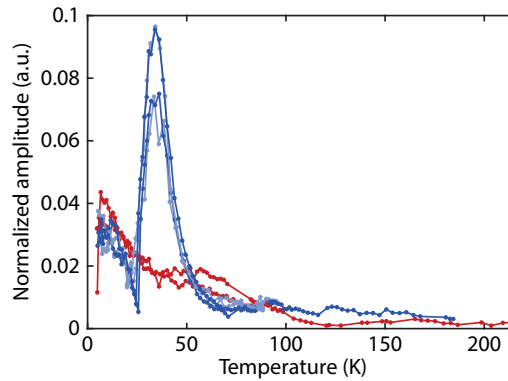


Figure 7.5: **Normalized amplitude at resonance.** The  $y$ -axis shows the resonance peak amplitude divided by the dc voltage on the photodiode to compensate for changes in the reflectivity of the sample. The blue and red points correspond to the data from Fig. 7.4b.

Finally we discuss the measured amplitude at resonance ( $A$ ), presented in Fig. 7.5. The amplitude decreases with increasing temperature, which can be explained by the significant decrease in the quality factor (see Fig. 7.4b) as  $|A|_{\omega=\omega_0} = FQ/(\omega_0^2 m)$ , where  $F$  is the driving force,  $\omega_0$  is the natural frequency and  $m$  is the effective mass of the resonator. Interestingly, the measurement points that belong to the high-dissipation branch (blue points in Figs. 7.4b and 7.5) exhibit a large peak at around 34 K. This is counterintuitive, as one would expect that a lower quality factor should result in a lower amplitude. The only cause of this could be an increase in the actuation efficiency that compensates for the decrease in the  $Q$  factor. If so, this phenomenon cannot be caused by a change in the absorption of STO (at  $\lambda = 405$  nm), which is constant as a function of temperature in the measured range [211]. Therefore, we attribute the increased driving efficiency to a change in the thermal properties of the material. The Debye term ( $C_p/T^3$ , where  $C_p$  is the specific heat of the material), which is also closely related to the thermal expansion of the material ( $\alpha$ ) [212], was found to display a peak around 30 K in STO [213]. The temperature at which  $C_p/T^3$  peaks [213] is consistent with the position of the amplitude peak in our measurements (blue curve in Fig. 7.5), signaling that the change in

the thermal properties is likely responsible for the increase in actuation efficiency. The absence of the peak in the measurements belonging to the other dissipation branches is, nevertheless, challenging to explain within the proposed interpretation, as it would imply that the aforementioned change in the thermal properties of the STO is inhomogeneous and is strongly enhanced at twin boundaries between different domains.

## 7.4. CONCLUSIONS

In conclusion, we demonstrated the fabrication of ultrathin mechanical resonators made of epitaxially grown STO and SRO films. Using laser interferometry, we mechanically characterized the nanodrums and showed that they can be used as nanomechanical devices, much like drums made of van der Waals materials [184, 185, 187, 190, 214, 215]. We show that phase transitions affect the temperature-dependent dynamics of the resonators and that their mechanical dissipation can shed light on the microscopic loss mechanisms, which are often coupled to electronic degrees of freedom.

This work provides novel opportunities for two fields: (i) the field of complex oxides will benefit from a new tool to probe their mechanical properties, which are often strongly coupled to their structural and electronic order parameters; (ii) the field of nanomechanics will now have access to a class of atomically-engineerable materials and heterostructures with exotic properties that could be used as functional elements in nanoelectromechanical systems (NEMS). Such nanomechanical resonators can be used in self-transducing mechanical devices, suspended Bragg reflectors, bimorphic actuators and novel thermomechanical and piezoelectric sensing concepts. Furthermore, by decoupling the high-temperature growth of the materials from the device fabrication flow, these complex oxide NEMS can be easily integrated into fully functional complementary metal oxide semiconductor (CMOS) devices, that cannot tolerate temperatures above 400°C.

## 7.5. METHODS

SAO, STO, and SRO films were grown by PLD on TiO<sub>2</sub>-terminated STO(001) substrates. The pulses were supplied by a KrF excimer laser and the substrate was mounted using two clamps and heated by an infrared laser. SAO and STO were deposited using a laser fluence of 1.2 J/cm<sup>2</sup>, a substrate temperature of 850°C and an oxygen pressure of 10<sup>-6</sup> mbar. SRO was deposited at 600°C, with a fluence of 1.1 J/cm<sup>2</sup> and an oxygen pressure of 0.1 mbar. The growth occurred in layer-by-layer mode for SAO and STO, while SRO grew in step-flow mode. After the deposition, the heterostructures were annealed for one hour at 600°C in 300 mbar O<sub>2</sub>, and cooled down in the same atmosphere at a rate of 20°C/min.

The thin films were detached from the substrate by adhering a PDMS layer to the film surface and immersing the stack in water. Dissolution of a 50 nm SAO layer was found to take approximately 60 minutes. After releasing the substrate, the PDMS layer with the thin film was dried using dry N<sub>2</sub>. The STO and SRO films were transferred onto pre-patterned Si/285 nm SiO<sub>2</sub> substrates using an all-dry deterministic transfer technique [183]. The crystallinity of the thin films before and after their release was investigated by XRD (see Figs. 7.1b and 7.6c).

The SHG measurements were performed in reflection geometry to confirm the presence of the structural transition observed in the mechanical experiments. The sample was excited by a 60 fs laser pulse at a central wavelength of 800 nm from a regenerative Ti:Sapphire amplified laser system operating at a 1 kHz repetition rate. The laser fluence was in the order of  $10 \text{ mJ}/\text{cm}^2$ . The nonlinear response at the central wavelength of 400 nm was detected using a photomultiplier tube.

## 7.6. SUPPLEMENTARY INFORMATION

### 7.6.1. GROWTH & CHARACTERIZATION OF FREESTANDING FILMS

Figure 7.6a shows RHEED oscillations during the growth of a 19 u.c. SAO film on an STO(001) substrate. An AFM measurement of the SAO surface (Fig. 7.6b) is taken directly after the sample is removed from the vacuum chamber. Clear steps and terraces are visible, indicating that the film grows in layer-by-layer mode. An XRD measurement of an SRO/SAO/STO heterostructure is shown in Fig. 7.6c. The simulation of the diffracted intensity (red line, simulated with InteractiveXRDFit [16]) can capture both the peak position and finite size oscillations of the SAO layer and the ultrathin (9 u.c.) SRO film.

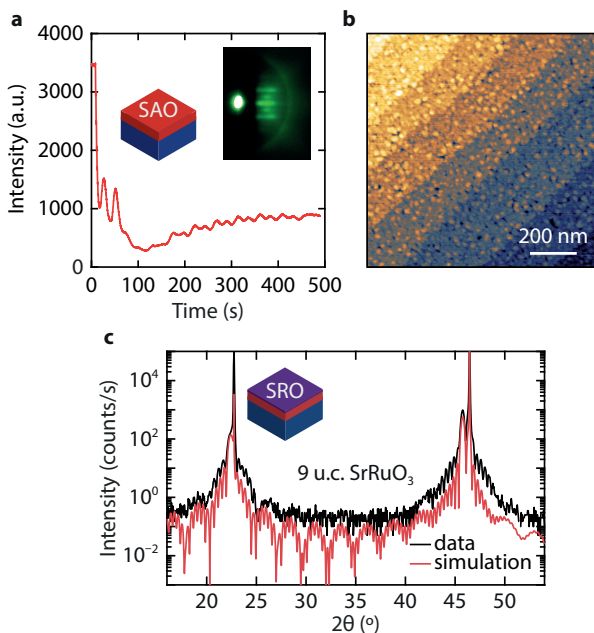


Figure 7.6: **Growth and characterization of freestanding films.** (a) RHEED oscillations during the growth of 19 u.c. SAO on STO. Inset: RHEED diffraction pattern of the SAO surface. (b) AFM topographic image of the SAO surface. (c) XRD measurement of an SRO/SAO/STO heterostructure.

### 7.6.2. SHG STUDY OF FREESTANDING STO

SHG is a nonlinear optical technique based on conversion of two photons of frequency  $f$  to a single photon of frequency  $2f$ . SHG has been proven to be efficient in probing microscopic transformations of the crystal symmetry near structural phase transitions. The polarization and intensity of the SHG light can be substantially affected when the crystal structure undergoes a transition between symmetry groups.

SHG measurements were performed on a 20 nm thick STO film lying on a Si/SiO<sub>2</sub> substrate. The measurement area was equal to the laser spot size, which is estimated to be around 100  $\mu\text{m}$ . The polarization of the incoming light wave was controlled by means of a Glan–Taylor polarizer and a half-wave plate mounted in the rotation stage. The residual SHG signal from the optical components was filtered out using a low-pass filter. The polarization of the reflected light was analyzed with a Glan–Taylor polarizer mounted in the rotational stage. The narrow band (10 nm) at the central filter was used to filter out light at the fundamental wavelength of 800 nm. The polarization of the incident light ( $P_{\text{in}}$ ) is the same as the polarization of the recorded SHG signal ( $P_{\text{out}}$ ). The measurements were taken during cooling down (dark blue curve in Fig. 7.7) and during warming up (light blue curve). The measurements show features at 105 and 157 K, which correspond to the transition temperatures of STO bulk and the STO surface, respectively.

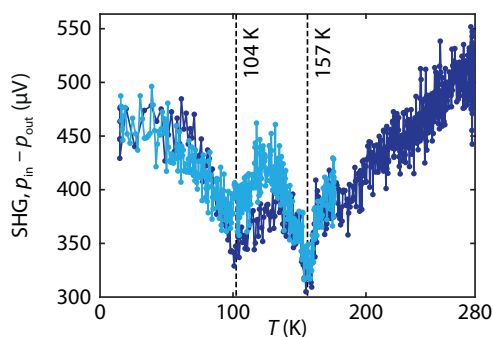


Figure 7.7: **SHG signal from freestanding STO.** SHG signal measured using a  $P_{\text{in}} - P_{\text{out}}$  beam configuration taken while warming up (light blue) and cooling down (dark blue).



# 8

## CONCLUSIONS AND PERSPECTIVES

*So long, and thanks for all the fish.*

Douglas Adams, The Hitchhiker's Guide to the Galaxy

*The results presented in this thesis are important for our fundamental understanding and for advances in future transition metal oxide-based applications. In this chapter, we will review the insights gained and outline promising future directions.*

**S**TRONTIUM iridates have produced a number of surprises over the past few decades, starting with the discovery of an  $J_{\text{eff}} = 1/2$  Mott insulating state in  $\text{Sr}_2\text{IrO}_4$ . While band theory predicted a metallic state owing to the extended nature of  $5d$  orbitals,  $\text{Sr}_2\text{IrO}_4$  was found to be insulating due to the formation of narrow, spin-orbit coupled bands, which are gapped by a relatively small  $U$ . In Chapters 2 to 5 we have seen that the 3D member SIO is no less exciting, displaying unusual electronic and magnetic properties arising from the combination of strong SOC and electronic correlations. We have ventured past seemingly conflicting Hall and thermoelectric measurements (Chapter 3), an enhancement of spin fluctuations in the 2D limit (Chapter 4), and a field-induced magnetic state at low temperatures (Chapter 5).

The properties of SIO are even more intriguing when used to form epitaxial interfaces with other TMOs. Although this avenue is still relatively unexplored, several recent publications have reported emergent magnetism [142], easy-axis reorientation [143], spin-glass-like behavior [44] and the formation of skyrmion spin textures [43] in heterostructures and superlattices involving SIO.

### 8.1. SPIN AND CHARGE ACCUMULATION AT OXIDE INTERFACES

In Chapter 6 we studied STO/SRO/SIO heterostructures, in which the strong SOC of SIO was reported to give rise to skyrmions [43–45]. We uncovered that its unconventional AHE can be explained without resorting to skyrmions, as the behavior can be fully accounted for by considering two AH channels with opposite signs. We showed that these channels arise from the imposition of asymmetric boundary conditions on the SRO film. Preliminary experiments on STO/SRO/LAO heterostructures, presented in Fig. 8.1, show that strong SOC is not required to observe such characteristics.

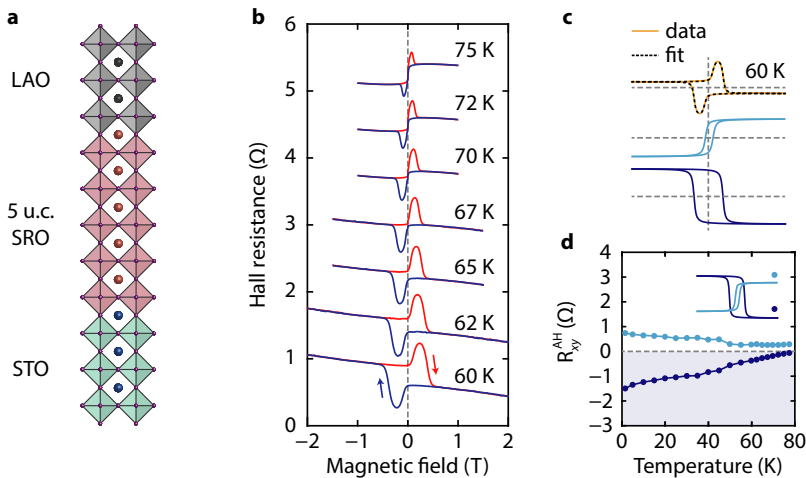


Figure 8.1: **AHE in STO/SRO/LAO heterostructures.** (a) Schematic of the heterostructure. (b) Hall resistance measured at different temperatures. The curves are offset vertically. (c) AHE at 60 K after subtraction of the ordinary Hall component. The dashed line is a fit to the data. The individual AH components are shown below. (d)  $R_{xy}^{\text{AH}}$  (half the height of the hysteresis loop) of the fitted AH components versus temperature.

In fact, since LAO and SRO are more different than SIO and SRO (orthorhombic vs. rhombohedral symmetry, different strain states, weak SOC and no  $d$  orbitals), the asymmetry is larger and the two AH channels can be discerned in a much wider range of temperatures. Several papers have since reported on skyrmion-induced topological Hall effects in uncapped SRO films [46], SRO/BaTiO<sub>3</sub> heterostructures [47], and in protonated SRO films [48]. Other scenarios have been put forward to explain the peaks superimposed on the AHE such as the presence of Ru vacancies [155] and inhomogeneous magnetoelectric properties [216] in uncapped SRO, and noncollinear magnetism induced by antiferromagnetic interfacial coupling in SRO/LSMO heterostructures [217]. However, to date our interpretation is the only one that is able to account for the magnetic field-dependence of the Hall effect, showing that it can be described by the superposition of two anomalous Hall effects of opposite sign. We believe that this field of research is still in its infancy and hope that our interpretation will inspire more studies into the manipulation of Berry phases at oxide interfaces.

## 8.2. BERRY PHASE ENGINEERING IN FREESTANDING OXIDES

In epitaxial form, the Berry curvature of SRO can be manipulated by (i) changing the materials at the top and bottom interfaces, (ii) varying the SRO layer thickness and (iii) designing superlattices. The methods developed in Chapter 7 can be used to greatly expand the array of possibilities for engineering the Berry curvature by manipulating freestanding SRO layers. Examples include:

- forming van der Waals interfaces between SRO and other (2D) materials to trigger different electronic and magnetic reconstructions;
- suspending SRO films and dynamically tuning their strain by field-effect, indentation with an AFM tip or bending a flexible substrate;
- forming interfaces between freestanding SRO and other TMOs, thereby controlling their alignment to form moiré patterns as in recent work on magic-angle graphene bilayers [218].

As a first step towards the realization of such devices, we performed preliminary experiments on freestanding SRO films transferred onto Si/SiO<sub>2</sub> and STO substrates. In particular, we focused on the modification of the conducting and ferromagnetic properties stemming from strain relaxation and the release process. An overview of the magnetotransport results is shown in Fig. 8.2. Surprisingly, we found that freestanding SRO films display two-phase magnetic behavior, qualitatively similar to our measurements on STO/SRO/SIO and STO/SRO/LAO heterostructures and SRO bilayers. The individual AH components are of opposite sign in the entire temperature range, but perhaps the most remarkable feature is the difference in switching mechanisms. Whereas the magnetization of one channel (negative AH component, dark blue curve) switches very abruptly, the magnetization of the other channel (positive AH component, light blue curve) switches gradually (see Fig. 8.2d). Further studies are required to investigate whether this originates from interfacial effects or from a structural or chemical gradient within the SRO film.

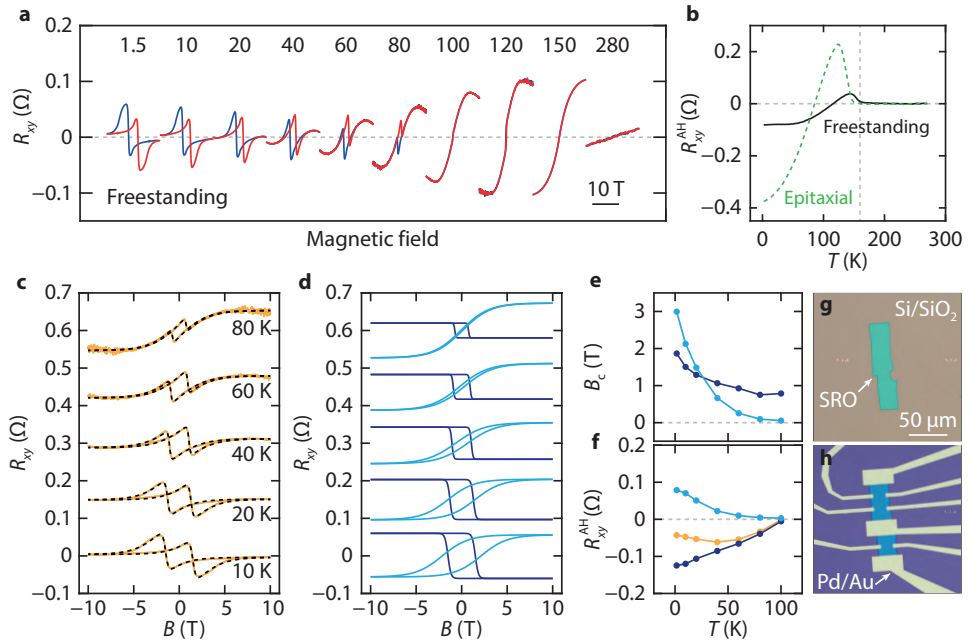


Figure 8.2: **Anomalous Hall effect in freestanding SRO films.** (a) Hall effect of a 75 u.c. SRO film measured at different temperatures. The curves are offset horizontally. (b) Temperature evolution of  $R_{xy}^{AH}$ . (c) Hall resistance measured at different temperatures. The black dashed lines are fits to the data and the curves are offset vertically. (d) Individual anomalous Hall components. (e) and (f) show the temperature evolution of the coercive fields and  $R_{xy}^{AH}$ , respectively. (g) and (h) show optical images of an SRO flake before and after fabrication.

### 8.3. FUNCTIONAL OXIDE RESONATORS AND SUPERCAPACITORS

For the complex oxide mechanical resonators, properties such as ferroelectricity or ferromagnetism could be used to obtain self-transducing devices, sensitive potentiometers or magnetometers (see Fig. 8.3a). Furthermore, the high dielectric constant of STO and other TMOs can be used to realize supercapacitors (see Fig. 8.3b).

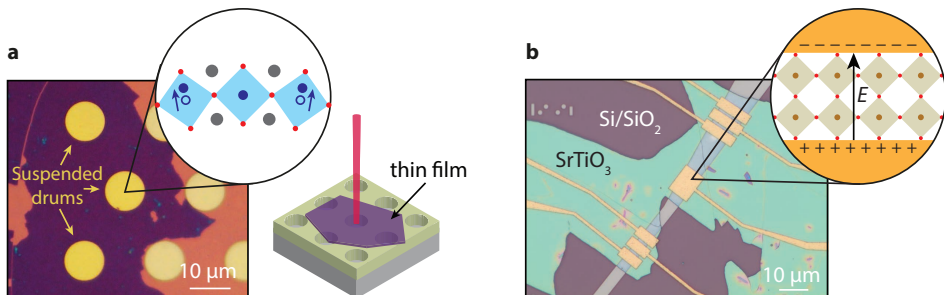


Figure 8.3: **Novel devices based on freestanding oxides.** (a) Complex oxide mechanical resonators. (b) Supercapacitor formed by sandwiching an STO film between gold electrodes.

# REFERENCES

- [1] P. Zubko, S. Gariglio, M. Gabay, P. Ghosez, and J.-M. Triscone, *Interface physics in complex oxide heterostructures*, [Annual Review of Condensed Matter Physics](#) **2**, 141 (2011).
- [2] Y. Tokura and N. Nagaosa, *Orbital physics in transition-metal oxides*, [Science](#) **288**, 462 (2000).
- [3] M. L. Medarde, *Structural, magnetic and electronic properties of RNiO<sub>3</sub> perovskites (R = rare earth)*, [Journal of Physics: Condensed Matter](#) **9**, 1679 (1997).
- [4] J. G. Bednorz and K. A. Müller, *Possible high T<sub>c</sub> superconductivity in the Ba-La-Cu-O system*, [Zeitschrift für Physik B Condensed Matter](#) **64**, 189 (1986).
- [5] S. Carter, T. Rosenbaum, J. Honig, and J. Spalek, *New phase boundary in highly correlated, barely metallic V<sub>2</sub>O<sub>3</sub>*, [Physical Review Letters](#) **67**, 3440 (1991).
- [6] Y. Tokura, Y. Taguchi, Y. Okada, Y. Fujishima, T. Arima, K. Kumagai, and Y. Iye, *Filling dependence of electronic properties on the verge of metal–Mott-insulator transition in Sr<sub>1-x</sub>La<sub>x</sub>TiO<sub>3</sub>*, [Physical Review Letters](#) **70**, 2126 (1993).
- [7] S. Wolf, D. Awschalom, R. Buhrman, J. Daughton, S. Von Molnar, M. Roukes, A. Y. Chtchelkanova, and D. Treger, *Spintronics: a spin-based electronics vision for the future*, [Science](#) **294**, 1488 (2001).
- [8] A. Manchon, H. C. Koo, J. Nitta, S. Frolov, and R. Duine, *New perspectives for Rashba spin–orbit coupling*, [Nature Materials](#) **14**, 871 (2015).
- [9] N. Ashcroft and N. Mermin, *Solid State Physics* (Saunders College, Philadelphia, 1976).
- [10] C. Kittel, *Introduction to Solid State Physics*, 6th ed. (John Wiley & Sons, Inc., New York, 1986).
- [11] G. Koster, L. Klein, W. Siemons, G. Rijnders, J. S. Dodge, C.-B. Eom, D. H. Blank, and M. R. Beasley, *Structure, physical properties, and applications of SrRuO<sub>3</sub> thin films*, [Reviews of Modern Physics](#) **84**, 253 (2012).
- [12] O. Schirmer, A. Forster, H. Hesse, M. Wohlecke, and S. Kapphan, *Paramagnetic resonance and near-infrared optical absorption of SrTiO<sub>3</sub>: Ir<sup>4+</sup>*, [Journal of Physics C: Solid State Physics](#) **17**, 1321 (1984).
- [13] R. Eason, *Pulsed laser deposition of thin films: applications-led growth of functional materials* (John Wiley & Sons, 2007).
- [14] M. Kawasaki, K. Takahashi, T. Maeda, R. Tsuchiya, M. Shinohara, O. Ishiyama, T. Yonezawa, M. Yoshimoto, and H. Koinuma, *Atomic control of the SrTiO<sub>3</sub> crystal surface*, [Science](#) **266**, 1540 (1994).
- [15] G. Koster, B. L. Kropman, G. J. Rijnders, D. H. Blank, and H. Rogalla, *Quasi-ideal strontium titanate crystal surfaces through formation of strontium hydroxide*, [Applied Physics Letters](#) **73**, 2920 (1998).
- [16] C. Lichtensteiger, *InteractiveXRDFit: a new tool to simulate and fit X-ray diffractograms of oxide thin films and heterostructures*, [Journal of Applied Crystallography](#) **51** (2018).
- [17] G. Jackeli and G. Khaliullin, *Mott insulators in the strong spin–orbit coupling limit: from Heisenberg to a quantum compass and Kitaev models*, [Physical Review Letters](#) **102**, 017205 (2009).
- [18] B. Kim, H. Jin, S. Moon, J.-Y. Kim, B.-G. Park, C. Leem, J. Yu, T. Noh, C. Kim, S.-J. Oh, *et al.*, *Novel J<sub>eff</sub> = 1/2 Mott state induced by relativistic spin–orbit coupling in Sr<sub>2</sub>IrO<sub>4</sub>*, [Physical Review Letters](#) **101**, 076402 (2008).
- [19] S. Moon, H. Jin, K. W. Kim, W. Choi, Y. Lee, J. Yu, G. Cao, A. Sumi, H. Funakubo, C. Bernhard, *et al.*, *Dimensionality-controlled insulator–metal transition and correlated metallic state in 5d transition metal oxides Sr<sub>n+1</sub>Ir<sub>n</sub>O<sub>3n+1</sub> (n = 1, 2, and ∞)*, [Physical Review Letters](#) **101**, 226402 (2008).
- [20] J. K. Kawasaki, M. Uchida, H. Paik, D. G. Schlom, and K. M. Shen, *Evolution of electronic correlations*

- across the rutile, perovskite, and Ruddelsden–Popper iridates with octahedral connectivity, *Physical Review B* **94**, 121104 (2016).
- [21] G. Cao, J. Bolivar, S. McCall, J. Crow, and R. Guertin, *Weak ferromagnetism, metal-to-nonmetal transition, and negative differential resistivity in single-crystal  $\text{Sr}_2\text{IrO}_4$* , *Physical Review B* **57**, R11039 (1998).
- [22] S. Boseggia, H. Walker, J. Vale, R. Springell, Z. Feng, R. Perry, M. M. Sala, H. M. Rønnow, S. Collins, and D. F. McMorrow, *Locking of iridium magnetic moments to the correlated rotation of oxygen octahedra in  $\text{Sr}_2\text{IrO}_4$  revealed by X-ray resonant scattering*, *Journal of Physics: Condensed Matter* **25**, 422202 (2013).
- [23] Y. Nie, P. King, C. Kim, M. Uchida, H. Wei, B. Faeth, J. Ruf, J. Ruff, L. Xie, X. Pan, *et al.*, *Interplay of spin–orbit interactions, dimensionality, and octahedral rotations in semimetallic  $\text{SrIrO}_3$* , *Physical Review Letters* **114**, 016401 (2015).
- [24] Z. Liu, M. Li, Q. Li, J. Liu, W. Li, H. Yang, Q. Yao, C. Fan, X. Wan, Z. Wang, *et al.*, *Direct observation of the Dirac nodes lifting in semimetallic perovskite  $\text{SrIrO}_3$  thin films*, *Scientific Reports* **6**, 30309 (2016).
- [25] M. A. Zeb and H.-Y. Kee, *Interplay between spin–orbit coupling and Hubbard interaction in  $\text{SrIrO}_3$  and related  $\text{Pbnm}$  perovskite oxides*, *Physical Review B* **86**, 085149 (2012).
- [26] J.-M. Carter, V. V. Shankar, M. A. Zeb, and H.-Y. Kee, *Semimetal and topological insulator in perovskite iridates*, *Physical Review B* **85**, 115105 (2012).
- [27] G. Cao, V. Durairaj, S. Chikara, L. DeLong, S. Parkin, and P. Schlottmann, *Non-Fermi-liquid behavior in nearly ferromagnetic  $\text{SrIrO}_3$  single crystals*, *Physical Review B* **76**, 100402 (2007).
- [28] J. Liu, D. Krieger, L. Horak, D. Puggioni, C. R. Serrao, R. Chen, D. Yi, C. Frontera, V. Holy, A. Vishwanath, *et al.*, *Strain-induced nonsymmorphic symmetry breaking and removal of Dirac semimetallic nodal line in an orthoperovskite iridate*, *Physical Review B* **93**, 085118 (2016).
- [29] T. Rice and M. Sigrist,  *$\text{Sr}_2\text{RuO}_4$ : an electronic analogue of  $3\text{He}$ ?* *Journal of Physics: Condensed Matter* **7**, L643 (1995).
- [30] K. Nelson, Z. Mao, Y. Maeno, and Y. Liu, *Odd-parity superconductivity in  $\text{Sr}_2\text{RuO}_4$* , *Science* **306**, 1151 (2004).
- [31] L. Klein, J. Dodge, C. Ahn, J. Reiner, L. Mieville, T. Geballe, M. Beasley, and A. Kapitulnik, *Transport and magnetization in the badly metallic itinerant ferromagnet  $\text{SrRuO}_3$* , *Journal of Physics: Condensed Matter* **8**, 10111 (1996).
- [32] S. Gausepohl, M. Lee, R. Rao, and C. Eom, *Hall-effect sign reversal in  $\text{CaRuO}_3$  and  $\text{SrRuO}_3$  thin films*, *Physical Review B* **54**, 8996 (1996).
- [33] L. Klein, J. Reiner, T. Geballe, M. Beasley, and A. Kapitulnik, *Extraordinary Hall effect in  $\text{SrRuO}_3$* , *Physical Review B* **61**, R7842 (2000).
- [34] Z. Fang, N. Nagaosa, K. S. Takahashi, A. Asamitsu, R. Mathieu, T. Ogasawara, H. Yamada, M. Kawasaki, Y. Tokura, and K. Terakura, *The anomalous Hall effect and magnetic monopoles in momentum space*, *Science* **302**, 92 (2003).
- [35] M. V. Berry, *Quantal phase factors accompanying adiabatic changes*, *Proceedings of the Royal Society of London A* **392**, 45 (1984).
- [36] J. Inoue and H. Ohno, *Taking the Hall effect for a spin*, *Science* **309**, 2004 (2005).
- [37] A. Fert, N. Reyren, and V. Cros, *Magnetic skyrmions: advances in physics and potential applications*, *Nature Reviews Materials* **2**, 17031 (2017).
- [38] N. Nagaosa, J. Sinova, S. Onoda, A. MacDonald, and N. Ong, *Anomalous Hall effect*, *Reviews of Modern Physics* **82**, 1539 (2010).
- [39] J. Smit, *The spontaneous Hall effect in ferromagnetics II*, *Physica* **24**, 39 (1958).
- [40] L. Berger, *Side-jump mechanism for the Hall effect of ferromagnets*, *Physical Review B* **2**, 4559 (1970).
- [41] R. Karplus and J. Luttinger, *Hall effect in ferromagnetics*, *Physical Review* **95**, 1154 (1954).

- [42] D. Xiao, M.-C. Chang, and Q. Niu, *Berry phase effects on electronic properties*, *Reviews of Modern Physics* **82**, 1959 (2010).
- [43] J. Matsuno, N. Ogawa, K. Yasuda, F. Kagawa, W. Koshibae, N. Nagaosa, Y. Tokura, and M. Kawasaki, *Interface-driven topological Hall effect in SrRuO<sub>3</sub>-SrIrO<sub>3</sub> bilayer*, *Science Advances* **2**, e1600304 (2016).
- [44] B. Pang, L. Zhang, Y. Chen, J. Zhou, S. Yao, S. Zhang, and Y. Chen, *Spin-glass-like behavior and topological Hall effect in SrRuO<sub>3</sub>/SrIrO<sub>3</sub> superlattices for oxide spintronics applications*, *ACS Applied Materials & Interfaces* **9**, 3201 (2017).
- [45] Y. Ohuchi, J. Matsuno, N. Ogawa, Y. Kozuka, M. Uchida, Y. Tokura, and M. Kawasaki, *Electric-field control of anomalous and topological Hall effects in oxide bilayer thin films*, *Nature Communications* **9**, 213 (2018).
- [46] Y. Gu, Y.-W. Wei, K. Xu, H. Zhang, F. Wang, F. Li, M. S. Saleem, C.-Z. Chang, J. Sun, C. Song, *et al.*, *Oxygen-octahedral-tilting-driven topological Hall effect in ultrathin SrRuO<sub>3</sub> films*, arXiv preprint arXiv:1811.09075 (2018).
- [47] L. Wang, Q. Feng, Y. Kim, R. Kim, K. H. Lee, S. D. Pollard, Y. J. Shin, H. Zhou, W. Peng, D. Lee, *et al.*, *Ferroelectrically tunable magnetic skyrmions in ultrathin oxide heterostructures*, *Nature Materials*, **1** (2018).
- [48] Z. Li, S. Shen, Z. Tian, K. Hwangbo, M. Wang, Y. Wang, F. M. Bartram, L. He, Y. Lyu, Y. Dong, *et al.*, *Electric-field control of magnetism with emergent topological Hall effect in SrRuO<sub>3</sub> through proton evolution*, arXiv preprint arXiv:1811.10794 (2018).
- [49] D. J. Groenendijk, N. Manca, G. Mattoni, L. Kootstra, S. Gariglio, Y. Huang, E. van Heumen, and A. D. Caviglia, *Epitaxial growth and thermodynamic stability of SrIrO<sub>3</sub>/SrTiO<sub>3</sub> heterostructures*, *Applied Physics Letters* **109**, 041906 (2016).
- [50] B. Kim, H. Ohsumi, T. Komesu, S. Sakai, T. Morita, H. Takagi, and T. Arima, *Phase-sensitive observation of a spin-orbital Mott state in Sr<sub>2</sub>IrO<sub>4</sub>*, *Science* **323**, 1329 (2009).
- [51] D. Xiao, W. Zhu, Y. Ran, N. Nagaosa, and S. Okamoto, *Interface engineering of quantum Hall effects in digital transition metal oxide heterostructures*, *Nature Communications* **2**, 596 (2011).
- [52] Y. Chen, Y.-M. Lu, and H.-Y. Kee, *Topological crystalline metal in orthorhombic perovskite iridates*, *Nature Communications* **6** (2015).
- [53] Y. Chen, H.-S. Kim, and H.-Y. Kee, *Topological crystalline semimetals in nonsymmorphic lattices*, *Physical Review B* **93**, 155140 (2016).
- [54] C. Fang, L. Lu, J. Liu, and L. Fu, *Topological semimetals with helicoid surface states*, *Nature Physics* **12**, 936 (2016).
- [55] J. Longo, J. Kafalas, and R. Arnott, *Structure and properties of the high and low pressure forms of SrIrO<sub>3</sub>*, *Journal of Solid State Chemistry* **3**, 174 (1971).
- [56] Y. Tian, Y. Gong, Z. Li, F. Jiang, and H. Jin, *Synthetic process and spark plasma sintering of SrIrO<sub>3</sub> composite oxide*, *Journal of Advanced Ceramics* **2**, 347 (2013).
- [57] Y. K. Kim, A. Sumi, K. Takahashi, S. Yokoyama, S. Ito, T. Watanabe, K. Akiyama, S. Kaneko, K. Saito, and H. Funakubo, *Metalorganic chemical vapor deposition of epitaxial perovskite SrIrO<sub>3</sub> films on (100)SrTiO<sub>3</sub> substrates*, *Japanese Journal of Applied Physics* **45**, L36 (2005).
- [58] S. Y. Jang, S. J. Moon, B. C. Jeon, and J.-S. Chung, *PLD growth of epitaxially-stabilized 5d perovskite SrIrO<sub>3</sub> thin films*, *Journal of the Korean Physical Society* **56**, 1814 (2010).
- [59] J. H. Gruenewald, J. Nichols, J. Terzic, G. Cao, J. W. Brill, and S. S. A. Seo, *Compressive strain-induced metal-insulator transition in orthorhombic SrIrO<sub>3</sub> thin films*, *Journal of Materials Research* **29**, 2491 (2014).
- [60] J. Matsuno, K. Ihara, S. Yamamura, H. Wadati, K. Ishii, V. V. Shankar, H.-Y. Kee, and H. Takagi, *Engineering a spin-orbital magnetic insulator by tailoring superlattices*, *Physical Review Letters* **114**, 247209 (2015).
- [61] L. Zhang, Q. Liang, Y. Xiong, B. Zhang, L. Gao, H. Li, Y. Chen, J. Zhou, S.-T. Zhang, Z.-B. Gu, *et al.*, *Tunable semimetallic state in compressive-strained SrIrO<sub>3</sub> films revealed by transport behavior*, *Physical Review B*

- 91**, 035110 (2015).
- [62] A. Biswas, K.-S. Kim, and Y. H. Jeong, *Metal–insulator transitions in perovskite SrIrO<sub>3</sub> thin films*, *Journal of Applied Physics* **116**, 213704 (2014).
- [63] K. Nishio, H. Y. Hwang, and Y. Hikita, *Thermodynamic guiding principles in selective synthesis of strontium iridate Ruddlesden–Popper epitaxial films*, *APL Materials* **4**, 036102 (2016).
- [64] S. Amoruso, A. Sambri, and X. Wang, *Propagation dynamics of a LaMnO<sub>3</sub> laser ablation plume in an oxygen atmosphere*, *Journal of Applied Physics* **100**, 013302 (2006).
- [65] L. Zhang, Y. Chen, B. Zhang, J. Zhou, S. Zhang, Z. Gu, S. Yao, and Y. Chen, *Sensitively temperature-dependent spin–orbit coupling in SrIrO<sub>3</sub> thin films*, *Journal of the Physical Society of Japan* **83**, 054707 (2014).
- [66] A. Biswas, K.-S. Kim, and Y. H. Jeong, *Emergence of non-Fermi liquid behaviors in 5d perovskite SrIrO<sub>3</sub> thin films: Interplay between correlation, disorder, and spin–orbit coupling*, *Journal of Magnetism and Magnetic Materials* **400**, 36 (2016).
- [67] M. Sato, Y. Soejima, N. Ohama, A. Okazaki, H. Scheel, and K. Müller, *The lattice constant vs. temperature relation around the 105 K transition of a flux-grown SrTiO<sub>3</sub> crystal*, *Phase Transitions: A Multinational Journal* **5**, 207 (1985).
- [68] R. Loetzsch, A. Lübcke, I. Uschmann, E. Förster, V. Große, M. Thuerk, T. Koettig, F. Schmidl, and P. Seidel, *The cubic to tetragonal phase transition in SrTiO<sub>3</sub> single crystals near its surface under internal and external strains*, *Applied Physics Letters* **96**, 1901 (2010).
- [69] Y. Segal, K. Garrity, C. Vaz, J. Hoffman, F. Walker, S. Ismail-Beigi, and C. Ahn, *Dynamic evanescent phonon coupling across the La<sub>1-x</sub>Sr<sub>x</sub>MnO<sub>3</sub>/SrTiO<sub>3</sub> interface*, *Physical Review Letters* **107**, 105501 (2011).
- [70] S. Foltyn, R. Dye, K. Ott, E. Peterson, K. Hubbard, W. Hutchinson, R. Muenchausen, R. Estler, and X. Wu, *Target modification in the excimer laser deposition of YBa<sub>2</sub>Cu<sub>3</sub>O<sub>7-x</sub> thin films*, *Applied Physics Letters* **59**, 594 (1991).
- [71] S. Wicklein, A. Sambri, S. Amoruso, X. Wang, R. Bruzzese, A. Koehl, and R. Dittmann, *Pulsed laser ablation of complex oxides: The role of congruent ablation and preferential scattering for the film stoichiometry*, *Applied Physics Letters* **101**, 131601 (2012).
- [72] D. Groenendijk and S. Gariglio, *Sequential pulsed laser deposition of homoepitaxial SrTiO<sub>3</sub> thin films*, *Journal of Applied Physics* **120**, 225307 (2016).
- [73] C. Xu, S. Wicklein, A. Sambri, S. Amoruso, M. Moors, and R. Dittmann, *Impact of the interplay between nonstoichiometry and kinetic energy of the plume species on the growth mode of SrTiO<sub>3</sub> thin films*, *Journal of Physics D: Applied Physics* **47**, 034009 (2013).
- [74] N. Manca, D. J. Groenendijk, I. Pallecchi, C. Autieri, L. M. Tang, F. Telesio, G. Mattoni, A. McCollam, S. Piccozzi, and A. D. Caviglia, *Balanced electron–hole transport in spin–orbit semimetal SrIrO<sub>3</sub> heterostructures*, *Physical Review B* **97**, 081105 (2018).
- [75] D. Pesin and L. Balents, *Mott physics and band topology in materials with strong spin–orbit interaction*, *Nature Physics* **6**, 376 (2010).
- [76] M. Kargarian, J. Wen, and G. A. Fiete, *Competing exotic topological insulator phases in transition-metal oxides on the pyrochlore lattice with distortion*, *Physical Review B* **83**, 165112 (2011).
- [77] B.-J. Yang and N. Nagaosa, *Emergent topological phenomena in thin films of pyrochlore iridates*, *Physical Review Letters* **112**, 246402 (2014).
- [78] X. Chen, T. Hogan, D. Walkup, W. Zhou, M. Pokharel, M. Yao, W. Tian, T. Z. Ward, Y. Zhao, D. Parshall, et al., *Influence of electron doping on the ground state of (Sr<sub>1-x</sub>La<sub>x</sub>)<sub>2</sub>IrO<sub>4</sub>*, *Physical Review B* **92**, 075125 (2015).
- [79] F. Wang and T. Senthil, *Twisted Hubbard model for Sr<sub>2</sub>IrO<sub>4</sub>: magnetism and possible high temperature superconductivity*, *Physical Review Letters* **106**, 136402 (2011).
- [80] J. Kim, D. Casa, M. Upton, T. Gog, Y.-J. Kim, J. Mitchell, M. Van Veenendaal, M. Daghofer, J. van

- Den Brink, G. Khaliullin, *et al.*, *Magnetic excitation spectra of  $\text{Sr}_2\text{IrO}_4$  probed by resonant inelastic X-ray scattering: establishing links to cuprate superconductors*, *Physical Review Letters* **108**, 177003 (2012).
- [81] Z. Y. Meng, Y. B. Kim, and H.-Y. Kee, *Odd-parity triplet superconducting phase in multiorbital materials with a strong spin-orbit coupling: application to doped  $\text{Sr}_2\text{IrO}_4$* , *Physical Review Letters* **113**, 177003 (2014).
- [82] J. Fujioka, T. Okawa, A. Yamamoto, and Y. Tokura, *Correlated Dirac semimetallic state with unusual positive magnetoresistance in strain-free perovskite  $\text{SrIrO}_3$* , *Physical Review B* **95**, 121102 (2017).
- [83] L. Horák, D. Kriegner, J. Liu, C. Frontera, X. Marti, and V. Holý, *Structure of epitaxial  $\text{SrIrO}_3$  perovskite studied by interference between X-ray waves diffracted by the substrate and the thin film*, *Journal of Applied Crystallography* **50** (2017).
- [84] D. Groenendijk, C. Autieri, J. Girovsky, M. C. Martinez-Velarte, N. Manca, G. Mattoni, A. Monteiro, N. Gauquelin, J. Verbeeck, A. Otte, *et al.*, *spin-orbit semimetal  $\text{SrIrO}_3$  in the two-dimensional limit*, *Physical Review Letters* **119**, 256403 (2017).
- [85] P. Schütz, D. Di Sante, L. Dudy, J. Gabel, M. Stübinger, M. Kamp, Y. Huang, M. Capone, M.-A. Husanu, V. Strocov, *et al.*, *Dimensionality-driven metal-insulator transition in spin-orbit-coupled  $\text{SrIrO}_3$* , *Physical Review Letters* **119**, 256404 (2017).
- [86] R. Neville, B. Hoeneisen, and C. Mead, *Permittivity of strontium titanate*, *Journal of Applied Physics* **43**, 2124 (1972).
- [87] D. Davidovikj, N. Manca, H. S. van der Zant, A. D. Caviglia, and G. A. Steele, *Quantum paraelectricity probed by superconducting resonators*, *Physical Review B* **95**, 214513 (2017).
- [88] I. Pallecchi, M. Buscaglia, V. Buscaglia, E. Gilioli, G. Lamura, F. Telesio, M. Cimberle, and D. Marré, *Thermoelectric behavior of Ruddlesden-Popper series iridates*, *Journal of Physics: Condensed Matter* **28**, 065601 (2016).
- [89] R. Heikes, R. Miller, and R. Mazelsky, *Magnetic and electrical anomalies in  $\text{LaCoO}_3$* , *Physica* **30**, 1600 (1964).
- [90] M. Jonson and G. Mahan, *Mott's formula for the thermopower and the Wiedemann-Franz law*, *Physical Review B* **21**, 4223 (1980).
- [91] I. Pallecchi, M. Codda, E. G. d'Agliano, D. Marré, A. Caviglia, N. Reyren, S. Gariglio, and J.-M. Triscone, *Seebeck effect in the conducting  $\text{LaAlO}_3/\text{SrTiO}_3$  interface*, *Physical Review B* **81**, 085414 (2010).
- [92] A. Abrikosov, *Quantum magnetoresistance*, *Physical Review B* **58**, 2788 (1998).
- [93] M. Parish and P. Littlewood, *Non-saturating magnetoresistance in heavily disordered semiconductors*, *Nature* **426**, 162 (2003).
- [94] M. M. Parish and P. B. Littlewood, *Classical magnetotransport of inhomogeneous conductors*, *Physical Review B* **72**, 094417 (2005).
- [95] A. Gerber, I. Kishon, I. Y. Korenblit, O. Riss, A. Segal, M. Karpovski, and B. Raquet, *Linear positive magnetoresistance and quantum interference in ferromagnetic metals*, *Physical Review Letters* **99**, 027201 (2007).
- [96] J. Hu and T. Rosenbaum, *Classical and quantum routes to linear magnetoresistance*, *Nature Materials* **7**, 697 (2008).
- [97] K. K. Huynh, Y. Tanabe, and K. Tanigaki, *Both electron and hole Dirac cone states in  $\text{Ba}(\text{FeAs})_2$  confirmed by magnetoresistance*, *Physical Review Letters* **106**, 217004 (2011).
- [98] N. Kozlova, N. Mori, O. Makarovskiy, L. Eaves, Q. Zhuang, A. Krier, and A. Patane, *Linear magnetoresistance due to multiple-electron scattering by low-mobility islands in an inhomogeneous conductor*, *Nature Communications* **3**, 1097 (2012).
- [99] P. Alekseev, A. Dmitriev, I. Gornyi, V. Y. Kachorovskii, B. Narozhny, M. Schütt, and M. Titov, *Magnetoresistance in two-component systems*, *Physical Review Letters* **114**, 156601 (2015).

- [100] G. Kresse and D. Joubert, *From ultrasoft pseudopotentials to the projector augmented-wave method*, *Physical Review B* **59**, 1758 (1999).
- [101] J. P. Perdew, A. Ruzsinszky, G. I. Csonka, O. A. Vydrov, G. E. Scuseria, L. A. Constantin, X. Zhou, and K. Burke, *Restoring the density-gradient expansion for exchange in solids and surfaces*, *Physical Review Letters* **100**, 136406 (2008).
- [102] V. I. Anisimov, J. Zaanen, and O. K. Andersen, *Band theory and Mott insulators: Hubbard  $U$  instead of Stoner  $I$* , *Physical Review B* **44**, 943 (1991).
- [103] A. Liechtenstein, V. Anisimov, and J. Zaanen, *Density-functional theory and strong interactions: Orbital ordering in Mott-Hubbard insulators*, *Physical Review B* **52**, R5467 (1995).
- [104] B. Kim, P. Liu, and C. Franchini, *Dimensionality–strain phase diagram of strontium iridates*, *Physical Review B* **95**, 115111 (2017).
- [105] P. E. Blöchl, *Projector augmented-wave method*, *Physical Review B* **50**, 17953 (1994).
- [106] J. D. Pack and H. J. Monkhorst, “*Special points for Brillouin-zone integrations*”—a reply, *Physical Review B* **16**, 1748 (1977).
- [107] K. Yoshimatsu, T. Okabe, H. Kumigashira, S. Okamoto, S. Aizaki, A. Fujimori, and M. Oshima, *Dimensional-crossover-driven metal–insulator transition in  $SrVO_3$  ultrathin films*, *Physical Review Letters* **104**, 147601 (2010).
- [108] J. Hubbard, *Electron correlations in narrow energy bands*, *Proceedings of the Royal Society of London A: Mathematical, Physical and Engineering Sciences* **276**, 238 (1963).
- [109] A. Boris, Y. Matiks, E. Benckiser, A. Frano, P. Popovich, V. Hinkov, P. Wochner, M. Castro-Colin, E. Detempe, V. K. Malik, *et al.*, *Dimensionality control of electronic phase transitions in nickel-oxide superlattices*, *Science* **332**, 937 (2011).
- [110] P. King, H. Wei, Y. Nie, M. Uchida, C. Adamo, S. Zhu, X. He, I. Božović, D. Schlom, and K. Shen, *Atomic-scale control of competing electronic phases in ultrathin  $LaNiO_3$* , *Nature Nanotechnology* **9**, 443 (2014).
- [111] R. Scherwitzl, S. Gariglio, M. Gabay, P. Zubko, M. Gibert, and J.-M. Triscone, *metal–insulator transition in ultrathin  $LaNiO_3$  films*, *Physical Review Letters* **106**, 246403 (2011).
- [112] M. Imada, A. Fujimori, and Y. Tokura, *metal–insulator transitions*, *Reviews of Modern Physics* **70**, 1039 (1998).
- [113] K.-H. Kim, H.-S. Kim, and M. J. Han, *Electronic structure and magnetic properties of iridate superlattice  $SrIrO_3/SrTiO_3$* , *Journal of Physics: Condensed Matter* **26**, 185501 (2014).
- [114] S. Y. Kim, C. H. Kim, L. Sandilands, C. Sohn, J. Matsuno, H. Takagi, K. Kim, Y. Lee, S. Moon, and T. Noh, *Manipulation of electronic structure via alteration of local orbital environment in  $[(SrIrO_3)_m,(SrTiO_3)]_{(m=1,2, \text{ and } \infty)}$  superlattices*, *Physical Review B* **94**, 245113 (2016).
- [115] L. Hao, D. Meyers, C. Frederick, G. Fabbris, J. Yang, N. Traynor, L. Horak, D. Krieger, Y. Choi, J.-W. Kim, *et al.*, *Two-dimensional  $J_{\text{eff}} = 1/2$  antiferromagnetic insulator unraveled from interlayer exchange coupling in artificial perovskite iridate superlattices*, *Physical Review Letters* **119**, 027204 (2017).
- [116] D. Meyers, Y. Cao, G. Fabbris, N. J. Robinson, L. Hao, C. Frederick, N. Traynor, J. Yang, J. Lin, M. Upton, *et al.*, *Magnetism in artificial Ruddlesden–Popper iridates leveraged by structural distortions*, *arXiv preprint arXiv:1707.08910* (2017).
- [117] D. Licciardello and D. Thouless, *Constancy of minimum metallic conductivity in two dimensions*, *Physical Review Letters* **35**, 1475 (1975).
- [118] W. Brenig, G. Döhler, and H. Heyszenau, *Hopping conductivity in highly anisotropic systems*, *Philosophical Magazine* **27**, 1093 (1973).
- [119] R. Rosenbaum, *Crossover from Mott to Efros–Shklovskii variable-range-hopping conductivity in  $In_xO_y$  films*, *Physical Review B* **44**, 3599 (1991).
- [120] S. Hurand, A. Jouan, C. Feuillet-Palma, G. Singh, J. Biscaras, E. Lesne, N. Reyren, A. Barthélémy, M. Bibes,

- J. Villegas, *et al.*, *Field-effect control of superconductivity and Rashba spin-orbit coupling in top-gated LaAlO<sub>3</sub>/SrTiO<sub>3</sub> devices*, *Scientific Reports* **5**, 12751 (2015).
- [121] S. Maekawa and H. Fukuyama, *Magneto-resistance in two-dimensional disordered systems: effects of Zeeman splitting and spin-orbit scattering*, *Journal of the Physical Society of Japan* **50**, 2516 (1981).
- [122] C. Walhout, A. Acun, L. Zhang, M. Ezawa, and H. J. Zandvliet, *Scanning tunneling spectroscopy study of the Dirac spectrum of germanene*, *Journal of Physics: Condensed Matter* **28**, 284006 (2016).
- [123] Y. J. Song, A. F. Otte, Y. Kuk, Y. Hu, D. B. Torrance, P. N. First, W. A. de Heer, H. Min, S. Adam, M. D. Stiles, *et al.*, *High-resolution tunnelling spectroscopy of a graphene quartet*, *Nature* **467**, 185 (2010).
- [124] Y. Kohsaka, K. Iwaya, S. Satow, T. Hanaguri, M. Azuma, M. Takano, and H. Takagi, *Imaging nanoscale electronic inhomogeneity in the lightly doped Mott insulator Ca<sub>2-x</sub>Na<sub>x</sub>CuO<sub>2</sub>Cl<sub>2</sub>*, *Physical Review Letters* **93**, 097004 (2004).
- [125] P. Cai, W. Ruan, Y. Peng, C. Ye, X. Li, Z. Hao, X. Zhou, D.-H. Lee, and Y. Wang, *Visualizing the evolution from the Mott insulator to a charge-ordered insulator in lightly doped cuprates*, *Nature Physics* **12**, 1047 (2016).
- [126] I. Battisti, K. M. Bastiaans, V. Fedoseev, A. De La Torre, N. Iliopoulos, A. Tamai, E. C. Hunter, R. S. Perry, J. Zaanen, F. Baumberger, *et al.*, *Universality of pseudogap and emergent order in lightly doped Mott insulators*, *Nature Physics* **13**, 21 (2017).
- [127] H.-S. Kim, Y. Chen, and H.-Y. Kee, *Surface states of perovskite iridates AlRO<sub>3</sub>: Signatures of a topological crystalline metal with nontrivial Z<sub>2</sub> index*, *Physical Review B* **91**, 235103 (2015).
- [128] X. Ming, K. Yamauchi, T. Oguchi, and S. Picozzi, *metal-insulator transition and J<sub>eff</sub> = 1/2 spin-orbit insulating state in rutile-based IrO<sub>2</sub>/TiO<sub>2</sub> superlattices*, *arXiv preprint arXiv:1702.04408* (2017).
- [129] H. Watanabe, T. Shirakawa, and S. Yunoki, *Theoretical study of insulating mechanism in multiorbital Hubbard models with a large spin-orbit coupling: Slater versus Mott scenario in Sr<sub>2</sub>IrO<sub>4</sub>*, *Physical Review B* **89**, 165115 (2014).
- [130] C. Autieri, *Antiferromagnetic and xy ferro-orbital order in insulating SrRuO<sub>3</sub> thin films with SrO termination*, *Journal of Physics: Condensed Matter* **28**, 426004 (2016).
- [131] J. Hwang, J. Son, J. Y. Zhang, A. Janotti, C. G. Van de Walle, and S. Stemmer, *Structural origins of the properties of rare earth nickelate superlattices*, *Physical Review B* **87**, 060101 (2013).
- [132] W. Witczak-Krempa, G. Chen, Y. B. Kim, and L. Balents, *Correlated quantum phenomena in the strong spin-orbit regime*, *Annual Review of Condensed Matter Physics* **5**, 57 (2014).
- [133] J. G. Rau, E. K.-H. Lee, and H.-Y. Kee, *Spin-orbit physics giving rise to novel phases in correlated systems: Iridates and related materials*, *Annual Review of Condensed Matter Physics* **7**, 195 (2016).
- [134] J. Zhao, L. Yang, Y. Yu, F. Li, R. Yu, Z. Fang, L. Chen, and C. Jin, *High-pressure synthesis of orthorhombic SrIrO<sub>3</sub> perovskite and its positive magnetoresistance*, *Journal of Applied Physics* **103**, 103706 (2008).
- [135] E.-X. Wu, J. Zhou, L. Zhang, Y. Chen, S.-T. Zhang, Z.-B. Gu, S.-H. Yao, and Y.-F. Chen, *Metal-insulator transition in SrIrO<sub>3</sub> with strong spin-orbit interaction*, *Journal of Physics: Condensed Matter* **25**, 125604 (2013).
- [136] L. Fruchter, O. Schneegans, and Z. Li, *Anisotropy and interaction effects of strongly strained SrIrO<sub>3</sub> thin films*, *Journal of Applied Physics* **120**, 075307 (2016).
- [137] T. Misawa and M. Imada, *Quantum criticality around metal-insulator transitions of strongly correlated electron systems*, *Physical Review B* **75**, 115121 (2007).
- [138] M. Crawford, M. Subramanian, R. Harlow, J. Fernandez-Baca, Z. Wang, and D. Johnston, *Structural and magnetic studies of Sr<sub>2</sub>IrO<sub>4</sub>*, *Physical Review B* **49**, 9198 (1994).
- [139] C. Wang, H. Seinige, G. Cao, J.-S. Zhou, J. B. Goodenough, and M. Tsoi, *Anisotropic magnetoresistance in antiferromagnetic Sr<sub>2</sub>IrO<sub>4</sub>*, *Physical Review X* **4**, 041034 (2014).
- [140] I. Fina, X. Martí, D. Yi, J. Liu, J.-H. Chu, C. Rayan-Serrao, S. Suresha, A. Shick, J. Železný, T. Jungwirth,

- et al.*, *Anisotropic magnetoresistance in an antiferromagnetic semiconductor*, *Nature Communications* **5**, 4671 (2014).
- [141] C. Lu, B. Gao, H. Wang, W. Wang, S. Yuan, S. Dong, and J.-M. Liu, *Revealing controllable anisotropic magnetoresistance in spin-orbit coupled antiferromagnet  $Sr_2IrO_4$* , *Advanced Functional Materials* **28**, 1706589 (2018).
- [142] J. Nichols, X. Gao, S. Lee, T. L. Meyer, J. W. Freeland, V. Lauter, D. Yi, J. Liu, D. Haskel, J. R. Petrie, *et al.*, *Emerging magnetism and anomalous Hall effect in iridate-manganite heterostructures*, *Nature Communications* **7**, 12721 (2016).
- [143] D. Yi, J. Liu, S.-L. Hsu, L. Zhang, Y. Choi, J.-W. Kim, Z. Chen, J. D. Clarkson, C. R. Serrao, E. Arenholz, *et al.*, *Atomic-scale control of magnetic anisotropy via novel spin-orbit coupling effect in  $La_{2/3}Sr_{1/3}MnO_3/SrIrO_3$  superlattices*, *Proceedings of the National Academy of Sciences* **113**, 6397 (2016).
- [144] D. J. Groenendijk, C. Autieri, T. C. van Thiel, W. Brzezicki, N. Gauquelin, P. Barone, K. H. van den Bos, S. van Aert, J. Verbeeck, A. Filippetti, *et al.*, *Berry phase engineering at oxide interfaces*, *arXiv preprint arXiv:1810.05619* (2018).
- [145] S. Itoh, Y. Endoh, T. Yokoo, S. Ibuka, J.-G. Park, Y. Kaneko, K. S. Takahashi, Y. Tokura, and N. Nagaosa, *Weyl fermions and spin dynamics of metallic ferromagnet  $SrRuO_3$* , *Nature Communications* **7**, 11788 (2016).
- [146] N. Sinitsyn, Q. Niu, J. Sinova, and K. Nomura, *Disorder effects in the anomalous Hall effect induced by Berry curvature*, *Physical Review B* **72**, 045346 (2005).
- [147] S. Onoda, N. Sugimoto, and N. Nagaosa, *Intrinsic versus extrinsic anomalous Hall effect in ferromagnets*, *Physical Review Letters* **97**, 126602 (2006).
- [148] A. De Backer, K. Van den Bos, W. Van den Broek, J. Sijbers, and S. Van Aert, *StatSTEM: an efficient approach for accurate and precise model-based quantification of atomic resolution electron microscopy images*, *Ultramicroscopy* **171**, 104 (2016).
- [149] Q. Gan, R. Rao, C. Eom, J. Garrett, and M. Lee, *Direct measurement of strain effects on magnetic and electrical properties of epitaxial  $SrRuO_3$  thin films*, *Applied Physics Letters* **72**, 978 (1998).
- [150] C. Jung, H. Yamada, M. Kawasaki, and Y. Tokura, *Magnetic anisotropy control of  $SrRuO_3$  films by tunable epitaxial strain*, *Applied Physics Letters* **84**, 2590 (2004).
- [151] D. Kan, R. Aso, H. Kurata, and Y. Shimakawa, *Epitaxial strain effect in tetragonal  $SrRuO_3$  thin films*, *Journal of Applied Physics* **113**, 173912 (2013).
- [152] T. Kobayashi, H. Tsuji, S. Tsunashima, and S. Uchiyama, *Magnetization process of exchange-coupled ferrimagnetic double-layered films*, *Japanese Journal of Applied Physics* **20**, 2089 (1981).
- [153] S. Zhang, Y. Liu, L. Collins-McIntyre, T. Hesjedal, J. Zhang, S. Wang, and G. Yu, *Extraordinary Hall balance*, *Scientific Reports* **3**, 2087 (2013).
- [154] S. Zhang and T. Hesjedal, *The magneto-Hall difference and the planar extraordinary Hall balance*, *AIP Advances* **6**, 045019 (2016).
- [155] D. Kan and Y. Shimakawa, *Defect-induced anomalous transverse resistivity in an itinerant ferromagnetic oxide*, *Physica Status Solidi (b)* (2018).
- [156] E. Grieten, O. Schalm, P. Tack, S. Bauters, P. Storme, N. Gauquelin, J. Caen, A. Patelli, L. Vincze, and D. Schryvers, *Reclaiming the image of daguerreotypes: Characterization of the corroded surface before and after atmospheric plasma treatment*, *Journal of Cultural Heritage* **28**, 56 (2017).
- [157] B. Conings, S. A. Bretschneider, A. Babayigit, N. Gauquelin, I. Cardinaletti, J. Manca, J. Verbeeck, H. J. Snaith, and H.-G. Boyen, *Structure-Property Relations of Methylamine Vapor Treated Hybrid Perovskite  $CH_3NH_3PbI_3$  Films and Solar Cells*, *ACS Applied Materials & Interfaces* **9**, 8092 (2017).
- [158] G. Kresse and J. Furthmüller, *Efficiency of *ab-initio* total energy calculations for metals and semiconductors using a plane-wave basis set*, *Computational Materials Science* **6**, 15 (1996).
- [159] J. P. Perdew and A. Zunger, *Self-interaction correction to density-functional approximations for many-*

- electron systems*, *Physical Review B* **23**, 5048 (1981).
- [160] D. M. Ceperley and B. Alder, *Ground state of the electron gas by a stochastic method*, *Physical Review Letters* **45**, 566 (1980).
- [161] C. Etz, I. Maznichenko, D. Böttcher, J. Henk, A. Yaresko, W. Hergert, I. Mazin, I. Mertig, and A. Ernst, *Indications of weak electronic correlations in SrRuO<sub>3</sub> from first-principles calculations*, *Physical Review B* **86**, 064441 (2012).
- [162] S. Roy, C. Autieri, B. Sanyal, and T. Banerjee, *Interface control of electronic transport across the magnetic phase transition in SrRuO<sub>3</sub>/SrTiO<sub>3</sub> heterointerface*, *Scientific Reports* **5**, 15747 (2015).
- [163] N. Marzari and D. Vanderbilt, *Maximally localized generalized Wannier functions for composite energy bands*, *Physical Review B* **56**, 12847 (1997).
- [164] I. Souza, N. Marzari, and D. Vanderbilt, *Maximally localized Wannier functions for entangled energy bands*, *Physical Review B* **65**, 035109 (2001).
- [165] A. A. Mostofi, J. R. Yates, Y.-S. Lee, I. Souza, D. Vanderbilt, and N. Marzari, *wannier90: A tool for obtaining maximally-localised Wannier functions*, *Computer Physics Communications* **178**, 685 (2008).
- [166] G. Rijnders, D. H. Blank, J. Choi, and C.-B. Eom, *Enhanced surface diffusion through termination conversion during epitaxial SrRuO<sub>3</sub> growth*, *Applied Physics Letters* **84**, 505 (2004).
- [167] E. Dagotto, *Complexity in strongly correlated electronic systems*, *Science* **309**, 257 (2005).
- [168] N. Reyren, S. Thiel, A. Cavaglia, L. F. Kourkoutis, G. Hammerl, C. Richter, C. Schneider, T. Kopp, A.-S. Rüetschi, D. Jaccard, *et al.*, *Superconducting interfaces between insulating oxides*, *Science* **317**, 1196 (2007).
- [169] S. Farokhipoor, C. Magén, S. Venkatesan, J. Íñiguez, C. J. Daumont, D. Rubi, E. Snoeck, M. Mostovoy, C. De Graaf, A. Müller, *et al.*, *Artificial chemical and magnetic structure at the domain walls of an epitaxial oxide*, *Nature* **515**, 379 (2014).
- [170] P. Zubko, J. C. Wojdeł, M. Hadjimichael, S. Fernandez-Pena, A. Sené, I. Luk'yanchuk, J.-M. Triscone, and J. Íñiguez, *Negative capacitance in multidomain ferroelectric superlattices*, *Nature* **534**, 524 (2016).
- [171] J. M. Rondinelli, S. J. May, and J. W. Freeland, *Control of octahedral connectivity in perovskite oxide heterostructures: An emerging route to multifunctional materials discovery*, *MRS Bulletin* **37**, 261 (2012).
- [172] U. K. Bhaskar, N. Banerjee, A. Abdollahi, Z. Wang, D. G. Schlom, G. Rijnders, and G. Catalan, *A flexoelectric microelectromechanical system on silicon*, *Nature Nanotechnology* **11**, 263 (2016).
- [173] D. M. Paskiewicz, R. Sichel-Tissot, E. Karapetrova, L. Stan, and D. D. Fong, *Single-crystalline SrRuO<sub>3</sub> nanomembranes: a platform for flexible oxide electronics*, *Nano Letters* **16**, 534 (2015).
- [174] D. Lu, D. J. Baek, S. S. Hong, L. F. Kourkoutis, Y. Hikita, and H. Y. Hwang, *Synthesis of freestanding single-crystal perovskite films and heterostructures by etching of sacrificial water-soluble layers*, *Nature Materials* **15**, 1255 (2016).
- [175] K. Novoselov, A. Mishchenko, A. Carvalho, and A. C. Neto, *2D materials and van der Waals heterostructures*, *Science* **353** (2016).
- [176] J. Atalaya, J. M. Kinaret, and A. Isacsson, *Nanomechanical mass measurement using nonlinear response of a graphene membrane*, *Europhysics Letters* **91**, 48001 (2010).
- [177] S. P. Koenig, L. Wang, J. Pellegrino, and J. S. Bunch, *Selective molecular sieving through porous graphene*, *Nature Nanotechnology* **7**, 728 (2012).
- [178] A. Smith, F. Niklaus, A. Paussa, S. Vaziri, A. C. Fischer, M. Sterner, F. Forsberg, A. Delin, D. Esseni, P. Palestri, *et al.*, *Electromechanical piezoresistive sensing in suspended graphene membranes*, *Nano Letters* **13**, 3237 (2013).
- [179] R. J. Dolleman, D. Davidovikj, S. J. Cartamil-Bueno, H. S. van der Zant, and P. G. Steeneken, *Graphene squeeze-film pressure sensors*, *Nano Letters* **16**, 568 (2015).
- [180] C. Lee, X. Wei, J. W. Kysar, and J. Hone, *Measurement of the elastic properties and intrinsic strength of*

- monolayer graphene*, *Science* **321**, 385 (2008).
- [181] R. J. Dolleman, S. Hourii, D. Davidovikj, S. J. Cartamil-Bueno, Y. M. Blanter, H. S. van der Zant, and P. G. Steeneken, *Optomechanics for thermal characterization of suspended graphene*, *Physical Review B* **96**, 165421 (2017).
- [182] D. Davidovikj, F. Alijani, S. J. Cartamil-Bueno, H. Zant, M. Amabili, and P. G. Steeneken, *Nonlinear dynamic characterization of two-dimensional materials*, *Nature Communications* **8**, 1253 (2017).
- [183] A. Castellanos-Gomez, M. Buscema, R. Molenaar, V. Singh, L. Janssen, H. S. Van Der Zant, and G. A. Steele, *Deterministic transfer of two-dimensional materials by all-dry viscoelastic stamping*, *2D Materials* **1**, 011002 (2014).
- [184] J. S. Bunch, A. M. Van Der Zande, S. S. Verbridge, I. W. Frank, D. M. Tanenbaum, J. M. Parpia, H. G. Craighead, and P. L. McEuen, *Electromechanical resonators from graphene sheets*, *Science* **315**, 490 (2007).
- [185] A. Castellanos-Gomez, R. van Leeuwen, M. Buscema, H. S. van der Zant, G. A. Steele, and W. J. Venstra, *Single-layer MoS<sub>2</sub> mechanical resonators*, *Advanced Materials* **25**, 6719 (2013).
- [186] M. Cardona, *Optical properties and band structure of SrTiO<sub>3</sub> and BaTiO<sub>3</sub>*, *Physical Review* **140**, A651 (1965).
- [187] S. J. Cartamil-Bueno, P. G. Steeneken, F. D. Tichelaar, E. Navarro-Moratalla, W. J. Venstra, R. van Leeuwen, E. Coronado, H. S. van der Zant, G. A. Steele, and A. Castellanos-Gomez, *High-quality-factor tantalum oxide nanomechanical resonators by laser oxidation of TaSe<sub>2</sub>*, *Nano Research* **8**, 2842 (2015).
- [188] C. Chen, S. Rosenblatt, K. I. Bolotin, W. Kalb, P. Kim, I. Kymissis, H. L. Stormer, T. F. Heinz, and J. Hone, *Performance of monolayer graphene nanomechanical resonators with electrical readout*, *Nature Nanotechnology* **4**, 861 (2009).
- [189] V. Singh, S. Sengupta, H. S. Solanki, R. Dhall, A. Allain, S. Dhara, P. Pant, and M. M. Deshmukh, *Probing thermal expansion of graphene and modal dispersion at low-temperature using graphene nanoelectromechanical systems resonators*, *Nanotechnology* **21**, 165204 (2010).
- [190] N. Morell, A. Reserbat-Plantey, I. Tsioutsios, K. G. Schädler, F. Dubin, F. H. Koppens, and A. Bachtold, *High quality factor mechanical resonators based on WSe<sub>2</sub> monolayers*, *Nano Letters* **16**, 5102 (2016).
- [191] F. W. Lytle, *X-ray diffractometry of low-temperature phase transformations in strontium titanate*, *Journal of Applied Physics* **35**, 2212 (1964).
- [192] H. Unoki and T. Sakudo, *Electron spin resonance of Fe<sup>3+</sup> in SrTiO<sub>3</sub> with special reference to the 110 K phase transition*, *Journal of the Physical Society of Japan* **23**, 546 (1967).
- [193] B. Zalar, A. Lebar, J. Seliger, R. Blinc, V. V. Laguta, and M. Itoh, *NMR study of disorder in BaTiO<sub>3</sub> and SrTiO<sub>3</sub>*, *Physical Review B* **71**, 064107 (2005).
- [194] J. Scott, E. Salje, and M. Carpenter, *Domain wall damping and elastic softening in SrTiO<sub>3</sub>: evidence for polar twin walls*, *Physical Review Letters* **109**, 187601 (2012).
- [195] E. Salje, O. Aktas, M. A. Carpenter, V. Laguta, and J. F. Scott, *Domains within domains and walls within walls: evidence for polar domains in cryogenic SrTiO<sub>3</sub>*, *Physical Review Letters* **111**, 247603 (2013).
- [196] H. Ledbetter, M. Lei, and S. Kim, *Elastic constants, Debye temperatures, and electron-phonon parameters of superconducting cuprates and related oxides*, *Phase Transitions: A Multinational Journal* **23**, 61 (1990).
- [197] J. Scott and H. Ledbetter, *Interpretation of elastic anomalies in SrTiO<sub>3</sub> at 37 K*, *Zeitschrift für Physik B Condensed Matter* **104**, 635 (1997).
- [198] E. Balashova, V. Lemanov, R. Kunze, G. Martin, and M. Weihnacht, *Interdigital transducer application for ultrasonic study of SrTiO<sub>3</sub> in the quantum paraelectric region*, *Solid State Communications* **94**, 17 (1995).
- [199] C. Ang, J. Scott, Z. Yu, H. Ledbetter, and J. Baptista, *Dielectric and ultrasonic anomalies at 16, 37, and 65 K in SrTiO<sub>3</sub>*, *Physical Review B* **59**, 6661 (1999).
- [200] A. Kityk, W. Schranz, P. Sondergeld, D. Havlik, E. Salje, and J. Scott, *Nonlinear elastic behaviour of SrTiO<sub>3</sub>*

- crystals in the quantum paraelectric regime*, *Europhysics Letters* **50**, 41 (2000).
- [201] S. Tsunekawa, H. Watanabe, and H. Takei, *Linear thermal expansion of SrTiO<sub>3</sub>*, *Physica Status Solidi (a)* **83**, 467 (1984).
- [202] E. Mishina, T. Misuryaev, N. Sherstyuk, V. Lemanov, A. Morozov, A. Sigov, and T. Rasing, *Observation of a near-surface structural phase transition in SrTiO<sub>3</sub> by optical second harmonic generation*, *Physical Review Letters* **85**, 3664 (2000).
- [203] J. Haeni, P. Irvin, W. Chang, R. Uecker, P. Reiche, Y. Li, S. Choudhury, W. Tian, M. Hawley, B. Craigo, *et al.*, *Room-temperature ferroelectricity in strained SrTiO<sub>3</sub>*, *Nature* **430**, 758 (2004).
- [204] Q. P. Unterreithmeier, T. Faust, and J. P. Kotthaus, *Damping of nanomechanical resonators*, *Physical Review Letters* **105**, 027205 (2010).
- [205] M. Will, M. Hamer, M. Müller, A. Noury, P. Weber, A. Bachtold, R. V. Gorbachev, C. Stampfer, and J. Güttinger, *High quality factor graphene-based two-dimensional heterostructure mechanical resonator*, *Nano Letters* **17**, 5950 (2017).
- [206] B. Kim, M. A. Hopcroft, R. N. Candler, C. M. Jha, M. Agarwal, R. Melamud, S. A. Chandorkar, G. Yama, and T. W. Kenny, *Temperature dependence of quality factor in MEMS resonators*, *Journal of Microelectromechanical Systems* **17**, 755 (2008).
- [207] S. S. Verbridge, J. M. Parpia, R. B. Reichenbach, L. M. Bellan, and H. Craighead, *High quality factor resonance at room temperature with nanostrings under high tensile stress*, *Journal of Applied Physics* **99**, 124304 (2006).
- [208] R. A. Norte, J. P. Moura, and S. Gröblacher, *Mechanical resonators for quantum optomechanics experiments at room temperature*, *Physical Review Letters* **116**, 147202 (2016).
- [209] M. Honig, J. A. Sulpizio, J. Drori, A. Joshua, E. Zeldov, and S. Ilani, *Local electrostatic imaging of striped domain order in LaAlO<sub>3</sub>/SrTiO<sub>3</sub>*, *Nature Materials* **12**, 1112 (2013).
- [210] E. Salje, X. Ding, Z. Zhao, T. Lookman, and A. Saxena, *Thermally activated avalanches: Jamming and the progression of needle domains*, *Physical Review B* **83**, 104109 (2011).
- [211] D. J. Kok, K. Irmscher, M. Naumann, C. Guguschev, Z. Galazka, and R. Uecker, *Temperature-dependent optical absorption of SrTiO<sub>3</sub>*, *Physica Status Solidi A* **212**, 1880 (2015).
- [212] J. Garai, *Correlation between thermal expansion and heat capacity*, *Calphad* **30**, 354 (2006).
- [213] A. Durán, F. Morales, L. Fuentes, and J. Siqueiros, *Specific heat anomalies at 37, 105 and 455 K in SrTiO<sub>3</sub>:Pr*, *Journal of Physics: Condensed Matter* **20**, 085219 (2008).
- [214] Z. Wang, H. Jia, X. Zheng, R. Yang, Z. Wang, G. Ye, X. Chen, J. Shan, and P. X.-L. Feng, *Black phosphorus nanoelectromechanical resonators vibrating at very high frequencies*, *Nanoscale* **7**, 877 (2015).
- [215] S. J. Cartamil-Bueno, M. Cavaliere, R. Wang, S. Hourri, S. Hofmann, and H. S. van der Zant, *Mechanical characterization and cleaning of CVD single-layer h-BN resonators*, *npj 2D Materials and Applications* **1**, 16 (2017).
- [216] D. Kan, T. Moriyama, K. Kobayashi, and Y. Shimakawa, *Alternative to the topological interpretation of the transverse resistivity anomalies in SrRuO<sub>3</sub>*, *Physical Review B* **98**, 180408 (2018).
- [217] I. Lindfors-Vrejoiu and M. Ziese, *Topological Hall effect in antiferromagnetically coupled SrRuO<sub>3</sub>/La<sub>0.7</sub>Sr<sub>0.3</sub>MnO<sub>3</sub> epitaxial heterostructures*, *Physica Status Solidi (b)* **254**, 1600556 (2017).
- [218] Y. Cao, V. Fatemi, S. Fang, K. Watanabe, T. Taniguchi, E. Kaxiras, and P. Jarillo-Herrero, *Unconventional superconductivity in magic-angle graphene superlattices*, *Nature* **556**, 43 (2018).



# CURRICULUM VITÆ

## Dirk Jan GROENENDIJK

07/02/1991      Born in Nieuwegein, The Netherlands.

### EDUCATION

- 2003–2009      High School  
CS Vincent van Gogh  
Assen, The Netherlands
- 2009–2012      BSc. in Physics & Astronomy  
Utrecht University  
Utrecht, The Netherlands  
*Thesis:*      *Self-assembly of colloids within the spherical confinement of emulsion droplets*  
*Supervisor:*      Dr. A. Imhof
- 2012–2014      MSc. in Applied Physics (*cum laude*)  
Delft University of Technology  
Delft, The Netherlands  
*Thesis:*      *Electrostatically defined PN junctions in ambipolar 2D semiconductors*  
*Supervisor:*      Dr. M. Buscema
- 2014              Internship  
University of Geneva  
Geneva, Switzerland  
*Thesis:*      *Sequential pulsed laser deposition of homoepitaxial SrTiO<sub>3</sub> thin films*  
*Supervisor:*      Dr. S. Gariglio
- 2015–2018      Ph.D. in Applied Physics  
Delft University of Technology  
Delft, The Netherlands  
*Thesis:*      *Spin-orbit coupling and geometric phases at oxide interfaces*  
*Supervisor:*      Dr. A. D. Caviglia



# LIST OF PUBLICATIONS

21. **D. J. Groenendijk**, T. C. van Thiel, and A. D. Caviglia. *Anomalous Hall effect in ultrathin SrRuO<sub>3</sub> bilayers*. (in preparation)
20. A. M. R. V. L. Monteiro, **D. J. Groenendijk**, and A. D. Caviglia. *Anomalous Hall effect in free-standing single-crystal SrRuO<sub>3</sub> films*. (in preparation)
19. T. C. van Thiel, **D. J. Groenendijk**, N. Janssen, W. Brzezicki, C. Autieri, N. Gauquelin, J. Verbeeck, M. Cuoco, and A. D. Caviglia. *Interface-driven anomalous Hall effects in ultrathin LaAlO<sub>3</sub>/SrRuO<sub>3</sub> heterostructures*. (in preparation)
18. **D. J. Groenendijk**, N. Manca, J. de Bruijckere, L. M. K. Tang, A. M. R. V. L. Monteiro, R. Gaudenzi, A. McCollam, H. S. J. van der Zant, and A. D. Caviglia. *Anisotropic magnetoresistance in two-dimensional SrIrO<sub>3</sub>*. (in preparation)
17. **D. J. Groenendijk**, C. Autieri, T. C. van Thiel, W. Brzezicki, P. Barone, N. Gauquelin, J. Verbeeck, A. Filippetti, S. Picozzi, M. Cuoco, and A. D. Caviglia. *Berry phase engineering at oxide interfaces*. [arXiv:1810.05619](https://arxiv.org/abs/1810.05619) (under review)
16. D. Davidovikj\*, **D. J. Groenendijk**\*, A. M. R. V. L. Monteiro, A. Dijkhoff, D. Afanasiev, Y. Huang, E. van Heumen, H. S. J. van der Zant, A. D. Caviglia, and P. G. Steeneken. *Nanomechanics of ultrathin complex oxide membranes*. (under review)
15. D. Afanasiev, A. Gatilova, **D. J. Groenendijk**, B. A. Ivanov, M. Gibert, S. Gariglio, Th. Rasing, A. D. Caviglia, and A. V. Kimel. *Ultrafast spin and charge carrier dynamics in the photo-doped spin-orbit Mott insulator Sr<sub>2</sub>IrO<sub>4</sub>*. (under review)
14. A. M. R. V. L. Monteiro, M. Vivek, **D. J. Groenendijk**, P. Bruneel, I. Leermakers, U. Zeitler, M. Gabay, and A. D. Caviglia. *Band inversion driven by electronic correlations at the (111) LaAlO<sub>3</sub>/SrTiO<sub>3</sub> interface*. [arXiv:1808.03063](https://arxiv.org/abs/1808.03063) (under review)
13. N. Manca, **D. J. Groenendijk**, I. Pallecchi, C. Autieri, L. M. K. Tang, F. Telesio, G. Mattoni, A. McCollam, S. Picozzi, and A. D. Caviglia. *Balanced electron-hole transport in spin-orbit semimetal SrIrO<sub>3</sub> heterostructures*. *Physical Review B* **97**, 081105(R) (2018).
12. **D. J. Groenendijk**, C. Autieri, J. Girovsky, M. Carmen Martinez-Velarte, N. Manca, G. Mattoni, A. M. R. V. L. Monteiro, N. Gauquelin, A. F. Otte, M. Gabay, S. Picozzi, and A. D. Caviglia. *Spin-orbit semimetal SrIrO<sub>3</sub> in the two-dimensional limit*. *Physical Review Letters* **119**, 256403 (2017).
11. G. Mattoni, D. J. Baek, N. Manca, N. Verhagen, **D. J. Groenendijk**, L. F. Kourkoutis, A. Filippetti, and A. D. Caviglia. *Insulator-to-metal transition at oxide interfaces induced by WO<sub>3</sub> overlayers*. *ACS Applied Materials & Interfaces* **9**, 42336–42343 (2017).
10. A. M. R. V. L. Monteiro, **D. J. Groenendijk**, I. Groen, J. de Bruijckere, R. Gaudenzi, H. S. J. van der Zant, and A. D. Caviglia. *Two-dimensional superconductivity at the (111) LaAlO<sub>3</sub>/SrTiO<sub>3</sub> interface*. *Physical Review B* **96**, 020504(R) (2017).

9. A. M. R. V. L. Monteiro, **D. J. Groenendijk**, N. Manca, E. Mulazimoglu, S. Goswami, Ya. Blanter, L. M. K. Vandersypen, and A. D. Caviglia. *Side gate tunable Josephson junctions at the  $\text{LaAlO}_3/\text{SrTiO}_3$  interface*. *Nano Letters* **17**, 715–720 (2017).
8. **D. J. Groenendijk** and S. Gariglio. *Sequential pulsed laser deposition of homoepitaxial  $\text{SrTiO}_3$  thin films*. *Journal of Applied Physics* **120**, 225307 (2016).
7. **D. J. Groenendijk**, N. Manca, G. Mattoni, L. Kootstra, S. Gariglio, Y. Huang, E. van Heumen, and A. D. Caviglia. *Epitaxial growth and thermodynamic stability of  $\text{SrIrO}_3/\text{SrTiO}_3$  heterostructures*. *Applied Physics Letters* **109**, 041906 (2016).
6. M. Buscema, J. O. Island, **D. J. Groenendijk**, S. I. Blanter, G. A. Steele, H. S. J. van der Zant, A. Castellanos-Gomez. *Photocurrent generation with two-dimensional van der Waals semiconductors*. *Chemical Society Reviews* **44**, 3691–3718 (2015).
5. **D. J. Groenendijk**, M. Buscema, G. A. Steele, S. Michaelis de Vasconcellos, R. Bratschitsch, H. S. J. van der Zant, and A. Castellanos-Gomez. *Photovoltaic and photothermoelectric effect in a double-gated  $\text{WSe}_2$  device*. *Nano Letters* **14**, 5846–5852 (2014).
4. B. de Nijs, S. Dussi, F. Smalenburg, J. D. Meeldijk, **D. J. Groenendijk**, L. Fillion, A. Imhof, A. van Blaaderen, M. Dijkstra. *Entropy-driven formation of large icosahedral colloidal clusters by spherical confinement*. *Nature Materials* **14**, 56–60 (2014).
3. M. Buscema\*, **D. J. Groenendijk**\*, G. A. Steele, H. S. J. van der Zant, A. Castellanos-Gomez. *Photovoltaic effect in few-layer black phosphorus PN junctions defined by local electrostatic gating*. *Nature Communications* **5**, 4651 (2014).
2. A. Castellanos-Gomez, L. Vicarelli, E. Prada, J. O. Island, K. L. Narasimha-Acharya, S. I. Blanter, **D. J. Groenendijk**, M. Buscema, G. A. Steele, J. V. Alvarez, H. W. Zandbergen, J. J. Palacios, H. S. J. van der Zant. *Isolation and characterization of few-layer black phosphorus*. *2D Materials* **1**, 025001 (2014).
1. M. Buscema, **D. J. Groenendijk**, S. I. Blanter, G. A. Steele, H. S. J. van der Zant, A. Castellanos-Gomez. *Fast and broadband photoresponse of few-layer black phosphorus field-effect transistors*. *Nano Letters* **14**, 3347–3352 (2014).

# ACKNOWLEDGEMENTS

First and foremost I would like to thank my supervisor and promotor, Andrea Caviglia, for giving me the opportunity to do my PhD research in his group. I am particularly grateful that you entrusted me with the freedom to initiate and pursue my own research directions. I appreciate your creativity, result-oriented approach and ability to distill key information from a large set of data. I expect and look forward to more exciting discoveries from your lab in the coming years. Next I would like to thank my co-promotor, Herre van der Zant. The great time I had during my master's thesis in your lab was one of the reasons I decided to do a PhD. I want to thank you not only for your scientific insights but also for the many wisdoms shared over the years. I would like to extend my gratitude to the members of my committee: Jacobo Santamaria, Tamalika Banerjee, Gertjan Koster, Peter Steeneken, Mario Cuoco, and Yaroslav Blanter. Thank you for reading my thesis, being part of my doctoral committee and a special thanks to those who came from abroad and traveled all the way to Delft.

I gratefully acknowledge everyone who worked with me on a scientific level to obtain the results presented in this thesis. First my collaborators: Yingkai Huang and Erik van Heumen for (re)sintering the strontium iridate and  $\text{Sr}_3\text{Al}_2\text{O}_6$  targets, Nicolas Gauquelin for electron microscopy measurements, Stefano Gariglio for X-ray diffraction measurements, Ilaria Pallecchi and Francesca Telesio for thermoelectric measurements, Lucas Tang and Alix McCollam for high-field magnetotransport measurements, Jan Girovsky, Mari Carmen Martinez-Velarte and Sander Otte for STM measurements, Dejan Davidovikj and Peter Steeneken for mechanical measurements, Joeri de Bruijckere and Rocco Gaudenzi for anisotropic magnetoresistance measurements, Marc Gabay, Carmine Autieri, Wojciech Brzezicki, Silvia Picozzi and Mario Cuoco for theoretical calculations. It was a pleasure working with all of you and I hope we have the opportunity to collaborate in the future.

Next up are the members of the lab. Giordano and Emre, as the first members of the lab you laid the foundations by setting up the measurement systems and optimizing the growth of various material systems. The occasions we had to work together—which often involved detecting vacuum leaks, finding electrical shorts, and soldering wires—were always enjoyable. Besides that, we spent ample time together playing board games, having the occasional drink and enjoying some fine dining. Giordano, we managed to find a good compromise between the Italian grandeur and the Dutch tranquility. After our many discussions about “proper” punctuation and typography, I hope that I didn't mix up any hyphens, en-dashes, and em-dashes. I congratulate you for taking the brave step of moving to Kyoto for a postdoc and am sure an outstanding scientific career will follow. Don't ever stop doing “Friday afternoon” experiments. Emre, besides your impeccable style and ferocious beard I admire your bold move of switching fields to neuroscience and doing a postdoc in Harvard. I am sure you will achieve your goals and have a

bright and eventful future ahead of you. Nicola, you were the first postdoc of the lab and we had the pleasure of working together on various projects, in particular on  $\text{SrIrO}_3$ . You have very clear goals and I appreciate how you manage to find a balance between your personal and professional life. I wish you all the best in your scientific career in Genova.

Andrew and Thierry, I had the pleasure of supervising your master's projects during my third year. I was lucky to supervise two students who were passionate about science and motivated to obtain excellent results. Together we spent (many) evenings at the PLD, the flow cryostat and in the cleanroom, which were always very enjoyable. Andrew, good luck in your future career at ASML. Thierry, I'm glad you joined the group as a PhD student and I am sure you will achieve great results. Keep on looking for that "smoking gun" experiment, and I already look forward to your doctoral defence. Dima and Jorrit—also known as "the optics guys". Dima, when you just arrived as a postdoc I was glad to collaborate with you on the magneto-optical characterization of  $\text{Sr}_2\text{IrO}_4$  films. I admire your work ethic and I am sure it will pay off in the near future. Jorrit, the new genius of the lab. I appreciate your helpfulness and drive for continuous self-improvement. I am sure you have a bright future ahead of you, no matter which direction you choose to pursue. Edouard, although you just joined the lab as a postdoc, I'm sure we would have made a great team and I'm confident that you will make your stay in Delft a great success. Yildiz, you have the tough task of working at the intersection between the difficult fields of complex oxides and microwave resonators. I hope you always remain cheerful and make it a great success. Thanks to all the MSc and BSc students who worked in the lab with us: Niels, Bas, Inge, Nils, Lucinda, Mattias, and H el ene.

Dejan and Davide, my paranymphs. Dejan, in the last few months of our PhD's we finally found a project on which we could work together, studying the properties of complex oxide resonators. It was a great pleasure working with you, and I think that our shared passion for physics made it a success. We spent a lot of time together outside of office hours, in particular at the many dinners, barbecues and game nights that you organised. You are kind, generous, and passionate about many different things. You became familiar with the Dutch language (and culture!) in the blink of an eye. It comes as no surprise to me that, only a few months in, you are already excelling in your new career. I am confident that you and your witty jokes will achieve all your goals. Davide, in many ways (except for food) you are the opposite of the Italian stereotype: patient, quiet and modest. I am grateful to have enjoyed your kindness and support over the years. If you would have not motivated me to do sports together I would certainly need a suit a few sizes larger—though your passion for making cakes (and having us tasting them) almost compensated for that. Thank you for all the nice chats, playing games and watching the GP together. Believe in yourself and I am sure that you will be very successful no matter what you choose to do after your PhD.

Nikos, the master of the barbecue and the DJ set. Besides your amazing cooking skills, you have an incredible work ethic. I hope you make up your mind on what you want to do next and I am sure you will be successful and happy with whatever decision you make. Thank you and Andrea for taking such good care of Maxwell. Thanks to those who met on Tuesday evenings for drinks and (philosophical) discussions—Holger, Marc, Pascal, Joeri, Nikos, Iacopo and Andreas. Holger, with your work ethic and attention to

detail I am sure you will have an exceptional scientific career full of discoveries. Marc, thank you for the interesting discussions about business and politics and for always being in good spirits. Pascal, I look forward to tasting more of your homebrew beers. Joeri, I hope we can visit a concert together some time. Thanks to everyone else who made my stay at QN a pleasure: Gary, Sander, Simon, Peter, João, Rocco, Santiago, Max, Mickael, Riccardo, Ignacio, Shun, Matvey, Felix, Lorenzo, Ranko, Floris, Robin, Makars, Martin, Sarwan, Vera, Sofya, Michele, Andres, Joshua, and Srijit. Marijke, Etty and Maria, thank you for making QN such a nice place to work. Tino, Ronald, Mascha and Ron, thank you for keeping all our systems running over the years.

Mafalda, I reserved a special place for you at the end. We embarked on this four-year adventure together, starting on the same day in the same lab. Being a great team, we worked on many projects together and were always there to lift each other up when things seemed down. Thank you for all your kindness and support, and I can't wait to start our next chapter together! Sander, thank you for your friendship and all the time we spent together during the last four years. Let's see where our next hiking trip will take us. Finally, my deep gratitude to my family for their continuous help and support. I am indebted to my parents for giving me the opportunities and experiences that brought me this far. Thank you for encouraging me to do my best and follow my passion. I am grateful to my sisters for always supporting me and for setting an example for many things in life. I am happy that we managed to stay so close even though we followed very different paths and hope we can continue to see each other so often!